

---

# Theoretical Interpretation of Scanning Probe Images of Molecules on Surfaces

Mohammad Abdur Rashid

Thesis submitted to the University of Nottingham  
for the degree of Doctor of Philosophy

April 2017

---

---

# Abstract

---

Scanning tunnelling microscopy (STM) and atomic force microscopy (AFM) can produce images of molecules with extremely high resolution. However, Claims that dynamic force microscopy has the capability to resolve intermolecular bonds in real space continue to be vigorously debated. Several studies have now shown that tip flexibility, especially at very close tip-sample separations, is responsible for the striking intra- and intermolecular resolution observed with various scanning probe microscopy techniques. The apparent intermolecular features can be observed with dynamic force microscopy even when no bonding interaction is present, suggesting that such features are in fact an artefact and cannot be interpreted as a real-space image of an intermolecular bond.

We have studied the interaction between fullerene ( $C_{60}$ ) molecules using a sum of pairwise Lennard-Jones (12-6) potentials, and investigated how flexibility in the tip can produce a bond like feature between the molecules in a  $C_{60}$  island where there is no chemical bond present except the weak van der Waals force. We also investigate how the potential between the molecules is dependent on their relative orientations. For a given configuration of the tip and the sample molecules, our results allow us to predict the form of the intermolecular potential that would be observed using non contact atomic force microscopy (NC-AFM).

Our study on the Si(111)-(7×7) reconstructed surface using the same model provides a better understating on the origin of sub-atomic contrast observed

## **Abstract**

---

in experiment suggesting that the contrast can arise from a flexible tip exploring an asymmetric potential created due to the positioning of the surrounding surface atoms. We have also simulated NC-AFM images of 2D bi-isonicotinic acid lattice using the same model. The geometry of the lattice have been optimized using DFT before simulating AFM images. Simulation results are in a good agreement with the experiment.

The theoretical work is accompanied by a variety of experimental results obtained by the group of Prof Philip Moriarty at the University of Nottingham.

---

# Acknowledgements

---

Firstly, I praise and thank almighty Allah, the Lord of the worlds, the Most Merciful, the Guider of hearts, the Provider of sustenance, the Owner of life and death. This thesis will not be done without His will.

I would like to express my special appreciation and thanks to my supervisor Dr Janette Dunn, whose selfless time and care were sometimes all that kept me going. I could not have imagined having a better supervisor for my PhD study. I am deeply indebted to my second supervisor Prof Philip Moriarty, for his continuous support, and personal involvement in all phases of this research. It has been a pleasure to work alongside them.

Special mention goes to Samuel Jarvis and Adam Sweetman for their insightful conversations and sharing their experimental results. I would like to extend my gratitude to Andrew Lakin, Jeremy Leaf, and Effat Rashed for their help and suggestions. I am also grateful to Zaid, Enamul, Zaidi, Belal, Ferdous, Ullash, Amin, Iqbal, Ali, Enam and all those who helped me during the last few years and made the life enjoyable in the UK. I would also like to take this opportunity to thank Hamidur Rahman, Ziauddin Ahmed, Iftekhar Arafath, Salekin, and Sayem for their encouragement.

Finally, but by no means least, thanks go to my parents and sisters, for their love and sacrifice. I am also especially grateful to my wife, for her care and moral support during the most difficult times. May Allah grant them goodly lives. May peace and praise be upon the Prophet Muhammad, his family members, and his companions.

---

# List of Publications

---

Jarvis, S. P., **Rashid, M. A.**, Sweetman, A., Leaf, J., Taylor, S., Moriarty, P., and Dunn, J., Intermolecular artifacts in probe microscope images of  $C_{60}$  assemblies, *Phys. Rev. B* **92**, 241405(R) (2015).

Sweetman, A., **Rashid, M. A.**, Jarvis, S. P., Dunn, J. L., Rahe, P., and Moriarty, P., Visualizing the orientational dependence of an intermolecular potential, *Nat. Commun.* **7**, 10621 (2016).

Sweetman, A., Jarvis, S. P., and **Rashid, M. A.** Modelling of sub-atomic contrast resulting from back-bonding on Si(111)- $7\times 7$ , *Beilstein J. Nanotechnol.* **7**, 937–945 (2016).

---

# Contents

---

## Theoretical Interpretation of Scanning Probe Images of Molecules on Surfaces

<b>1</b>	<b>Introduction</b>	<b>1</b>
1.1	Motivation . . . . .	1
1.2	Structure of the thesis . . . . .	3
<b>2</b>	<b>Scanning probe microscopy</b>	<b>5</b>
2.1	Scanning tunnelling microscopy . . . . .	6
2.1.1	The physics of STM . . . . .	6
2.1.2	Modes of STM operation . . . . .	9
2.2	Atomic force microscopy . . . . .	11
2.2.1	The physics of AFM . . . . .	11
2.2.2	Modes of AFM operation . . . . .	14
2.2.3	AM and FM operation of NC-AFM . . . . .	15
2.3	Frequency shifts and tip-sample forces in frequency-modulation AFM . . . . .	17
2.4	Functionalized tip . . . . .	19
2.5	Modeling SPM . . . . .	20
2.5.1	Density functional theory . . . . .	20
2.5.2	Hückel molecular orbital theory . . . . .	21
2.5.3	Mechanical AFM model . . . . .	22

## Contents

---

<b>3</b>	<b>Recent advances in submolecular resolution with NC-AFM</b>	<b>23</b>
3.1	Modification of the scanning probe . . . . .	24
3.2	Flexibility of the CO-terminated tip . . . . .	28
3.3	Conclusions . . . . .	32
<b>4</b>	<b>Theoretical basis</b>	<b>34</b>
4.1	Hückel theory for molecular orbitals . . . . .	34
4.1.1	Simple HMO theory . . . . .	35
4.1.2	Modified HMO theory for heteroatom System . . . . .	37
4.1.3	Extended HMO theory . . . . .	39
4.1.4	Gaussian type orbital . . . . .	40
4.2	Simulating STM images using Hückel MO theory . . . . .	42
4.2.1	Derivative rule for tip state . . . . .	44
4.3	Modelling the surface interaction . . . . .	45
4.4	Simulating AFM images using Hückel MO theory . . . . .	46
4.5	Mechanical AFM model with a flexible tip . . . . .	50
4.5.1	Simulating AFM images . . . . .	51
4.6	Kohn-Sham DFT . . . . .	52
<b>5</b>	<b>Intermolecular artifacts in AFM images of C<sub>60</sub> lattices</b>	<b>56</b>
5.1	Buckminsterfullerene, C <sub>60</sub> . . . . .	57
5.2	Why C <sub>60</sub> . . . . .	57
5.3	NC-AFM study of C <sub>60</sub> monolayer . . . . .	59
5.4	Modelling NC-AFM images of C <sub>60</sub> assembly . . . . .	59
5.4.1	Variation in force experienced by the probe particle . . . . .	65
5.4.2	Effect of stiffness parameter in the contrast of the simulated AFM images . . . . .	69
5.4.3	The role of molecular orientation and symmetry . . . . .	73
5.5	Simulating AFM images using EHMO theory . . . . .	75

## Contents

---

5.6	Orientation-dependent simulation of AFM images . . . . .	78
5.7	Conclusions . . . . .	85
<b>6</b>	<b>Modeling STM images of <math>C_{60}F_{48}</math> using Hückel theory</b>	<b>89</b>
6.1	Constructing molecular orbitals of $C_{60}F_{48}$ using modified HMO theory . . . . .	90
6.2	Constructing molecular orbitals of $C_{60}F_{48}$ using EHMO theory	91
6.3	Incorporating the surface interaction . . . . .	93
6.4	Simulating a constant current STM image . . . . .	95
<b>7</b>	<b>Interpreting NC-AFM images of Si(111)-(7×7) surface</b>	<b>100</b>
7.1	The Si(111)-(7×7) reconstructed surface . . . . .	100
7.2	L-J parameters . . . . .	102
7.3	Origin of triangular contrast . . . . .	103
7.4	Conclusions . . . . .	108
<b>8</b>	<b>Interpreting ultrahigh resolution images of 2D bi-isonicotinic acid islands</b>	<b>111</b>
8.1	Structure of bi-isonicotinic acid molecule . . . . .	112
8.2	Geometry optimization using Kohn-Sham DFT . . . . .	113
8.3	Generating simulated AFM images of bi-isonicotinic acid molecules	117
8.4	Simulating AFM images of 2D bi-isonicotinic acid lattices . .	118
8.4.1	Effect of stiffness parameter in simulated AFM images	123
8.5	Conclusion . . . . .	129
<b>9</b>	<b>Summary</b>	<b>130</b>
<b>A</b>	<b>Metal phthalocyanine (MPcs)</b>	<b>134</b>
	<b>Bibliography</b>	<b>138</b>

**Theoretical Interpretation of  
Scanning Probe Images of  
Molecules on Surfaces**

# Chapter 1

---

## Introduction

---

The advancement of scanning probe microscopy (SPM) not only allows us to investigate the fundamental electronic, magnetic and mechanical properties of individual molecules [1–3] but also enables us to image, measure and manipulate matter at surfaces with atomic resolution [4–6]. Scanning tunnelling microscopy (STM) [7] and atomic force microscopy (AFM) [8] can probe both the atomic and electronic structure of single molecules and self assembled aggregates of molecules on surfaces. STM, the ancestor of all scanning probe microscopies, uses the concept of quantum tunnelling of electrons to provide information on the electronic structure of the system arising from its frontier orbitals. On the other hand, AFM is based on arguably the “most intuitive” interaction at the atomic level, the force, giving us the ability to feel materials in a way which is closer to daily life interaction, but at the atomic or molecular level.

### 1.1 Motivation

Intermolecular interactions which govern the chemistry “beyond the molecule” [9, 10] are responsible for stabilising self-assembled arrays of molecules and

## Introduction

---

supramolecular systems. The potential to investigate intermolecular interactions at the single bond limit is therefore particularly attractive especially for molecular and supramolecular self-assembly on surfaces [11–13]. In recent years dynamic force microscopy (also called non-contact atomic force microscopy (NC-AFM)) has provided unprecedented submolecular detail for a variety of systems [14–19]. This has been achieved by terminating the scanning probe with a single molecule which is subsequently moved so close to the underlying molecule that repulsive tip-sample interactions from the molecular skeleton yield exceptionally high resolution.

To understand the origin of such intra- and intermolecular contrast and the exact nature of the interactions of the atoms and molecules with each other, however it is of utmost important to have a thorough theoretical understanding of the physics and the physical chemistry that underlies them. In studying the majority of systems that are of interest using the available methods, such as density functional theory (DFT), it is required to undertake computationally expensive calculation. Thus, alternative methods which would allow a much easier and faster analysis of systems are always of interest.

The aim of this work is to contribute in developing a simple, less expensive theoretical technique to model the outcome of SPM experiments for a variety of systems. In particular, we focus on modelling high-resolution NC-AFM images that are obtained using a functionalized tip and have revealed “bond like” features between the molecules. Using a mechanical model based on the Lennard-Jones potential we are able to explain the possible origin of such striking intermolecular contrast. We study assemblies of  $C_{60}$ , of bi-isonicotinic acid, and Si(111)- $7\times 7$  reconstructed surface using the model. We optimized the geometry of the island of bi-isonicotinic acid molecules using DFT while for Si(111)- $7\times 7$  surface a previous DFT-optimized geometry was used. In addition, we simulated STM images of  $C_{60}F_{48}$  which show band-like features for the molecular orbitals.

### 1.2 Structure of the thesis

In Chapter 2 we discuss the basics of scanning probe microscopy, more specifically the basic principles on which STM and AFM are based. We also discuss their different operational modes and their working procedures in brief. Following that, the idea of tip functionalization will be introduced. Finally, several theoretical techniques that may be used when modelling STM and AFM images will be discussed in brief along with their advantages and shortcomings. A short review on recent achievements on producing high resolution images of molecules with NC-AFM is presented in Chapter 3. In the review we mainly focused on the effect of tip functionalization and its flexibility, which is eventually responsible for producing extremely high resolution of molecules in NC-AFM.

Chapter 4 describes the theoretical models that we have used to simulate AFM and STM images. First, we discuss Hückel molecular orbital (HMO) theory with an example. The modified and extended versions of the HMO have been covered in detail. The application of these theories to modeling STM and AFM images is then presented. This is followed by a description of a mechanical AFM model which is based on the Lennard-Jones empirical potential, coupled with a flexible tip which is free to move at the end of the force microscope probe. We finish Chapter 4 with a description of density functional theory (DFT), which was used to find the optimized geometry of the assembly of bi-isonicotinic acid molecules.

In Chapter 5 we present the simulation results for AFM images for assemblies of  $C_{60}$  molecules and individual  $C_{60}$  molecules. We start with a study of the assembly of  $C_{60}$  using a functionalized tip and show how a  $C_{60}$ -terminated flexible tip can reproduce the intermolecular contrast that is observed experimentally. In this study the tip is approximated as a single sphere to represent the functionalized tip. This is followed by the result from the study of isolated  $C_{60}$  molecules, in which case a detailed functionalized tip

## Introduction

---

with atomic description of the  $C_{60}$  molecule is used. Since both probe and sample are described with atomic details, depending on the orientation of the probe and the sample, a large number of configurations of the probe-sample system is possible. We have generated theoretical AFM images for a number of configurations and found a good match to the experimental results. We continue by studying the fullerene based molecule  $C_{60}F_{48}$  in Chapter 6. We show how Hückel molecular orbital theory can be used to simulate STM images using different tip states. In our study we find similar feature in the simulated images as found in experiment.

We also study the Si(111)-(7×7) reconstructed surface theoretically and demonstrate how *sub-atomic* contrast can arise from a flexible tip exploring an asymmetric potential created due to the positioning of the surrounding surface atoms, which are presented in Chapter 7. Chapter 8 includes the results on the study of assembly of bi-isonicotinic acid using the mechanical AFM model. The geometry of the assembly is optimized using DFT.

Finally, Chapter 9 contains the summary of this work.

## Chapter 2

---

# Scanning probe microscopy

---

The scanning probe microscope (SPM) is an imaging tool which produces topographical maps of a sample at the atomic level allowing unprecedented views of surfaces and providing local spectroscopy. It is one of the powerful modern research techniques that is used in a wide variety of disciplines, from fundamental surface science research to food and agriculture industry. Unlike electron and optical microscopes SPM uses a sharp tip, which acts as the probe to sense the strength of a particular interaction between the tip and the sample. During the measurements the tip scans the sample maintaining a very close spacing to the sample and the tip-sample interaction is recorded as a function of tip position. A computer is used to accrue the data and to generate the images of the surface.

SPM has formed a basis for development of new methods in nanotechnology, which aims to investigate and manipulate single atoms and molecules. The first instrument that was used to generate real-space images of surfaces with atomic resolution is the scanning tunnelling microscope (STM) [20], the ancestor of all scanning probe microscopes. STM produces topological image of the surface by measuring the tunnelling current between the probe and the sample. Atomic force microscopy (AFM) is the other most com-

monly utilized tool for probing systems at an atomistic level. AFM uses the force between the sample and the probe to construct the image of the system. In this chapter, the physics that forms the basis of STM and AFM will be discussed, alongside with their operational modes. The idea of tip functionalisation in SPM and the various theoretical techniques that may be used when simulating SPM images will also be described.

## 2.1 Scanning tunnelling microscopy

STM, developed by Binnig and Rohrer [21] at IBM, is a microscope of atomic level resolution. The invention of STM not only brought a revolutionary change in probing and imaging materials in atomic level but also won the 1986 Nobel Prize in Physics for its inventors. The concept of quantum tunnelling of electrons between the tip and the substrate is used in STM and it can be operated in air, in inert gas, in ultrahigh vacuum and even in liquids within a temperature ranging from absolute zero to hundreds of degree centigrade [22]. The tunnelling current, which depends on the tip-sample separation, together with the applied voltage and the vertical position of the tip, is used to create a topographical map of the local density of states of the material under study. The resolution that is considered to be good for STM is about 1.0 Å laterally and 0.1 Å in depth [23]. This means that materials can be imaged in atomic resolution and individual atoms within materials can be manipulated [4]. STM is widely used both in research institution and in industry.

### 2.1.1 The physics of STM

STM is a non-optical electron-based microscope which operates on the basis of quantum mechanical tunnelling of electrons between the STM tip and the sample under investigation. In classical physics an electron can-

## Scanning probe microscopy

---

not penetrate into or across a potential barrier if its energy is smaller than the potential within the barrier while quantum mechanical treatment predicts an exponentially decaying solution for the electron wave function in the barrier giving a non-zero probability of finding the electron beyond the barrier. Figure 2.1 shows the schematic of quantum mechanical tunnelling through a 1D rectangular potential barrier. The region inside the barrier is classically forbidden, a particle with energy  $E < U_0$  could not penetrate according to classical physics. However, according to quantum mechanics, there is a finite probability that the particle will tunnel through the barrier.

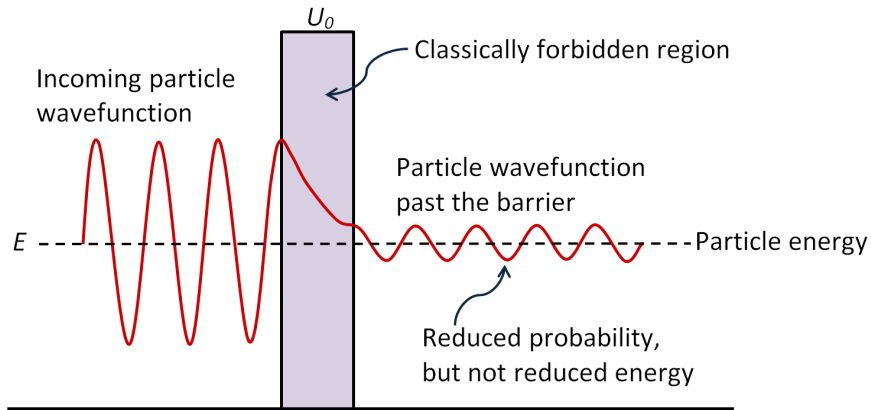


**Figure 2.1:** Schematic of wavefunction tunnelling through one dimensional rectangular potential barrier.

In STM when the tip is brought very close to the sample and a small bias voltage is applied between the tip and the sample, a tunnelling current flows through the vacuum gap between the tip and the sample. The decay of current is determined by the vacuum gap, the applied bias and the conducting properties of the tip and the sample and can be expressed as

$$I(z) = I_0 e^{-2\kappa z}, \quad (2.1)$$

where  $I_0$  is a function of the applied voltage and density of states in both tip and the sample,  $\kappa$  is the decay constant and  $z$  is the separation between

## Scanning probe microscopy

---

the tip and the sample.

With an applied bias voltage, tunnelling only occurs if the tip is brought sufficiently close to the sample so that the wavefunction has not decayed such that the flow would be too weak to detect. An image of the sample can only be constructed if a current is detected by the tip i.e. if a net flow of electrons is maintained between the tip and the sample. However with zero bias if the tip and sample are close enough for sufficient tunnelling to occur, the electrons would tunnel equally in both directions considering them at the same energy state. In that case no net current will be observed at the tip. Hence, in order to favour the flow of electrons in one direction or the other a bias is applied to the sample. If a positive sample bias is applied, the Fermi level of the sample electrons will be decreased, favouring a flow from the tip to the sample while the opposite will happen for a negative sample bias, resulting in an increase of the Fermi level of the sample electrons. Since electrons can flow from the metal tip to the sample surface or vice versa, depending on the polarity of the bias, it is possible to gain more information about the electronic structure of the surface by studying the variation of the STM signal on the sign and magnitude of the tip-sample voltage. STM can not be used to image a non-conducting surface as the tunnelling of current through the tip is essential to image the sample.

The basic components of an STM are shown in Figure 2.2. The probe of an STM is usually made of tungsten or a platinum-iridium alloy and is attached to a piezo tube. The position of the tip in three dimensions is accurately controlled by the piezoelectric tube scanner. There are five electrodes (labelled as  $x^-$ ,  $x^+$ ,  $y^-$ ,  $y^+$  and  $z$ ) attached to the piezo tube, which selects the directions and elongations of scan according to the potential applied to corresponding electrodes. The separation between the tip and the sample is controlled by using the coarse positioner and the  $z$  piezo. To induce a tunnelling current a bias voltage is applied between the tip and the sample. During normal operation, the tunnelling current is held constant by con-

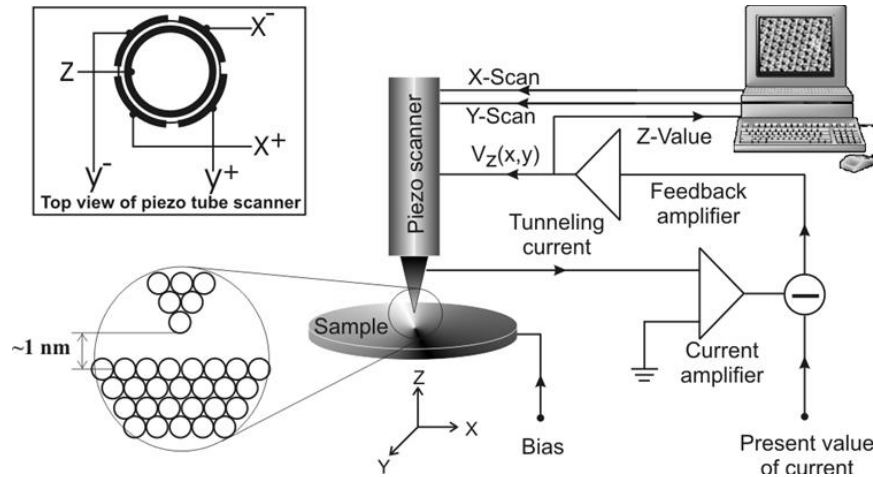


**Figure 2.2:** Schematic diagram showing the working principle of STM, microscopic view of tip-sample interface is shown in the circle. Inset is the top view of the piezo tube scanner,  $x^-$ ,  $x^+$ ,  $y^-$ ,  $y^+$  and  $z$  represent the electrodes on and inside the piezo tube. Image taken from [24].

trolling the  $z$  piezo through the use of a feedback circuit. The tunnelling current is converted to a voltage by the current amplifier and is used to obtain an equilibrium  $z$  position. As the tip scans over the  $xy$  plane, a two-dimensional array of equilibrium  $z$  positions, representing a contour plot of the equal tunnelling-current surface, is obtained, displayed, and stored in the computer memory. To ensure stable operation, vibration isolation is essential. This is achieved by making the STM unit as rigid as possible, and by reducing the influence of environmental vibration to the STM unit.

### 2.1.2 Modes of STM operation

STM can be operated both in constant current and constant height modes. The latter is simpler and quicker but the former usually provides more information. A bias voltage between the tip and the conducting sample is applied in both cases. When the tip-sample distance is small enough, say a few angstroms, a tunnelling current occurs, as a result of the tunnelling electrons flow either from tip to sample or vice versa depending on the bias.

In constant height mode the tip is kept at a fixed vertical height and the variation of tunnelling current due to the topography and local electronic

## Scanning probe microscopy

---

properties of the surface coupled to the lateral tip position is used in imaging the sample. It is the simplest mode of STM operation and can only be used for very smooth surfaces. For a rough surface there is an increased chance of the tip crashing into the surface because of fixed height. Hence flat samples with very low roughness are commonly used to image in constant height mode.

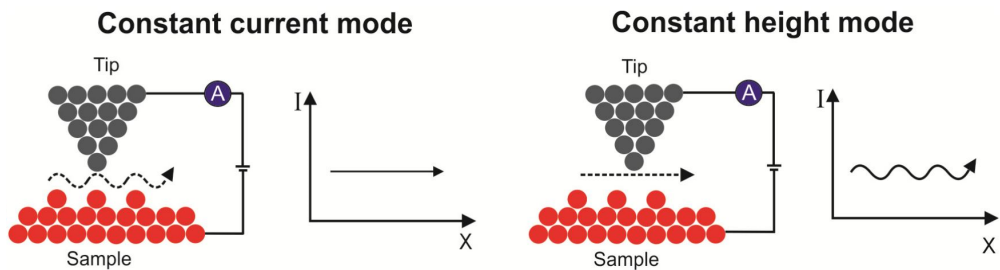


**Figure 2.3:** Schematic illustration of the two different operation modes of STM: the constant current mode (left) and the constant height mode (right). Image adapted from reference [25].

A more detailed image of the sample can be constructed when the STM is operated in constant current mode compared to constant height mode. In constant current mode, the tunnelling current is kept constant by a feedback circuit during the scan while the vertical distance between the tip and the sample is allowed to change. The vertical position of the tip is used to image the sample surface. As the tip height is actively varied to maintain a constant current this mode of operation is slower than the previous one. Related to this mode is dynamic STM, where a constant average current is maintained while the tip is oscillated at a set frequency. Since the tip is allowed to penetrate further into the sample than the constant current mode, an even more detailed image of the sample can be constructed during dynamic STM operation.

## 2.2 Atomic force microscopy

Atomic force microscopy, developed by Binnig, Quate and Gerber in 1985 [8], is a powerful microscopy for studying samples at atomic resolution irrespective of the surface topology or conductivity of the sample. The tip of the AFM scans across the surface of a sample to measure the surface morphology and constructs a 3D image of the surface. AFM can be operated both in air and in liquid and it allows study of the local resistivity, elasticity, tribology, microstructure of a surface.

### 2.2.1 The physics of AFM

AFM uses the force interactions between the sample and the tip to construct an image of the sample, unlike STM which uses the quantum mechanical effect of electron tunnelling between the tip and the sample. Depending on the separation between the tip and the sample, the forces can be roughly divided into two groups: i) long-range forces which are attractive and mostly van der Waals (vdW) in nature but also include magnetic and electrostatic forces as well; ii) short-range repulsive force which correspond to the interaction of the tip apex with the atomic scale feature of the surface and arises from the Pauli exclusion principle. Both the vdW attraction and Pauli repulsion forces can be modeled using the Lennard-Jones (L-J) potential which is written as

$$U(r) = \epsilon \left[ \left( \frac{r_0}{r} \right)^{12} - 2 \left( \frac{r_0}{r} \right)^6 \right], \quad (2.2)$$

where  $\epsilon$  is the depth of the potential well and  $r_0$  is the distance at which the potential reaches its minimum i.e.  $U(r_0) = -\epsilon$ . The L-J potential is an empirically derived function to model the energy of two interacting atoms. The  $r^{-12}$  term in Eq. (2.2) models the Pauli repulsion force and becomes extremely dominant with a steep increase in the function when inter atomic

## Scanning probe microscopy

---

separation is less than  $r_0$  i.e. when electron orbitals overlap. The  $r^{-6}$  models the van der Waals attraction force and is dominant at long range. The force is related to the potential by its negative gradient,

$$\begin{aligned} F(r) &= -\frac{dU}{dr} \\ &= 12\epsilon \left[ \left( \frac{r_0^{12}}{r^{13}} \right) - \left( \frac{r_0^6}{r^7} \right) \right]. \end{aligned} \quad (2.3)$$

Figure 2.4 shows an illustration of a L-J type potential where the interaction between two arbitrary atoms is plotted as a function of the interatomic distance. It can be seen from the plot that the energy decreases within the attractive regime as the two atoms approach, indicating an attractive force. At  $r = r_0$  the vdW force cancels out the Pauli repulsion and there is no net force acting between the atoms. When the atoms are pushed closer i.e. at  $r < r_0$ , the energy increases at a rapid rate, hence the repulsive forces become dominant.

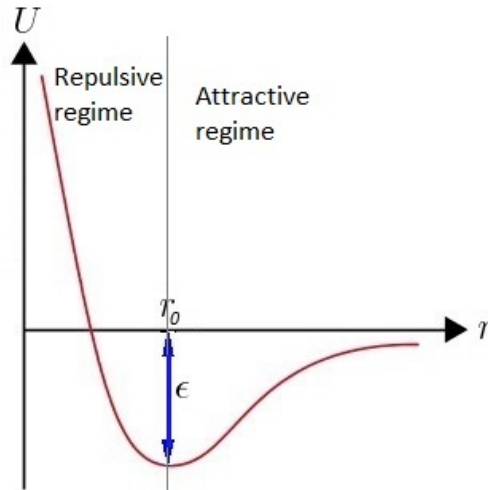


**Figure 2.4:** A graph showing the typical shape of the Lennard-Jones potential.

Since the first invention of AFM [8], like any other devices, it has undergone many developments. In early AFM, a cantilever with a very sharp tip was used to scan over a sample surface. When the tip approaches the surface, the

## Scanning probe microscopy

---

attractive vdW force between the surface and the tip causes the cantilever to deflect towards the surface. As the tip comes closer to the sample, such that it makes contact with the surface, Pauli repulsion becomes more and more significant and causes the cantilever to deflect away from the surface. Four photodiodes in a cross configuration are used to detect the change in the direction of the reflecting laser caused by the cantilever. The tip-sample interaction is kept constant by a feedback circuit during the scan of a sample. The working principle of an AFM which uses a cantilever is shown schematically in Figure 2.5 using a schematic diagram.

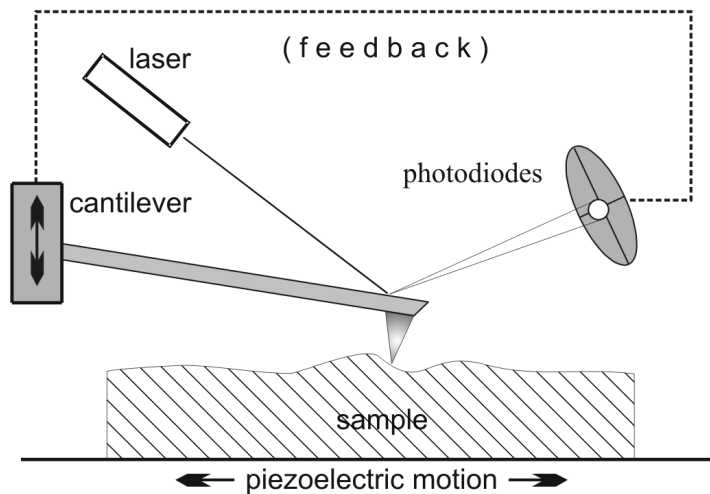


**Figure 2.5:** Schematic description of the operation principle of the AFM. The feedback loop monitors the cantilever deflection and keeps it constant by adjusting the vertical position of the cantilever. Figure adapted from reference [26].

Nowadays, in AFM, instead of using a silicon cantilever, a qPlus sensor [27] is often used. The qPlus sensor is originally made from a quartz tuning fork which has many technological and operational advantages over the traditional cantilever. Quartz tuning forks are not only produced in large quantity with an incredible level of consistency but also has large stiffness ( $\sim 1800 \text{ Nm}^{-1}$ ) compare to silicon cantilever ( $\sim 10 \text{ Nm}^{-1}$ ), which facilitates smaller amplitude (below  $1 \text{ \AA}$ ) oscillation compared to conventional cantilevers. The tip is glued to one prong of the tuning fork and the other

prong is bonded to a mount (Figure 2.6). As a result, only one prong (at which the tip is attached) of the quartz tuning fork oscillates keeping the other prong fixed, just like a cantilever driven by an oscillator. The quality of the bond between the fixed prong and the mount is crucial for obtaining high  $Q$  factor. Since quartz is piezoelectric, the AFM deflection can be directly measured using the electric signal originating from the sensor rather than relying on an external technique (such as laser deflection). This not only reduces the complexity of the instrument but also simplifies its operation.

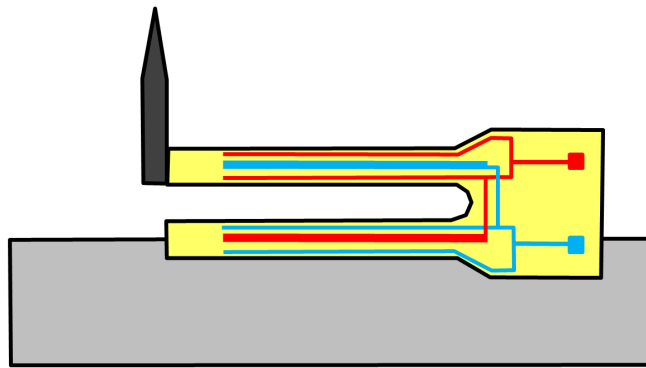


**Figure 2.6:** Schematic of a qPlus sensor. Red and light blue areas represent the two gold electrodes on the quartz tuning fork (yellow). One of the prongs and the base part of a quartz tuning fork is fixed with the holder while the tip is mounted to the second prong. Image readapted from Wikipedia.

### 2.2.2 Modes of AFM operation

Because of its versatility, the atomic force microscope has gone through many modifications for specific requirements. There are several AFM operating modes [28] but the most commonly operated modes are: i) contact mode, ii) non-contact mode, and iii) tapping mode.

The first and foremost mode of operation, the contact mode, is generally undertaken within the repulsive regime. The tip is dragged across the sample and the contours of the surface are used to construct the image. Forces

between the tip and the sample are maintained at a constant level using a feedback loop and the tip is kept fixed to the cantilever. The surface is scanned with piezoelectric motion of the tip. Because of involvement of strong forces between the tip and the sample in contact mode it is generally utilised only for stable, flat surfaces with very low or no roughness.

In non-contact mode, the AFM operates in the short-range regime and the cantilever (hence the tip) does not contact the sample. Rather it oscillates at or just above its resonant frequency, known as frequency modulation (FM) and amplitude modulation (AM) respectively. Non-contact AFM (NC-AFM) does not suffer from tip or sample degradation effects that are sometimes observed with contact mode. In frequency modulation the change in the oscillating frequency of the cantilever, because of tip-sample interaction is used in forming images of the surface of the sample. While in the amplitude modulation the change in amplitude is used. AM and FM operational techniques of NC-AFM are discussed below.

If the imaging is undertaken in ambient conditions or a fragile sample is used the preferred mode of operation is tapping mode, also known as dynamic contact mode. In tapping mode the tip oscillates with a large amplitude spending less time in close proximity to the sample thus reduces the damage on the surface because of tip contact compare to contact mode.

### 2.2.3 AM and FM operation of NC-AFM

In amplitude modulation the cantilever is oscillated just above its resonant frequency to detect the forces sensed by the tip by monitoring the amplitude of oscillation. As the tip is brought close to the sample, a small shift in the resonant frequency occurs due to tip-sample interaction. For an attractive force i.e. in the attractive regime, the frequency shift would be negative. If the driving frequency is made to be equal to the original resonant frequency then there will be a drop in the amplitude (Figure 2.7). The opposite is

## Scanning probe microscopy

---

true for a repulsive force. AFM images are generated by monitoring the changes in amplitude of the cantilever oscillation. A feedback loop, known as  $z$ -feedback, is used to keep the tip-sample interaction constant during the scan. The main disadvantage of AM operation is that the cantilever response time due to a perturbation is large. However, atomic resolution in the images can still be obtained as reported by Erlandsson *et al.* [29].

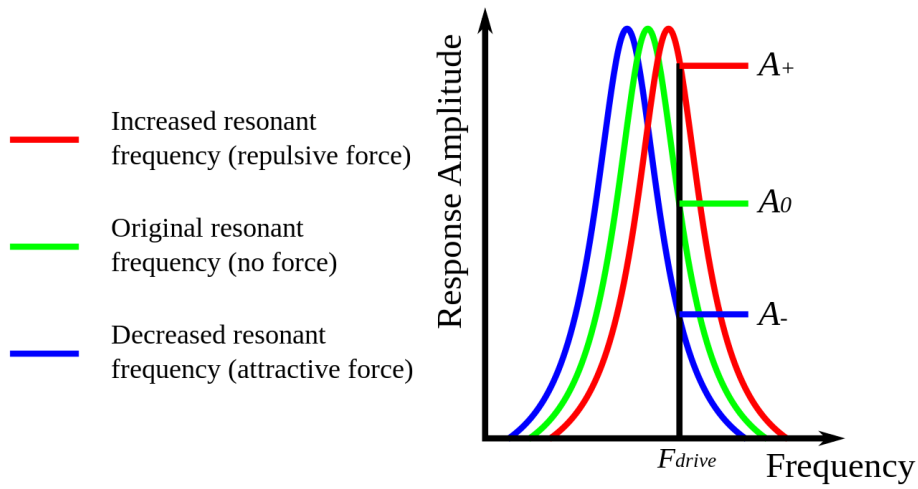


**Figure 2.7:** Change in resonant frequency of a cantilever due to tip-sample interaction in amplitude modulation technique. Image taken from Wikipedia.

The frequency modulation technique of AFM operation was introduced by Albrecht *et al.* [30] in 1991. In this operational mode, not only the amplitude of the cantilever is kept constant but also the cantilever is always oscillated at its resonant frequency. On-resonance operation is maintained by applying a  $90^\circ$  phase shift between the driving signal and the cantilever motion. The phase control can be performed in two ways. Either by self-exciting the cantilever with a  $90^\circ$  phase shifted signal or by using an advanced phase-locked loop (PLL) [31]. The PLL continuously tracks the oscillation frequency of the cantilever and its output is locked to a specific phase. The change in the resonant frequency of the cantilever is used to detect variations in the interaction force between the cantilever tip and

the sample studied and hence to construct the image of the sample. In the literature, these images are commonly referred as “frequency shift NC-AFM images”. During the operation an additional feedback loop is used to keep the amplitude of resonance constant. Compare to amplitude modulation which uses only one feedback loop (the  $z$ -feedback loop), frequency modulation uses three feedback loops which are the phase-locked loop, the amplitude loop, and the  $z$ -feedback loop. Despite this, frequency modulation is the dominant AFM technique and used extensively to study systems of interest.

### 2.3 Frequency shifts and tip-sample forces in frequency-modulation AFM

Though the oscillation frequency is the main observable in FM atomic force microscopy, a relation can be established between the observed frequency shift  $\Delta f$  and the physical tip-sample forces  $F_{ts}$ . This is important, because in simulating AFM images the forces acting between the tip and the sample is usually calculated. In frequency-modulation AFM, the oscillation amplitude  $A$  of a cantilever with natural frequency  $f_0$  and spring constant  $k$  is kept constant by using a positive feedback during the operation. When the oscillating cantilever is brought close to the sample, due to the force gradient  $k_{ts} = -\partial F_{ts}/\partial z$  between the tip of the cantilever and the sample, the oscillating frequency changes to  $f = f_0 + \Delta f$ . If the force gradient remains constant during the oscillation cycle, the frequency shift is given by [30]

$$\Delta f = \frac{f_0}{2k} k_{ts} = -\frac{f_0}{2k} \frac{\partial F_{ts}}{\partial z}. \quad (2.4)$$

If the force gradient is not constant during a cycle, the frequency shift can be calculated by first order perturbation theory (for  $|\Delta f| \ll f_0$ ) using the

## Scanning probe microscopy

---

Hamilton-Jacobi approach [32]

$$\Delta f(z_b) = -\frac{f_0^2}{kA} \int_0^{1/f_0} F_{ts}(z_b - A \cos(2\pi f_0 t)) \cos(2\pi f_0 t) dt, \quad (2.5)$$

where  $z_b$  is the vertical base position of the cantilever as shown in Figure 2.8.

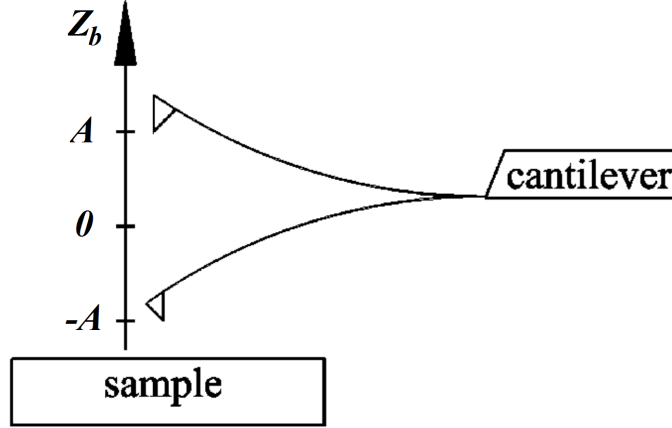


**Figure 2.8:** Schematic view of an oscillating cantilever with amplitude  $A$  is approached to a sample, while the frequency shift  $\Delta f$  is recorded as a function of the position of the base of the cantilever  $z_b$ . Image adapted from [28].

Substituting  $q' = A \cos(2\pi f_0 t)$  in Eq. (2.5) yields

$$\begin{aligned} \Delta f(z_b) &= \frac{f_0}{2k} \frac{2}{\pi A^2} \int_{-A}^A \frac{F_{ts}(z_b - q') q'}{\sqrt{A^2 - q'^2}} dq' \\ &= \frac{f_0}{2k} \frac{2}{\pi A^2} \int_{-A}^A F_{ts}(z_b - q') w(q', A) dq'. \end{aligned} \quad (2.6)$$

Integrating by parts we have

$$\begin{aligned} \Delta f(z_b) &= \frac{f_0}{2k} \frac{2}{\pi A^2} \int_{-A}^A k_{ts}(z_b - q') \sqrt{A^2 - q'^2} dq' \\ &= \frac{f_0}{2k} \langle k_{ts} \rangle. \end{aligned} \quad (2.7)$$

Which resembles the Eq. (2.4), except that  $k_{ts}$  is replaced by a weighted average of  $k_{ts}$ . For  $A \rightarrow 0$ , the weight function  $w(q', A)$  is a representation of Dirac's delta function and Eq. (2.7) yields the same result as Eq. (2.4).

In a real experiment,  $\Delta f(z_b)$  is not available as a continuous function, but as a set of discrete points. In that case Eq. (2.7) can be written as a set of linear equations [33].

## 2.4 Functionalized tip

Ideally the tip apex used in scanning probe microscopy should be atomically sharp, having a single atom at the apex of the tip. This is because the results obtained in SPM depend on sensing the interactions between the tip and the sample under study. In STM, to prepare a good tip, the tip state is changed mostly by deliberately crashing the tip into the sample or by applying voltage pulses. However, it is extremely difficult to determine the exact tip state from the STM or AFM images. This can be avoided by using a functionalized tip, which is usually done through deliberate adsorption of a chemical species prior to the actual scan. Thus the tip state can be assigned reliably, and the effect it has on the images obtained can be accounted for. Accurate description of the tip state can also be obtained through the interaction of the functionalized tip with a known surface structure, called inverse imaging.

The interaction, and hence the resolution of AFM images, crucially depends on the chemical nature of the tip termination. The resolution of an image can be dramatically enhanced by functionalizing the tip with a molecule or an atom that significantly contributes to the tip-sample interaction. Experimental molecular AFM images obtained by using a CO functionalized tip reveals features that have been interpreted as individual bonds within the sample molecule [14, 15, 34]. The same approach is used to measure the intermolecular forces between two molecules as a function of intermolecular separation [35]. The same technique can be used to understand the nature of the bonding between molecule and substrate. In addition, orientation dependant properties such as ordered structures observed on various forms

of monolayer can also be explored using the same concept.

## 2.5 Modeling SPM

The development of a comprehensive theoretical model to explain the numerous physical and chemical phenomena involved in SPM remain as a challenge to date. In spite of that a number of techniques are used for modelling the multi-electron system that are imaged in SPM.

### 2.5.1 Density functional theory

The most widely used, yet very computationally expensive, technique is the application of density functional theory (DFT), an iterative method for calculating electronic structure. DFT is also believed to be one of the highly accurate model so far, though for the overwhelming majority of multi-electron systems the solutions are found only numerically. In Kohn-Sham DFT [36], the electron density is first approximated, and then used within a set of equations known as the Kohn-Sham equations to obtain a set of Kohn-Sham orbitals. These orbitals are then used to generate a new estimate of the electron density and the process continues until the required accuracy is obtained. The accuracy of DFT largely depends on the approximations that are used to model the exchange-correlation interaction. A number of functionals such as the local density approximation (LDA) and generalised gradient approximations (GGA) are used to approximate the exchange-correlation interaction. The computational expense of applying DFT increases when complex systems or molecules with large numbers of atoms are considered. This is particularly true when modelling AFM, as the intermolecular interactions that are needed to incorporate increases with the system size, especially when vdW forces are considered [37]. Another difficulty may stem from modelling the tip [38,39] since the exact morphology

of the tip is not known.

Attempts have been made to minimize the computational expense by assuming the tip to be “chemically inert” [40] or using real-space pseudopotentials to describe the tip while studying partially periodic systems [41] within the DFT framework. These proposed schemes considered the tip as a semiclassical object without specifying its geometry and do not contain any Pauli or more generally exchange-correlation interactions. Usages of these assumptions produced good results for some systems but may not be valid for many cases, such as when contrast of AFM images change even within the same experiment [42].

### 2.5.2 Hückel molecular orbital theory

Models based on Hückel molecular orbital theory can be a computationally less expensive alternative to DFT. Both Hückel molecular orbital (HMO) theory and the related extended Hückel molecular orbital (EHMO) theory are semi empirical in type, and are limited in their applications, but nevertheless can be very useful. These theories express the electronic wavefunction i.e. the molecular orbital (MO) of a molecule as a linear combination of atomic orbitals (LCAO). HMO theory is the simplest one and the electronic basis is formed from  $\pi$  electrons only. In this method only the interactions between nearest neighbour atoms are considered, and all  $\sigma$  bonds are assumed to be negligible in determining the properties of a molecule. Though no integrals are explicitly evaluated in the HMO theory, it is usually accurate only for molecules having alternating single and double bonds. On the other hand EHMO theory not only includes the  $\sigma$  bonding into the calculation but also incorporates the interactions between all the atoms within the system. Though this requires the evaluation of the overlap integrals to calculate the matrix elements, like HMO theory it is also not an iterative method. In Chapter 4, we shall discuss the HMO and EHMO theories in greater detail.

### 2.5.3 Mechanical AFM model

Very recently, models have been proposed to simulate images obtained using a functionalized AFM tip based on the Lennard-Jones potential [43–45]. In all of these models, the tip is divided into two parts: i) the metal rigid end of the tip apex called *tip base* and ii) the flexible interactive end of the tip called *probe*. The interaction between the probe and the sample is calculated using the L-J potential though the actual form of the functionals that are used in these proposed model vary. The functionalized tip i.e. the probe, is allowed to relax during the simulation while remaining attached with the tip base. To describe the interaction between the metal end of the tip and the probe, in addition to the L-J potential lateral force constant is introduced. The model that we have adopted in our calculations will be described in detail in Chapter 4. Though these models are simple and quick, the parameters that are used to describe the interactions need to be tuned depending on the property of the system under study and the type of the tip used. Sometimes extra functions are also added in the model [46] to incorporate additional type of interactions (e.g. electrostatic interaction) depending on the studied system.

# Recent advances in submolecular resolution with NC-AFM

---

Though the existence of atoms and the concept of bonds between atoms have been known for a long time, the chemical structure of molecules was resolved, in real space, only in the past few years by using non-contact atomic force microscopy (NC-AFM) [14,34] and scanning tunnelling hydrogen microscopy (STHM) [47–49]. In these works individual atoms within the molecules were resolved, thereby visualizing the structure of the molecules. In the case of NC-AFM a CO-terminated tip was used, whereas in the case of STHM, molecular hydrogen was added into the gap between the tip and the sample. In this chapter we review the technical details of NC-AFM that is used for high resolution molecular imaging and summarise their implementations, advantages and limitations. We specially focus on the functionalization of the AFM tip and whether it is able to identify the single intermolecular bond uniquely.

### 3.1 Modification of the scanning probe

Atomic resolution of organic molecules in NC-AFM was achieved using a qPlus sensor [27] at low temperature (5 K). The tuning fork of the qPlus sensor is oscillated at its resonance frequency of about 30 kHz and the mode of operation is known as frequency-modulation [30]. During the scanning, the shift of the resonance frequency,  $\Delta f$  caused by the interaction between the tip and the sample is measured. To achieve atomic resolution, it is essential to detect the short range forces and in order to improve the sensitivity to those forces the tuning fork is required to oscillate with small amplitude, usually below 1 Å [28], which is facilitated by the large stiffness of the qPlus fork, normally about  $1800 \text{ Nm}^{-1}$ .

The resolution of the AFM images was also increased by exploiting a functionalized tip, which is done by picking up individual atoms or molecules by means of vertical atomic manipulation. In this process, the tip is first approached to a certain adsorbate, e.g. an atom [50] or a molecule [51]. Then the adsorbate is transferred from the sample to the end of the tip by applying a voltage pulse. Compared to other methods of tip preparation, which can be exchanging, heating or sputtering the tip, or even crashing the tip into the sample, this approach of tip preparation has two very important advantages. First, the exact atomic composition and the geometry of the tip is known, and, second, it is highly reproducible.

High contrast images in NC-AFM were only obtained when it was operated in the short-range regime in which case the image is constructed from the Pauli repulsion forces felt by the tip due to the molecule on the surface. When the tip is placed directly over the atoms or the bonds, the repulsion force is strongest because of the localization of the electron density directly above the atomic positions of the molecules. Thus produces images with atomic resolution. A tip which is able to produce such exceptional images must need to be (a) chemically inert, (b) atomically sharp, and (c) suffi-

ciently small to resolve atomic features. A CO-terminated tip has all these properties and is able to pass through the attractive regime to enter the repulsive regime [14]. For other non inert tips like Au-, Ag- or Cu-terminated tips, the large attractive force causes a manipulation instead of imaging the molecule under study. AFM tips functionalized with Cl, Br or Xe also provide good resolution but they are poorer in quality and sharpness compared to a CO-terminated tip [14, 52]. This is not only because of the smaller size of the O atom but also due to the flexibility of the CO molecule around the scanning tip apex. Figure 3.1 C shows the very first NC-AFM images revealing bond structure of an entire organic molecule which is obtained by a functionalized CO tip [14]. The NC-AFM image of cephalandole A, shown in Figure 3.2 B, obtained with a CO-terminated tip, is able to resolve the C–H bonds within the molecule [34].

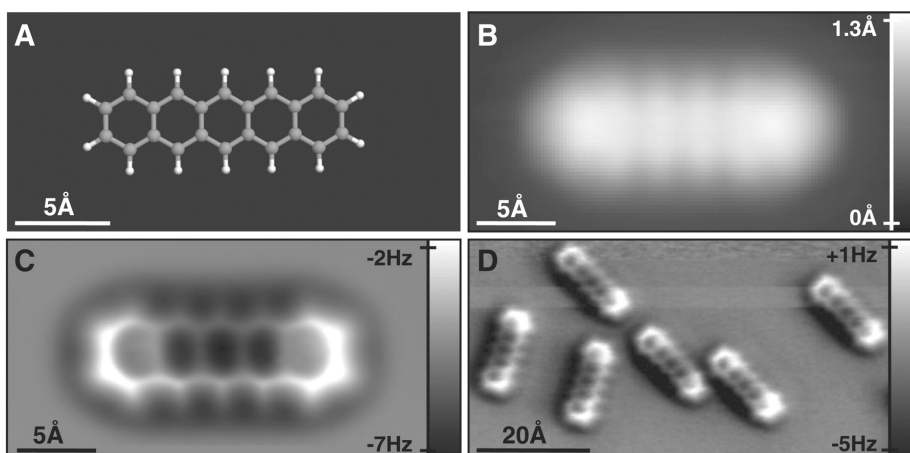


**Figure 3.1:** STM and AFM imaging of pentacene on Cu(111). (A) Ball-and-stick model of the pentacene molecule. (B) Constant-current STM and (C and D) constant-height AFM images of pentacene acquired with a CO-modified tip. Images are from ref. [14].

A comparison of the NC-AFM images of pentacene on NaCl(2ML)/Cu(111), acquired with different tip terminations (Ag-, CO-, Cl-, and pentacene-terminated tip), is shown in Figure 3.3. We see that tip functionalization is crucial for observing atomic contrast above the molecule and the highest resolution is obtained with a CO-terminated tip. In the NC-AFM images

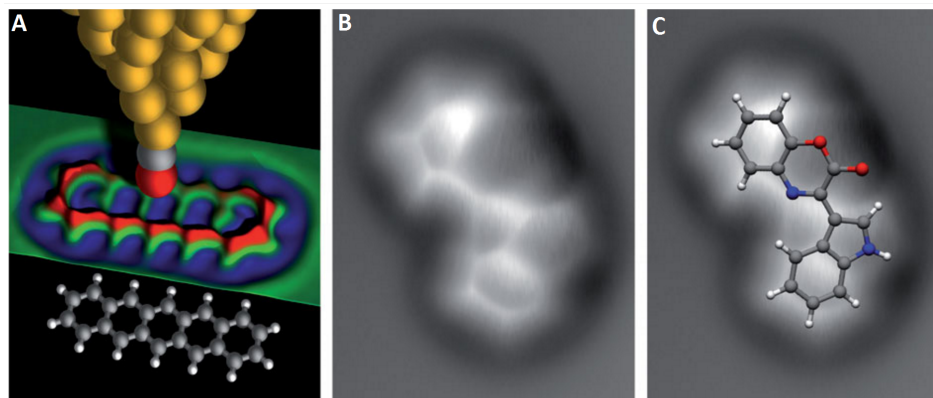


**Figure 3.2:** Constant-height NC-AFM measurements using CO-functionalized tips. (A) Model of a CO functionalized tip above a pentacene molecule. (B) Cephalandole A on NaCl(2ML)/Cu(111). (C) The same image as B with the molecular model of cephalandole A overlaid. Image A is taken from ref. [53] and images B and C are taken from ref. [34]

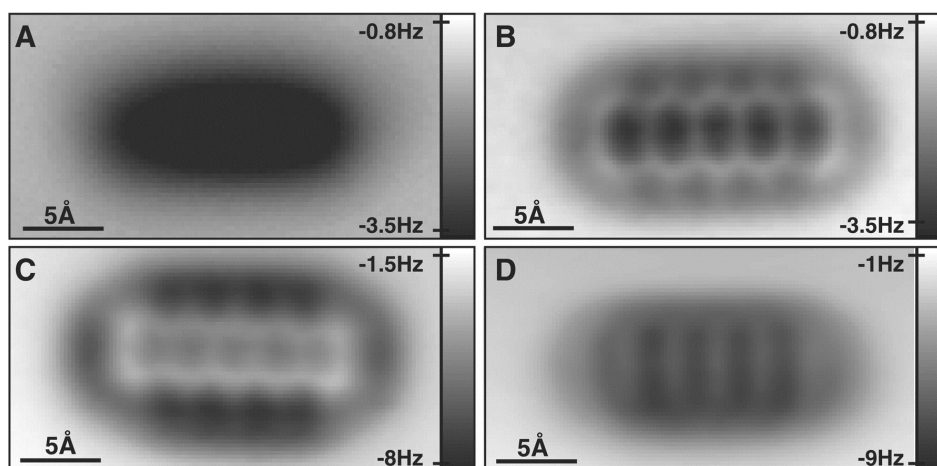


**Figure 3.3:** Constant-height AFM images of pentacene on NaCl(2ML)/Cu(111) using different tip modifications. (A) Ag tip, (B) CO tip, (C) Cl tip, and (D) pentacene tip. Images are from ref. [14].

of pentacene acquired with a Cl-terminated tip, the carbon rings appear smaller in diameter compared with those acquired with a CO-terminated tip, although both have similar spatial resolution.

One of the most exiting prospects of NC-AFM imaging with CO-terminated tip is that it can be used to identify a structure out of many possibilities unambiguously. It was shown in ref. [34] that NC-AFM can be used to resolve detailed molecular architecture. In addition, with a CO-terminated tip important information about the bond order can be acquired. The

## Recent advances in submolecular resolution with NC-AFM

bond order of individual carbon-carbon bonds within aromatic hydrocarbon was identified from the variation in bond lengths and brightness in the NC-AFM images of hexabenzocoronene (Figure 3.4 A) and fullerenes [15]. Subsequently this NC-AFM was used to investigate the mechanism of a thermal reaction (Figure 3.4 B) in which the structure of the molecule was determined using a functionalized CO tip before and after annealing at 90 °C [17].

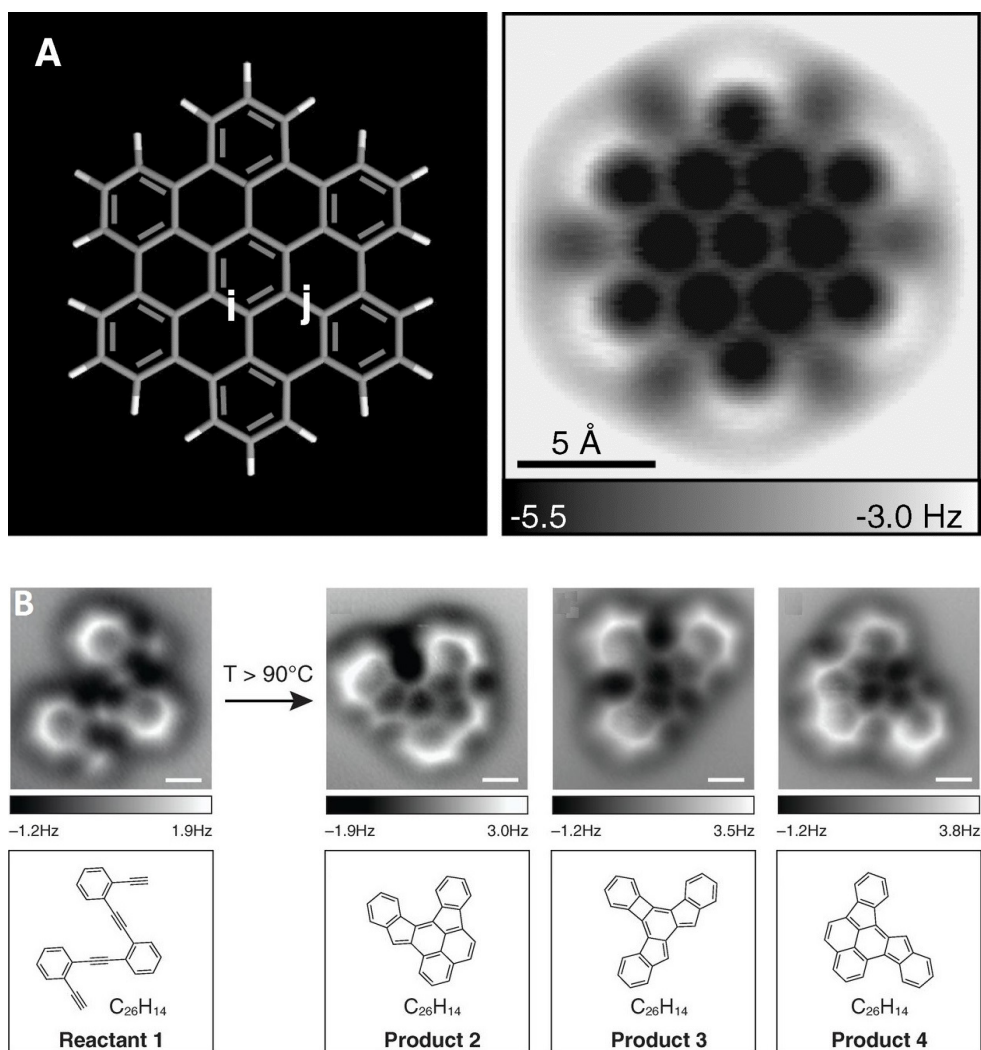


**Figure 3.4:** (A) Model and NC-AFM image of hexabenzocoronene showing discrimination in thickness depending on bond order (taken from ref. [15]). (B) NC-AFM images and schematic representation of the molecular structure before and after thermal reaction (taken from ref. [17]).

### 3.2 Flexibility of the CO-terminated tip

Ideally, an AFM tip should be atomically sharp and rigid to image the interactions within the system being studied. However, when a metallic and atomically sharp tip is used, it modifies the system because of its interaction with the system instead of imaging the interactions in the system [14]. To date, in all of the NC-AFM studies where enhanced contrast within and between the molecules is achieved, a CO-terminated tip is used, except for naphthalene tetracarboxylic diimide (NTCDI) on Si(111)-(7×7) surface, reported by Sweetman *et al.* [18], where the tip was not functionalized deliberately. Sun *et al.* [35], by studying the pair potential between two CO molecules showed that metal-adsorbed CO molecules are not rigid, but show a great deal of flexibility and undergo relaxation as the tip-sample distance is decreased.

Gross *et al.* in 2012 [15] showed that variation in the bond lengths between  $h$  (bond fusing between two hexagons) and  $p$  (bond fusing between a pentagon and a hexagon) bonds can be imaged using NC-AFM with a functionalized CO tip (Figure 3.5). The  $h$  bond, which is higher in order compared to the  $p$  bond, appears smaller in length compared to the  $p$  bond. They reproduced the experimental results using density functional theory (DFT) by modeling CO as a flexible tip and showed that tilting of the CO molecule at the tip apex is greater above the  $h$  bonds compared with the  $p$  bonds i.e. the variation in the bending of the CO molecule at the tip apex depends on the variation in the electron density across the molecule under study. Because of the bending of the CO molecule at the tip apex due to its interaction with the sample, the molecular geometry in the NC-AFM images appear considerably distorted [43, 54–57]. Neu *et al.* [56] proposed a technique to correct the distortions in the NC-AFM images assuming that the bending of the CO molecule at the tip apex depend linearly on the lateral forces acting on the tip cantilever. Comparing the original and de-skewed NC-AFM

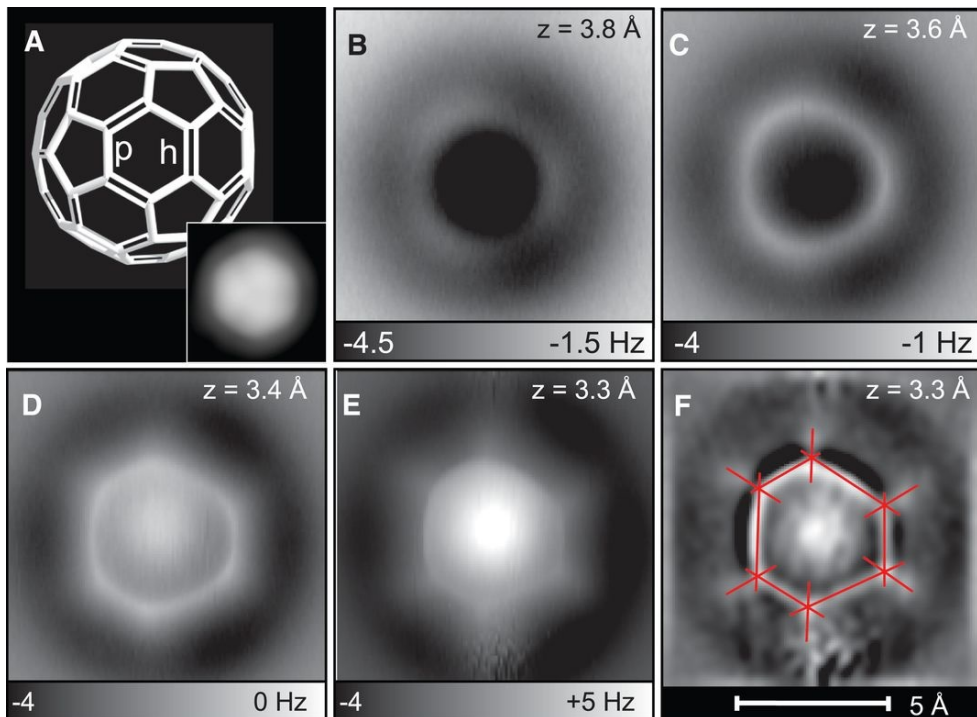


**Figure 3.5:** Variation in bond order in C<sub>60</sub>. (A) Model of C<sub>60</sub> showing that *p* and *h* bonds. Inset is the STM image of C<sub>60</sub> molecule. (B to E) NC-AFM images of C<sub>60</sub> obtained using CO-functionalized tip at decreasing tip-sample separation. The difference between *p* and *h* bonds become more and more visible as the tip approaches the sample. (F) Laplace-filtered and flattened image of E to highlight differences in bond lengths. Images are from ref. [15].

images of pentacene molecules adsorbed on Cu(111) and on NaCl/Cu(111) films (Figure 3.6), they found that the C–C bond length in the molecule can appear 40-100% larger in length than the actual value. Therefore, it is crucial to obtain NC-AFM images with CO-terminated tip where the distortion will be minimized, but at the same time the clarity and sharpness of the images will be maintained.

On the other hand, NC-AFM images of the assemblies of organic molecules obtained with a functionalized CO tip show intermolecular contrast [58, 59] which has been ascribed to intermolecular bonds (Figure 3.7). Hapala *et al.* [44] reproduced the experimental results reported in ref. [59] (Figure 3.7 B) by using a model based on pairwise Lennard-Jones potentials. They modelled the CO-terminated tip as a flexible probe, which is allowed to relax during the simulation, attached to a rigid metallic tip base. De-

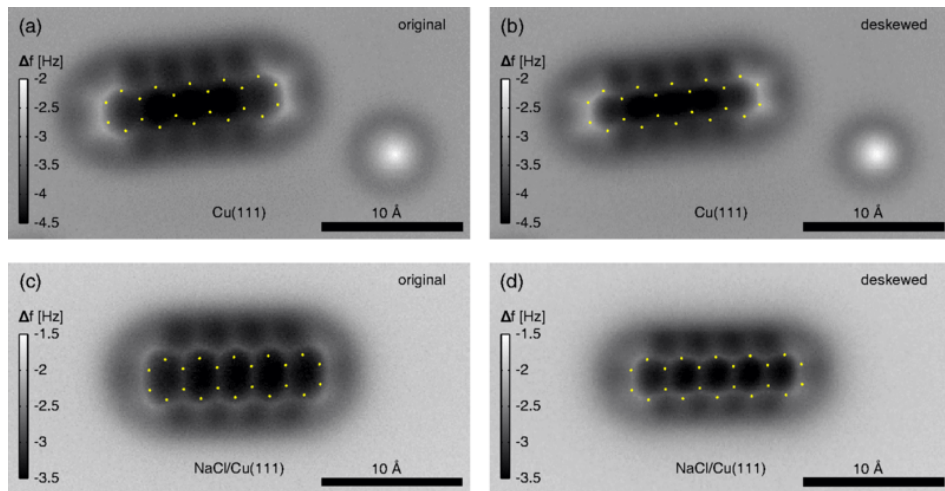


**Figure 3.6:** Original (a and c) and de-skewed (b and d) images of individual pentacene molecules adsorbed on Cu(111) and on NaCl/Cu(111). Dots indicate the positions of carbon atoms in the known geometry of pentacene reported in ref. [60]. Images are taken from ref. [56].

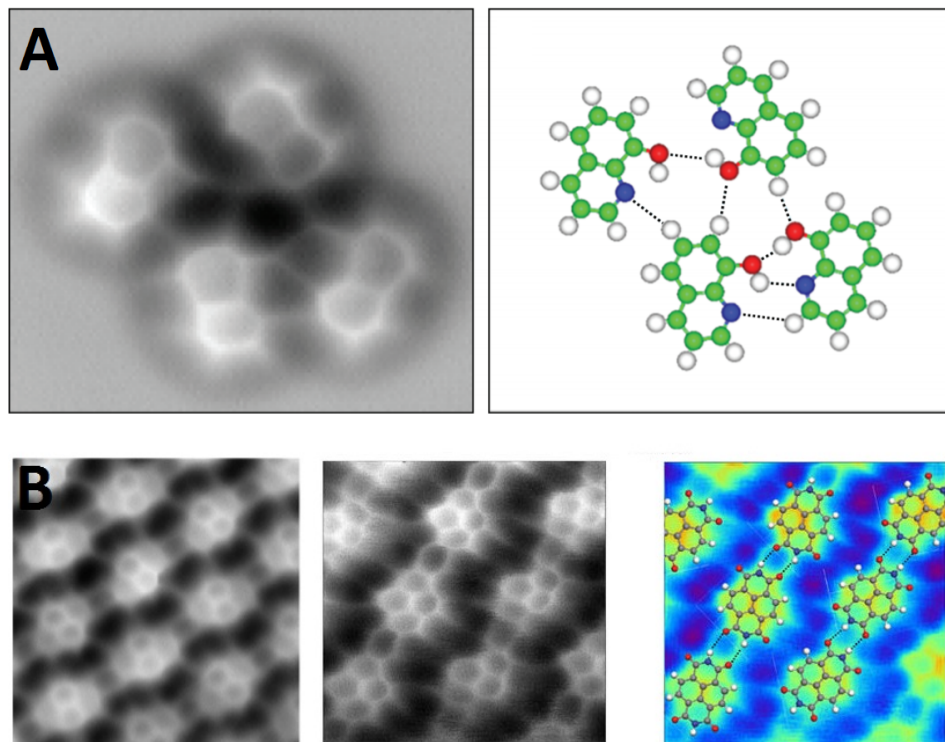


**Figure 3.7:** NC-AFM images of molecular assemblies exhibiting features in the locations of hydrogen bonding obtained with CO-terminated tip. (A) Constant-height NC-AFM image of 8-hydroxyquinoline assembly on Cu(111) and the corresponding structure model. (B) Constant height NC-AFM images of NTCDI island on Ag:Si(111)-( $\sqrt{3} \times \sqrt{3}$ ) R30° surface and overlay of the model of NTCDI on a contrast-adjusted image. Images in A are taken from ref. [58] while images in B are taken from ref. [59].

spite the fact that the model does not include any electrostatic interactions, whereas hydrogen bonds primarily originate from electrostatic interaction and may include dispersion, covalency, and exchange contributions (according to the IUPAC definition published in 2011 [61]), Hapala *et al.*'s model can reproduce bond like features between molecules when the flexibility of the CO-terminated tip is taken into account (Figure 3.8). However, when the CO-terminated tip is assumed to be rigid i.e. the CO molecule attached to tip apex is not allowed to bend, the model show no such features between the molecules even at very small tip-sample separation.

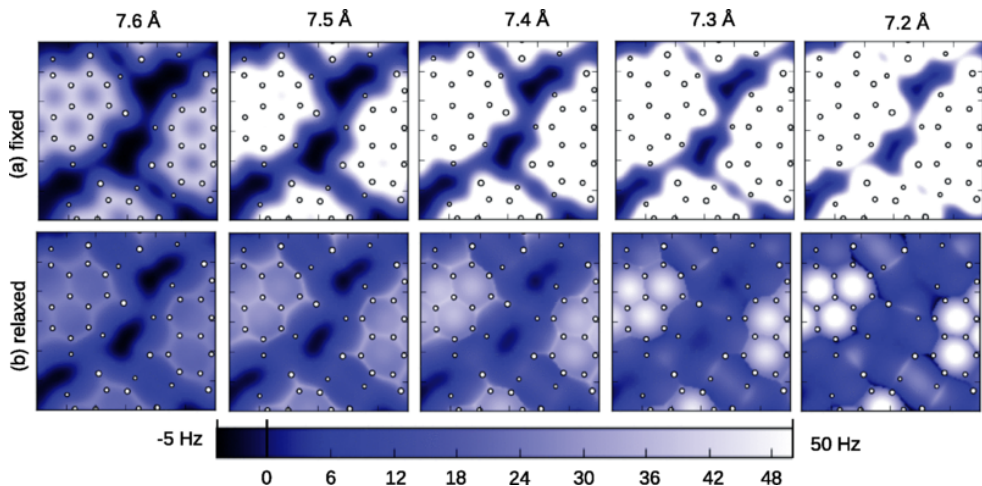


**Figure 3.8:** Simulated constant-height NC-AFM images of NCTDI with functionalized CO tip at decreasing tip-sample separation. No intermolecular contrast is visible when a rigid tip is used (a) and the feature is only apparent is the tip is allowed to relax during simulation. Images are taken from ref. [44].

Amazingly, DFT simulations, which take into account the electrostatic interactions, of CO-terminated NC-AFM images of four bis(para-pyridyl)acetylene (BPPA) molecules in a tetramer stabilized by hydrogen bonding, reported by Hämäläinen *et al.* [45], do not produce any intermolecular contrast (Figure 3.9). The NC-AFM images of the same system show intermolecular contrast where hydrogen bonds are present and also where no bond is present. Using a similar model as Hapala *et al.* i.e. modeling the CO tip is as a flexible end attached to the tip apex, Hämäläinen *et al.* reproduced the

experimental observations (Figure 3.9). These results suggest that the flexibility of the CO-terminated tip, not necessarily the intermolecular bond, determines the appearance of intermolecular contrast. This gives rise to the question: can we describe the submolecular contrast observed in NC-AFM images obtained with CO-terminated tip as a real space mapping of the intermolecular bond?

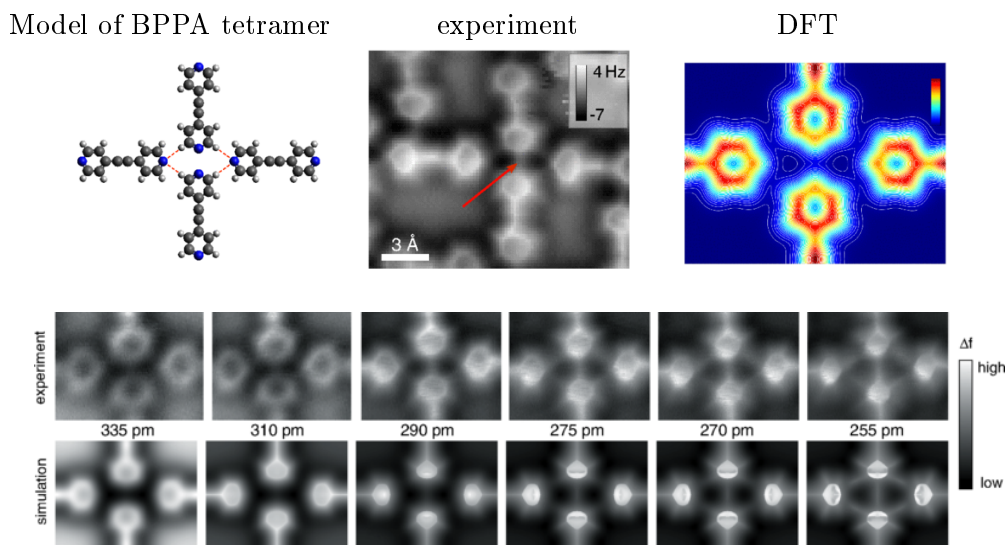


**Figure 3.9:** Experimental and simulated constant-height of NC-AFM images of BPPA tetramer. Intermolecular features are seen in NC-AFM images obtained with CO-terminated tip at the place where no bond is present (red arrow) though no sign of intermolecular bond is observed in DFT calculation. Bottom two rows show experimental and simulated results at decreasing tip-sample separation. In the simulation the CO tip is modelled as a flexible end attached to the tip apex. Images are taken from ref. [45].

### 3.3 Conclusions

The development in NC-AFM, specifically the use of a functionalized tip, enabled us to study systems in unprecedented resolution. The flexibility of the molecular tip not only allows us to visualize the C–C bonds in systems but also in some cases reveal the order of the C–C bonds. At the same time, the flexibility of the molecular tip introduces a distortion in the im-

## **Recent advances in submolecular resolution with NC-AFM**

ages which causes a significant deviation from the true atomic structure of the system. The tip induced distortion sometime produces intermolecular contrast when no bonds are present between the molecules. Since, it is still a very developing technique, it will be too early to use NC-AFM with a functionalized tip to identify the presence of hydrogen bond in a system without any prior knowledge. The study of a variety of systems, both theoretically and experimentally, which are not necessarily planar and stabilized through bonds other than hydrogen bond, will enhance our understanding of the mechanism involved in tip functionalized NC-AFM.

# Theoretical basis

---

A number of previously developed theories will be required throughout the work. Before starting the investigation it is important to have an overview of those techniques. We start the chapter with an overview of Hückel molecular orbital theory and its extensions with examples. Following that we shall discuss briefly about STM theory i.e. how tunnelling current can be used theoretically to simulate STM images. We shall also discuss theoretical models of simulating STM and AFM images. Finally a brief overview of Kohn-Sham DFT, which is used for optimizing the geometry of the network of bi-isonicotinic acid molecules, will be given. The relaxed geometry of the assembly is then used in simulating the AFM images of the island of bi-isonicotinic acid molecules.

### 4.1 Hückel theory for molecular orbitals

Hückel molecular orbital (HMO) theory expresses the electronic wavefunction i.e. the molecular orbitals (MO) of a molecule, as a linear combination of atomic orbitals, mathematical expressions describing the wave-like behavior of electrons within a molecule. Electrons in a molecule are associated

## Theoretical basis

---

with MOs of different energy, just as the electrons in an atom are associated with atomic orbitals (AOs) of different energy. Thus, electrons added to a molecule occupy the MOs in order of increasing energy (like electrons in an atom occupy AOs). The highest energy filled MO is referred as the highest occupied molecular orbital (HOMO), while the next highest energy MO is referred as the lowest unoccupied molecular orbital (LUMO). Together, the HOMO and the LUMO form the frontier orbitals of a molecule.

### 4.1.1 Simple HMO theory

Hückel molecular orbital theory uses a linear combination of atomic orbitals (LCAOs) associated with each atom for the determination of the energies of the MOs of the molecules, where the atomic bonding within the molecule is dominated by  $\pi$  bonding. Any  $\sigma$  bonding that is present is assumed to have a negligible contribution in determining the molecular properties of the molecule. Each atom contributes a single electron to the  $\pi$  bonding within the molecule. The basis of AOs used to construct the linear combination is the set of  $p_z$  orbitals associated with each atom, pointing outwards from the molecule. The overlapping between the orbitals is neglected and the orbitals are considered orthogonal:

$$S_{ij} = \langle \psi_i | \psi_j \rangle = \begin{cases} 1 & \text{if } i = j \\ 0 & \text{if } i \neq j \end{cases} \quad (4.1)$$

i.e. the overlap matrix is an identity matrix. A Hückel Hamiltonian is constructed which incorporates the kinetic and potential energies of the electron on the diagonal elements and the interaction between adjacent orbitals only on the off diagonal terms. Any interaction between next nearest neighbours

## Theoretical basis

---

and greater is neglected. This can be formulated mathematically as follows:

$$H_{ii} = \langle \psi_i | \mathcal{H} | \psi_i \rangle = \alpha \quad (4.2)$$

$$H_{ij} = \langle \psi_i | \mathcal{H} | \psi_j \rangle = \begin{cases} \beta & \text{if the atoms are adjacent} \\ 0 & \text{otherwise} \end{cases} \quad (4.3)$$

The term  $\alpha$  is the Coulomb integral which represents the total kinetic and potential energy associated with the electron present in the  $p$  orbital of atom  $i$ . The term  $\beta$  is referred to as the resonance integral between directly-bonded atoms and represents the energy of an electron in the region between atoms where the atomic orbitals overlap. Hence  $\beta$  is negative in magnitude. However, to obtain the eigenvalues and eigenvectors it is not necessary to know the values of  $\alpha$  and  $\beta$ . Instead, the secular equation is divided by  $\beta$ , resulting a Hamiltonian that has the same unknown on each diagonal element. This way eigenvectors are calculated correctly but eigenvalues are given as a function of  $\alpha$  and  $\beta$ . Hence the simple HMO theory becomes incredibly quick without using any empirical data and without any integrals being calculated.

The wavefunction of the  $i$ th MO of the  $\pi$  orbital system can be written as

$$\Psi_i = \sum_j c_{ij} \psi_j \quad (4.4)$$

where the index  $j$  runs over all the atoms in the molecule and  $c_{ij}$  corresponds to the weight of that particular  $p$  orbital in the  $i$ th MO i.e. the portion of  $\psi_j$  in  $\Psi_i$  as dictated by the corresponding eigenvector of the Hückel Hamiltonian.

To illustrate simple Hückel theory with an example, consider butadiene,  $C_4H_6$  ( $CH_2=CH-CH=CH_2$ ). We know electrons in hydrogen atoms are in the  $1s$  orbital and they contribute to the  $\sigma$ -bonding only. Since HMO theory only relies on the  $\pi$ -bonding network, no  $\sigma$ -bonds are considered.

## Theoretical basis

---

Therefore, the determinant becomes as follows

$$\begin{bmatrix} \alpha - E & \beta & 0 & 0 \\ \beta & \alpha - E & \beta & 0 \\ 0 & \beta & \alpha - E & \beta \\ 0 & 0 & \beta & \alpha - E \end{bmatrix} = 0 \quad (4.5)$$

using  $E' = -(\alpha - E)/\beta$ , we obtain from Eq. (4.5)

$$\begin{bmatrix} -E' & 1 & 0 & 0 \\ 1 & -E' & 1 & 0 \\ 0 & 1 & -E' & 1 \\ 0 & 0 & 1 & -E' \end{bmatrix} = 0. \quad (4.6)$$

Which gives the secular equation in a simpler form for  $C_4H_6$

$$\hat{\mathcal{H}}\Psi = \begin{bmatrix} 0 & 1 & 0 & 0 \\ 1 & 0 & 1 & 0 \\ 0 & 1 & 0 & 1 \\ 0 & 0 & 1 & 0 \end{bmatrix} \Psi = E' \Psi. \quad (4.7)$$

This gives a purely numerical matrix known as the Hückel Hamiltonian,  $\hat{\mathcal{H}}$ , and is simple to diagonalise. In obtaining Eq. (4.7) from Eq. (4.5) the basis remains the same but at the end energies are given in terms of unknown variables.

### 4.1.2 Modified HMO theory for heteroatom System

So far, the Hückel theory we have discussed is only for systems involving hydrocarbons with several carbon-carbon double bonds, specially one having a chain of alternating single and double bonds. In reality many molecules of interest like  $C_{60}F_{48}$ , phthalocyanine ( $C_{32}H_{16}N_8$ ), etc. involve “foreign” atoms. These atoms, which are in a similar state of hybridization to car-

## Theoretical basis

---

bon, can contribute vacant, singly occupied, or doubly occupied orbitals to the  $\pi$ -system of the molecule. Therefore, the different electronegativities of atoms must be taken into account in assigning Coulomb integral values. This is normally done by scaling all Coulomb integrals in terms of the standard value  $\alpha_0$ , plus some fraction of standard bond integral  $\beta_0$ . For an atom X, the Coulomb integral then becomes

$$\alpha_X = \alpha_0 + h_X \beta_0 \quad (4.8)$$

where  $h_X$  is an empirical and dimensionless constant that is characteristic of X, and depends i) on the electronegativity difference between X and carbon and ii) on the number of electrons that X can or does contribute to the delocalized  $\pi$ -system.

Similarly when heteroatoms are considered the properties of C–X bonds can no longer be considered to be the same as those of C–C bonds. In this case the bond integral terms are also scaled empirically with reference to a standard C–C bond integral as

$$\beta_{C-C} = k_{C-C} \beta_0 \quad (4.9)$$

$$\beta_{C-X} = k_{C-X} \beta_0 \quad (4.10)$$

where  $k_{C-C}$  is taken as unity for all normal C–C bonds in polyenes, some value less than unity for longer bonds and greater than unity for shorter bonds. This allows the bond integral to vary from system to system. Mostly, the C–C bond length in  $sp^2$  hybridized systems is between 1.34 & 1.45 Å, and  $k_{C-C}$  is set equal to unity. The  $k_{C-X}$  for internuclear distance are estimated from calculated  $2p_z$ -type overlaps [62].

The values of  $k_{C-C}$  as a function of C–C bond length and values of  $h_X$  and  $k_{C-X}$  for different atoms are tabulated by Yates [63]. As an example for fluorine the scaling factors are  $h_F = 3.0$  and  $k_{C-F} = 0.7$ . It is to be noted that the inclusion of heteroatoms generally reduces the symmetry of the

system so that calculations may become more difficult.

### 4.1.3 Extended HMO theory

An extension of simple Hückel approach, developed by Hoffmann [64], is widely employed and in many cases very useful and is also free from unknowns like  $\alpha$  and  $\beta$ . Extended Hückel molecular orbital (EHMO) theory takes into account all the atoms in the molecular system. Moreover all orbitals on each atom that are part of its valence shell, whether these AOs are occupied in the free atom or not, are considered in calculation. It also includes the overlaps between all the atomic orbitals considered, not just nearest neighbour (i.e. no  $S_{ij}$  are assumed to be zero). To calculate all  $S_{ij}$  values it is necessary to know the molecular geometry in terms of bond length and bond angle. Thus the coordinates of every atom must be specified.

Coulomb integrals,  $H_{ij}$ , are not calculated explicitly, but for all normally occupied atomic orbitals (or subshells) they are taken to be equal to the appropriate valence state ionization potentials (VSIP) that are available in the literature in many cases [65]. For AOs in the basis set that are normally vacant, the Coulomb integrals are taken to be equal to the appropriate electron affinity values.

The bond integrals are assigned numerical values based on the Wolfsberg-Helmholtz approximation [66], where

$$H_{ij} = K \cdot \frac{H_{ii} + H_{jj}}{2} \cdot S_{ij}. \quad (4.11)$$

This is a reasonable approximation, since the Coulomb integral for an interaction between two orbitals  $i$  and  $j$  should be related to the energies of electrons in the individual AOs, as well as to the degree of overlap between them. The best value of the constant  $K$ , which is used as a scaling factor, is 1.75, although the final results are not very sensitive to the precise value

## Theoretical basis

---

of  $K$  used [63].

On the above basis, the complete secular determinant is then solved to obtain the eigenvalues and the coefficients. The major differences between EHMO and the HMO are that all valence orbitals on all atoms are included, all off-diagonal elements are retained and overlap is fully included, and finally energies are obtained as numerical quantities, not in terms of  $\alpha$  and  $\beta$ .

### 4.1.4 Gaussian type orbital

In this work we have used Gaussian type orbitals (GTO) rather using hydrogen-like orbitals or Slater type orbitals (STO) for our basis sets. Hydrogen-like orbitals are exact solutions to the non-relativistic Schrödinger equations for a single electron system. For many-electron systems, they are considered to be very accurate but the presence of radial nodes makes the calculation problematic, specially when integrations are involved. A very good alternative is STOs

$$S_{nlm}^{\zeta}(r, \theta, \phi) = N Y_l^m(\theta, \phi) r^{n-1} e^{-\zeta r}, \quad (4.12)$$

introduced by J. C. Slater [67], which are not only free of nodes but also decay in the same way as hydrogen-like functions do.  $N$  is the normalization factor,  $n$  is the principal quantum number of the orbital,  $Y_l^m(\theta, \phi)$  is the spherical harmonics,  $l$  and  $m$  are the angular momenta quantum numbers and  $\zeta$  is called Slater exponent. The value of  $\zeta$  depends on the effective nuclear charge of the atom. Though STOs are good alternatives for hydrogen-like orbitals, especially for calculations involving long range interactions, the pre-exponential factor  $r^{n-1}$  and  $r = \sqrt{x^2 + y^2 + z^2}$  in the exponential make the analytic calculations extremely difficult in most cases.

Calculations can be made faster and simpler by using GTO, first introduced

## Theoretical basis

---

by S. F. Boys [68], defined as

$$G_{ijk}^{\alpha}(\mathbf{r}) = N_{ijk}^{\alpha} x^i y^j z^k e^{-\alpha r^2}, \quad (4.13)$$

where  $N_{ijk}^{\alpha}$  is the normalization factor, and  $\alpha$  is called the exponent of the Gaussian function. GTOs are also free of nodes and most importantly the exponent  $r^2 = x^2 + y^2 + z^2$  makes the calculation simpler and faster by allowing variables to be handled independently. GTOs are not really orbitals but simpler functions, frequently called gaussian primitives and usually obtained from quantum calculations on atoms e.g. Hartree-Fock or Hartree-Fock with some correlated calculations. For molecular calculations, certain linear combinations of them are used as basis functions with fixed coefficients and exponents. By summing over multiple Gaussian primitives the accuracy of the basis can be increased and also long range interactions can be included. However, increasing the number of Gaussians increases computational time, so a balance should be made between accuracy and speed in choosing the basis set.

Among all the GTOs, the STO- $n$ G are the most popular minimal basis sets, where  $n$  primitive Gaussian orbitals are fitted to a single STO. For example, an STO-3G basis set for the  $1s$ ,  $2s$  and  $2p$  orbital of the carbon atom are all linear combination of 3 primitive Gaussian functions. So a STO-3G  $s$  orbital is given by

$$\psi_{\text{STO-3G}}(s) = c_1 \phi_1 + c_2 \phi_2 + c_3 \phi_3, \quad (4.14)$$

where

$$\phi_i = \left( \frac{2\alpha_i}{\pi} \right)^{3/4} e^{-\alpha_i(x^2+y^2+z^2)}; \quad \{i = 1, 2, 3\}. \quad (4.15)$$

The constants  $c_i$  and  $\alpha_i$  are determined by least square fit. For STO- $n$ G these sets were obtained by fitting the combination of  $n$  gaussian functions to a STO of the same type. The advantage of STO- $n$ G basis set over other

GTOs is that common exponents ( $\alpha$ 's) are used for orbitals in the same shell (e.g.  $2s$  and  $2p$ ) which allows more efficient computation [69].

## 4.2 Simulating STM images using Hückel MO theory

The tunnelling current in STM between the tip and the sample is proportional to the probability of a transition occurring between electronic states of them. Using first-order perturbation theory, it can be shown that the transition probability of an electron between the states  $\chi$  (tip wavefunction) and  $\psi$  (sample wavefunction) is given by Fermi's golden rule

$$P = \frac{2\pi}{\hbar} |M|^2 \delta(E_\chi - E_\psi), \quad (4.16)$$

where the delta function ensures the elastic tunnelling condition which requires  $E_\chi = E_\psi$  i.e. the tunnelling only occurs between sites of equivalent energy. According to Bardeen tunnelling theory [70], a tunnelling matrix element,  $M$  is evaluated only in the volume of the tip,  $\Omega_\chi$  and has the form

$$M = \int_{\Omega_\chi} \chi^* U_\chi \psi d\tau. \quad (4.17)$$

To find  $M$  we first write the Schrödinger equations for tip and sample

$$\left( -\frac{\hbar^2}{2m} \nabla^2 + U_\chi \right) \chi = E_\chi \chi \quad (4.18)$$

$$\left( -\frac{\hbar^2}{2m} \nabla^2 + U_\psi \right) \psi = E_\psi \psi, \quad (4.19)$$

where  $m$  is the mass of electron and  $U$  is potential energy.

Using Schrödinger equation for the tip states, Eq. (4.18), the matrix element

## Theoretical basis

---

is converted into

$$\begin{aligned}
M &= \int_{\Omega_\chi} \psi U_\chi \chi^* d\tau \\
&= \int_{\Omega_\chi} \psi \left( E_\chi + \frac{\hbar^2}{2m} \nabla^2 \right) \chi^* d\tau \\
&= \int_{\Omega_\chi} \left( \chi^* E_\chi \psi + \frac{\hbar^2}{2m} \psi \nabla^2 \chi^* \right) d\tau. \tag{4.20}
\end{aligned}$$

Because of the elastic tunnelling condition,  $E_\chi = E_\psi$ , Eq. (4.20) can be converted into

$$\begin{aligned}
M &= \int_{\Omega_\chi} \left( \chi^* E_\psi \psi + \frac{\hbar^2}{2m} \psi \nabla^2 \chi^* \right) d\tau \\
&= \int_{\Omega_\chi} \left( \chi^* \left( -\frac{\hbar^2}{2m} \nabla^2 + U_\psi \right) \psi + \frac{\hbar^2}{2m} \psi \nabla^2 \chi^* \right) d\tau, \tag{4.21}
\end{aligned}$$

where Eq. (4.19) is used and since  $U_\psi$  is zero at the tip, we obtain

$$M = -\frac{\hbar^2}{2m} \int_{\Omega_\chi} (\chi^* \nabla^2 \psi - \psi \nabla^2 \chi^*) d\tau. \tag{4.22}$$

For both tip states and sample states near the Fermi level, the wavefunctions satisfy Schrödinger equation in the vacuum,

$$(\nabla^2 - \kappa^2) \chi(\mathbf{r}) = 0, \tag{4.23}$$

where  $\kappa$  is the decay constant. The Green's function for the above Schrödinger equation (Eq. (4.23)) is defined by the differential form [71]

$$(\nabla^2 - \kappa^2)G(\mathbf{r} - \mathbf{r}_0) = -\delta(\mathbf{r} - \mathbf{r}_0) \tag{4.24}$$

with the boundary condition that it is regular at  $|\mathbf{r} - \mathbf{r}_0| \rightarrow \infty$ . The explicit form of the Green's function is

$$G(\mathbf{r} - \mathbf{r}_0) = \frac{\exp(-\kappa|\mathbf{r} - \mathbf{r}_0|)}{4\pi|\mathbf{r} - \mathbf{r}_0|}. \tag{4.25}$$

## Theoretical basis

---

Therefore, the  $s$ -type spherical harmonic representing the tip wavefunction can be written as a Green's function

$$\chi_s(\mathbf{r}) \propto G(\mathbf{r} - \mathbf{r}_0), \quad (4.26)$$

centered at the tip apex  $\mathbf{r}_0$ . The conditions that the sample wavefunction,  $\psi$  satisfies the Schrödinger equation, Eq. (4.23), in  $\Omega_\chi$ , and that the Green's function satisfies Eq. (4.24) lead us to

$$\begin{aligned} M_s &\propto \int_{\Omega_\chi} [G(\mathbf{r} - \mathbf{r}_0)\nabla^2\psi(\mathbf{r}) - \psi(\mathbf{r})\nabla^2G(\mathbf{r} - \mathbf{r}_0)] d\tau \\ &\propto \psi(\mathbf{r}_0) \end{aligned} \quad (4.27)$$

which was derived first by Tersoff and Hamann [72, 73] using the Fourier transform method.

Hence we can say that if the tip is considered as a simple  $s$ -type atomic orbital associated with a single atom, the matrix element is proportional to the wavefunction of the sample orbital determined at the tip centre only. This leads us to the conclusion that the tunnelling current in STM for a  $s$ -type tip is proportional to the square of the wavefunction of the sample orbital determined at the tip centre.

### 4.2.1 Derivative rule for tip state

The tunnelling matrix elements for other components of tip wave function can be obtained in virtue of the relation between tip wave functions and the Green's function. For example, it can be shown that the tip wave function for the  $p_z$  states is [74]

$$\chi_{p_z}(\mathbf{r}) \propto \frac{\partial}{\partial z_0} G(\mathbf{r} - \mathbf{r}_0). \quad (4.28)$$

## Theoretical basis

---

How tip wave functions of different state are related to the derivatives of Green's function is discussed in references [22, 74]. From our previous discussion, we can write

$$\psi(\mathbf{r}_0) \propto \int_{\Omega_\chi} [G(\mathbf{r} - \mathbf{r}_0) \nabla^2 \psi(\mathbf{r}) - \psi(\mathbf{r}) \nabla^2 G(\mathbf{r} - \mathbf{r}_0)] d\tau. \quad (4.29)$$

Taking the derivative with respect to  $z_0$  on both sides keeping in mind that  $z_0$  only appears in the Green's function and does not involve in the integration process, we can write

$$\frac{\partial}{\partial z_0} \psi(\mathbf{r}_0) \propto \int_{\Omega_\chi} \left[ \frac{\partial}{\partial z_0} G(\mathbf{r} - \mathbf{r}_0) \nabla^2 \psi(\mathbf{r}) - \psi(\mathbf{r}) \nabla^2 \frac{\partial}{\partial z_0} G(\mathbf{r} - \mathbf{r}_0) \right] d\tau. \quad (4.30)$$

From Eqs. (4.28) and (4.30), we now have

$$\begin{aligned} \frac{\partial}{\partial z_0} \psi(\mathbf{r}_0) &\propto \int_{\Omega_\chi} [\chi_{p_z} \nabla^2 \psi - \psi \nabla^2 \chi_{p_z}] d\tau \\ &\propto M_{p_z} \end{aligned} \quad (4.31)$$

i.e. the tunnelling matrix element for a  $p_z$  tip state is proportional to the  $z$  derivative of the sample wave function centered at the tip apex  $\mathbf{r}_0$ . Tunnelling matrix elements for all the tip states as derived by Chen [22, 74] are listed in Table 4.1.

## 4.3 Modelling the surface interaction

While simulating STM images, its very important to take into account the interaction between the sample and substrate. The interaction can be van der Waals attraction, Pauli repulsion or any other complicated type including any one or both of them. The exact nature of the interaction depend on the surface and the molecule under consideration. In most cases the mathematical functions for these interactions can be derived from first principle technique i.e. by fitting the empirical function to experimental data. In our

**Table 4.1:** Tunnelling matrix elements for different tip states.

Tip State	$M$ proportional to the value at $\mathbf{r}_0$
$s$	$\psi(\mathbf{r}_0)$
$p_z$	$\frac{\partial\psi(\mathbf{r}_0)}{\partial z}$
$p_x$	$\frac{\partial\psi(\mathbf{r}_0)}{\partial x}$
$p_y$	$\frac{\partial\psi(\mathbf{r}_0)}{\partial y}$
$d_{xy}$	$\frac{\partial\psi(\mathbf{r}_0)}{\partial x \partial y}$
$d_{yx}$	$\frac{\partial\psi(\mathbf{r}_0)}{\partial y \partial z}$
$d_{zx}$	$\frac{\partial\psi(\mathbf{r}_0)}{\partial z \partial x}$
$d_{x^2-y^2}$	$\frac{\partial^2\psi(\mathbf{r}_0)}{\partial x^2} - \frac{\partial^2\psi(\mathbf{r}_0)}{\partial y^2}$
$d_{3z^2-r^2}$	$2\frac{\partial^2\psi(\mathbf{r}_0)}{\partial z^2} - \frac{\partial^2\psi(\mathbf{r}_0)}{\partial x^2} - \frac{\partial^2\psi(\mathbf{r}_0)}{\partial y^2}$

calculation we will be using Lennard-Jones potential [75, 76] to include the interaction. The mathematical form of the potential is given in (2.2) and the values of the parameters depend on the molecule under consideration and the systems with which they are associated. These values are chosen to reproduce the experimental observations.

## 4.4 Simulating AFM images using Hückel MO theory

A number of theoretical techniques were developed for modelling the multi-electron systems that are imaged in scanning probe microscopy. Most of them use density functional theory with different approximations. Since

## Theoretical basis

---

these methods are iterative, they are computationally expensive. An alternative, less expensive method is to use extended Hückel molecular orbital theory in calculating the orbital wavefunctions, as discussed in details in Section 4.1. Once the wavefunctions of the sample and the tip of a particular MO,  $\Psi_s$  and  $\Psi_t$  respectively, are calculated from EHMO theory, the force observed due to the Pauli exclusion can be calculated by fixing one of the wavefunctions and orthogonalising the other one. From the difference in kinetic energy between the orthogonalised and unorthogonalised states, a potential energy change can be calculated, which then will be used to find either the force or the frequency shift observed experimentally.

To orthogonalise  $\Psi_t$  we use Gram-Schmidt orthogonalisation assuming that the change in a particular tip MO due to the orthogonalisation does not directly alter the form of other MOs. Hence the orthogonalised wavefunction of the tip MO is given by

$$|\Psi'_t\rangle = \frac{|\Psi_t\rangle - \langle\Psi_s|\Psi_t\rangle|\Psi_s\rangle}{\sqrt{1 - |\langle\Psi_s|\Psi_t\rangle|^2}} \quad (4.32)$$

which ensures the orthogonality of  $\Psi_s$  and  $\Psi'_t$ :

$$\langle\Psi_s|\Psi'_t\rangle = 0. \quad (4.33)$$

Since the wavefunction  $\Psi_s$  remains unchanged, the increase in kinetic energy,  $\Delta E_{\text{kin}}$  is solely due to the increase in kinetic energy of the wavefunction  $\Psi_t$ . Hence

$$\Delta E_{\text{kin}} = \langle\Psi'_t|\hat{T}|\Psi'_t\rangle - \langle\Psi_t|\hat{T}|\Psi_t\rangle, \quad (4.34)$$

where  $\hat{T}$  is the kinetic energy operator. We define the following variables to

## Theoretical basis

---

simplify the notations in further calculations

$$S_{st} = \langle \Psi_s | \Psi_t \rangle \quad (4.35)$$

$$\eta_1 = \frac{1}{\sqrt{1 - |S_{st}|^2}} \quad (4.36)$$

$$\eta_2 = -\frac{S_{st}}{\sqrt{1 - |S_{st}|^2}}. \quad (4.37)$$

$\Delta E_{\text{kin}}$  can be expanded as

$$\begin{aligned} \Delta E_{\text{kin}} &= \langle \eta_1 \Psi_t + \eta_2 \Psi_s | \hat{T} | \eta_1 \Psi_t + \eta_2 \Psi_s \rangle - \langle \Psi_t | \hat{T} | \Psi_t \rangle \\ &= \eta_2^2 \langle \Psi_s | \hat{T} | \Psi_s \rangle + \eta_1 \eta_2 \left( \langle \Psi_s | \hat{T} | \Psi_t \rangle + \langle \Psi_t | \hat{T} | \Psi_s \rangle \right) \\ &\quad + (\eta_1^2 - 1) \langle \Psi_t | \hat{T} | \Psi_t \rangle. \end{aligned} \quad (4.38)$$

All the integrals can be calculated using Gaussian type orbitals (GTOs). However, at the small tip-sample separation, it is the Pauli repulsion energy also called the interaction energy,  $E_{\text{int}}$  that needs to be considered to construct an image. Moll *et al.* [77] showed that  $E_{\text{int}}$  can be approximated from the increase in kinetic energy as

$$E_{\text{int}}(x, y, z) = \frac{1}{z} \lim_{\gamma \rightarrow \infty} \int_z^\gamma \Delta E_{\text{kin}}(x, y, z') dz'. \quad (4.39)$$

Here  $(x, y, z)$  is used to show the tip position dependence while sample is placed at  $(x, y, 0)$ . In order to calculate the force experienced by the tip at the tip position  $(x, y, z)$  we take the derivative of  $\Delta E_{\text{int}}(x, y, z)$  with respect to  $z$ , which gives

$$\begin{aligned} F(x, y, z) &= -\frac{\partial}{\partial z} E_{\text{int}}(x, y, z) \\ &= \frac{1}{z^2} \lim_{\gamma \rightarrow \infty} \int_z^\gamma \Delta E_{\text{kin}}(x, y, z') dz' \\ &\quad - \frac{1}{z} \frac{\partial}{\partial z} \lim_{\gamma \rightarrow \infty} \int_z^\gamma \Delta E_{\text{kin}}(x, y, z') dz'. \end{aligned} \quad (4.40)$$

At the upper bound, as  $\gamma \rightarrow \infty$  the integral will not be a function of  $z$ , as a result the derivative will be zero. At the lower bound, the integral will be

## Theoretical basis

---

evaluated at the tip position  $z$ . Hence, the derivative with respect to  $z$  will simply return the initial function. Which leads us to

$$F(x, y, z) = \frac{1}{z^2} \lim_{\gamma \rightarrow \infty} \int_z^\gamma \Delta E_{\text{kin}}(x, y, z') dz' + \frac{1}{z} \Delta E_{\text{kin}}(x, y, z). \quad (4.41)$$

It is shown by Lakin [78] that the term containing the integral can be approximated as some multiple of the kinetic energy change i.e.

$$\frac{1}{z^2} \lim_{\gamma \rightarrow \infty} \int_z^\gamma \Delta E_{\text{kin}}(x, y, z') dz' = k \frac{1}{z} \Delta E_{\text{kin}}(x, y, z), \quad (4.42)$$

where  $k$  is a multiplicative constant. This gives us the force as

$$F(x, y, z) = \frac{1}{z} (k + 1) \Delta E_{\text{kin}}(x, y, z), \quad (4.43)$$

which directly relates the force to the change in kinetic energy. In a constant height scan,  $z$  remains the same throughout the operation leaving a simple proportionality between the force and change in kinetic energy:

$$F(x, y) \propto \Delta E_{\text{kin}}(x, y). \quad (4.44)$$

Here the force is calculated considering a particular MO of the tip interacting with a given MO of the sample. To include the full interaction, it is necessary to sum the kinetic energy change associated with each MO of the tip and the sample. Throughout the calculation it is assumed that the orthogonalisation of a particular tip MO does not make any changes directly to the other MOs and the interactions are independent of one another. Though in principle they are related to one another through the Pauli exclusion principle, we can neglect this effect as the changes in other MOs are expected to be small because of the orthogonalisation of a particular MO.

## 4.5 Mechanical AFM model with a flexible tip

Despite the advancement in experimental techniques to use a functionalized tip in AFM, different groups are also trying to develop a rather simple mechanical model to simulate AFM images [43–45]. The model we adapted is proposed by Hapala *et al.* [44], a simple model where the interaction between the functionalized tip and the sample is described by using empirical potentials. The tip is modeled as a functionalized soft apex and consists of a *tip base* and a *probe* (Figure 4.1). The tip base is the outermost atom of the metallic tip and the probe is allowed to rotate around the tip base as a flexible end of the functionalized tip.

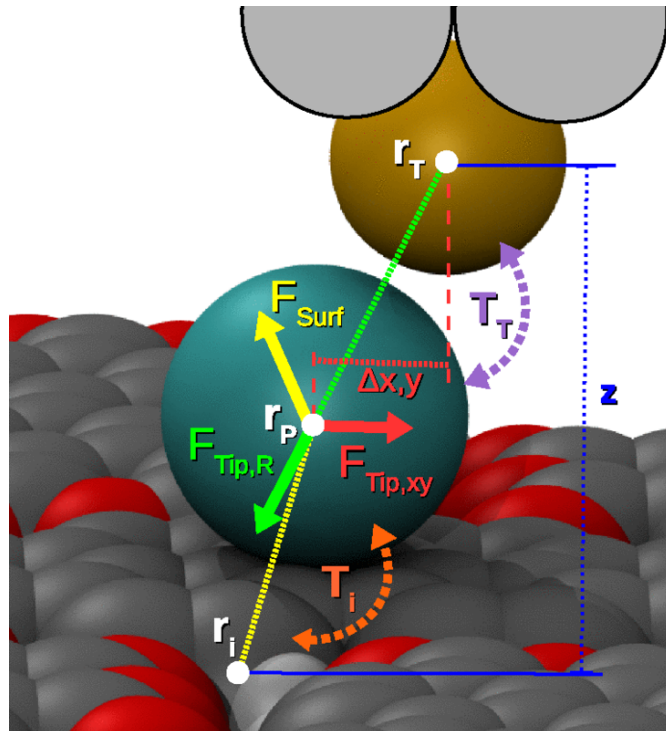


**Figure 4.1:** Schematic view of the mechanical model of a functionalized tip as employed by Hapala *et al.* [44]. The last metal atom of the tip (tip base) is shown in sand color the probe particle in cyan, and the sample in gray and red. The forces acting on the probe particle are shown in color: radial tip force  $F_{\text{Tip,R}}$  (green); lateral tip force  $F_{\text{Tip,xy}}$  (red); force  $F_{\text{Surf}}$  exerted by atoms of the sample (yellow). Figure adapted from reference [44].

## Theoretical basis

---

Depending on the functionalization of the tip, the probe can be a single atom or a molecule consisting of many atoms. In either case the interaction between the probe of the functionalized tip and the sample is described by the pairwise Lennard-Jones (L-J) potential. The single atom probe experiences three forces: (i) a L-J force due to the tip base,  $\mathbf{F}_{\text{Tip,R}}$ , (ii) a sum of all pairwise L-J forces due to interactions with the atoms in the sample,  $\mathbf{F}_{\text{Surf}}$  and (iii) a lateral harmonic force from the tip base,  $\mathbf{F}_{\text{Tip,xy}}$ . If the probe contains several atoms, each atom in the probe experiences all three forces and the net force on the probe is calculated by summing up all the forces experienced by each atom on the probe. The potential  $U_{\alpha\beta}(r)$  and the force  $\mathbf{F}_{\alpha\beta}(\mathbf{R})$  between atoms  $\alpha$  and  $\beta$  are described as

$$U_{\alpha\beta}(r) = \epsilon_{\alpha\beta} \left( \frac{r_{\alpha\beta}^{12}}{r^{12}} - \frac{2r_{\alpha\beta}^6}{r^6} \right), \quad (4.45)$$

$$\mathbf{F}_{\alpha\beta}(\mathbf{R}) = 12\epsilon_{\alpha\beta} \mathbf{R} \left( \frac{r_{\alpha\beta}^{12}}{r^{14}} - \frac{r_{\alpha\beta}^6}{r^8} \right) \quad (4.46)$$

where  $r = |\mathbf{R}|$  is the distance between atoms  $\alpha$  and  $\beta$ ,  $\epsilon_{\alpha\beta}$  is the pair binding energy and  $r_{\alpha\beta}$  is the equilibrium separation of the two atoms. The pair parameters are computed from atomic parameters  $\epsilon_{\alpha}$  and  $r_{\alpha}$  as

$$\epsilon_{\alpha\beta} = \sqrt{\epsilon_{\alpha}\epsilon_{\beta}}, \quad (4.47)$$

$$r_{\alpha\beta} = r_{\alpha} + r_{\beta}. \quad (4.48)$$

Where  $\epsilon_{\alpha}$  is the depth of the potential well and  $r_{\alpha}$  is the distance at which the potential reaches its minimum as shown in Figure 4.2 for atom  $\alpha$ . At  $r_{\alpha}$  the value of the potential is  $-\epsilon_{\alpha}$ . The values of  $\epsilon_{\alpha}$  and  $r_{\alpha}$  can be fitted to reproduce experimental results.

### 4.5.1 Simulating AFM images

In generating the simulated AFM images, first the tip is set at a particular position  $(x, y, z_0)$  far from the sample, where  $z_0$  is the perpendicular offset

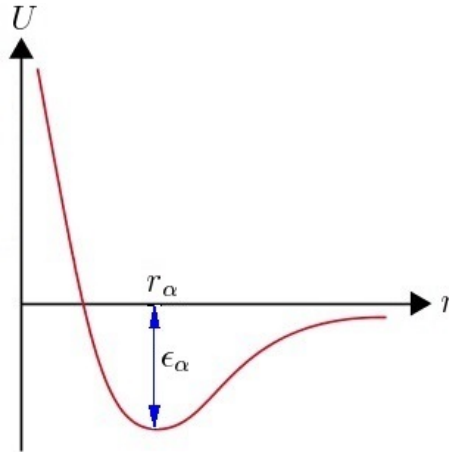


**Figure 4.2:** A graph showing the typical shape of the Lennard-Jones potential.

distance of the tip base from the sample. In this position the probe is placed in the minimum of the tip potential. The tip is approached towards the sample in small steps. At each step the net force experienced by the probe,

$$\mathbf{F}_{\text{net}} = \mathbf{F}_{\text{Tip,R}} + \mathbf{F}_{\text{Tip,xy}} + \mathbf{F}_{\text{Surf}}, \quad (4.49)$$

is minimized allowing the probe position to be relaxed. On completing the structural relaxation the vertical component of the force felt by the probe due to the sample,  $F_{\text{Surf}}(z)$ , at the relaxed probe position is recorded for that particulate tip position  $(x, y, z)$ . From those data the constant height image can be obtained for every required height  $Z$ .

## 4.6 Kohn-Sham DFT

In principle, the quantum mechanical wavefunction of a many-particle system contains all the information about the system. To derive the properties of a system of  $N$  particles from the quantum mechanical laws, it is require to solve the Schrödinger equation of  $3N$  spatial variables and  $N$  spin variables (for electrons). In reality, this can not be done exactly, without making any approximations for even a system having several electrons. However ‘solv-

## Theoretical basis

---

ing' the Schrödinger equations is only part of the many-particle problem. The most important objective is to understand and predict the properties of many-particle systems and to calculate the several measurable quantities, such as the bonding energy, polarizability, conductivity, etc., rather than the wavefunction itself. A formalism which is exact (to some extent) and can treat the system with less computational effort is the density functional method [79–83] developed by Hohenberg and Kohn [84] and Kohn and Sham [36]. The Kohn-Sham approach to density functional theory (DFT) allows an exact description of the interacting many-particle systems in terms of an effective self-consistent non-interacting particle system. The effective potential in this noninteracting Kohn-Sham system can be shown to be completely determined by the electron density of the interacting system, and is for this reason called a density functional. The total energy functional of the Kohn-Sham system in a static external potential  $v(\mathbf{r})$  is given in terms of the electron density  $n(\mathbf{r})$  as

$$E[n] = \int v(\mathbf{r})n(\mathbf{r})d\mathbf{r} + \frac{e^2}{2} \int \int \frac{n(\mathbf{r})n(\mathbf{r}')}{|\mathbf{r} - \mathbf{r}'|} d\mathbf{r}d\mathbf{r}' + T_s[n] + E_{xc}[n], \quad (4.50)$$

where the second term on the right side of the equation represents the classical Coulomb interaction energy for the electron density with itself (also known as the Hartree energy),  $T_s[n]$  is the kinetic energy functional of a system of non-interacting electrons with density  $n(\mathbf{r})$  and  $E_{xc}[n]$  is the exchange-correlation energy functional of the interacting system with density  $n(\mathbf{r})$ .  $E_{xc}[n]$  accounts all the many-body effects of the electron-electron interactions and by definition it is the difference between the exact total energy and the other known quantities. However, the exact form of the exchange-correlation energy functional is not known.

Kohn-Sham DFT gives a set of Schrödinger like variational equations that are solved self consistently:

$$\hat{H}_{\text{KS}}\psi_i(\mathbf{r}) = \varepsilon_i\psi_i(\mathbf{r}), \quad (4.51)$$

## Theoretical basis

---

for the Kohn-Sham orbitals  $\psi_i(\mathbf{r})$  of the independent particle governed by an effective Hamiltonian  $\hat{H}_{\text{KS}}$  with eigenvalues  $\varepsilon_i$ . These orbitals are related to the electron density of  $N$  electrons by

$$n(\mathbf{r}) = \sum_i^N |\psi_i(\mathbf{r})|^2. \quad (4.52)$$

The effective Hamiltonian is given by

$$\begin{aligned} H_{\text{KS}} &= -\frac{\hbar}{2m} \nabla^2 + v(\mathbf{r}) + v_{\text{H}}(\mathbf{r}) + v_{\text{xc}}(\mathbf{r}) \\ &= -\frac{\hbar}{2m} \nabla^2 + v_{\text{KS}}(\mathbf{r}), \end{aligned} \quad (4.53)$$

where  $v_{\text{KS}}(\mathbf{r})$  is the effective Kohn-Sham potential and is the sum of external, Hartree and exchange-correlation potentials. Hence the set of wave functions  $\psi_i(\mathbf{r})$  of the Kohn-Sham system that minimize the Kohn-Sham energy functional are given by the self-consistent solution of the Kohn-Sham equations:

$$\left[ -\frac{\hbar}{2m} \nabla^2 + v(\mathbf{r}) + v_{\text{H}}(\mathbf{r}) + v_{\text{xc}}(\mathbf{r}) \right] \psi_i(\mathbf{r}) = \varepsilon_i \psi_i(\mathbf{r}), \quad (4.54)$$

where

$$v_{\text{H}}(\mathbf{r}) = e^2 \int \frac{n(\mathbf{r}')}{|\mathbf{r} - \mathbf{r}'|} d\mathbf{r}' \quad (4.55)$$

and

$$v_{\text{xc}}(\mathbf{r}) = \frac{\partial E_{\text{xc}}[n(\mathbf{r})]}{\partial n(\mathbf{r})}. \quad (4.56)$$

The Kohn-Sham equations represent a mapping of the interacting many-electron system onto a system of noninteracting electrons moving in an effective potential due to all the other electrons. The Kohn-Sham equations (Eq. (4.54)) are solved self-consistently so that the occupied electronic states generate a charge density that produces the electronic potential that was

## Theoretical basis

---

used to construct the equations. If the initial and new densities are identical, then the ground state density has been found. Otherwise one should select a new trial density through minimisation of the total energy and continue to repeat the iterative procedure. In practice, such a self consistent calculation must be performed computationally. In our study we have used the open source CP2K/Quickstep code [85–87] to do the self consistent calculation. The code is used to optimize the geometry of the system under study.

# Intermolecular artifacts in AFM images of C<sub>60</sub> lattices

---

This chapter provides a detailed account of the study of two dimensional arrays of C<sub>60</sub> molecules and of isolated fullerene molecules. We also show a comparison between our theoretical results and the experimental data obtained by the experimental group of Prof Philip Moriarty, the University of Nottingham. We begin the chapter mentioning some of the reasons of studying fullerene molecule followed by the details of the NC-AFM experiment of C<sub>60</sub> monolayer and the results. In the following sections we discuss our theoretical results on the assembly of C<sub>60</sub> and how it provides a better understanding on the origin of the sharp bond like features between two molecules in the assembly. Finally we present the study of isolated C<sub>60</sub> molecule with a functionalized C<sub>60</sub> probe. Many of results that are presented in this chapter have been published in the Rapid Communication section of Physical Review B **92**, 241405(R) (2015) [88] and in Nature Communications **7**, 10621 (2016) [89].

## 5.1 Buckminsterfullerene, $C_{60}$

Buckminsterfullerene,  $C_{60}$ , known as fullerene and discovered by Kroto *et al.* in 1985 [90], is made from sixty carbon atoms in which each atom is bonded to three other carbon atoms. It has twenty hexagonal and twelve pentagon faces, where bond length of 6-6 (between two hexagons) and 5-6 (between a pentagon and hexagon) are 1.38 Å and 1.45 Å respectively. The distance from the centre of the molecule to the carbon shell is 3.555 Å.  $C_{60}$  has the highest point group symmetry possible for a molecule, icosahedral,  $I_h$ . This high symmetry of  $C_{60}$  makes it an ideal candidate for investigating symmetry lowering interactions such as Jahn-Teller effects. In addition to the potential as a single molecule transistor [91],  $C_{60}$  has many potential applications in molecular electronics such as  $C_{60}$  electrodes [92] and  $C_{60}$  junctions [93]. The monolayer formed by  $C_{60}$  molecules on different surfaces has triangular structure with a nearest neighbour separation of  $\sim 10$  Å (Figure 5.1). The interactions between molecules in  $C_{60}$  islands is dominated by van der Waals [94].

## 5.2 Why $C_{60}$

As discussed in Chapter 3 it has been shown recently that NC-AFM and scanning tunnelling hydrogen microscopy can be used to resolve apparent intermolecular features in molecular assemblies, stabilised either through hydrogen bonds [44,45,58] or, very recently, halogen-bonding interactions [95]. A theoretical study of tip-sample interaction using density functional theory (DFT) provided reasonable agreement for the relative line profile heights of the observed intra- and intermolecular features, but it failed to reproduce the striking appearance observed in experiment [59]. It has been shown that the tip-flexibility at very close tip-sample separation is responsible for apparent intra- and intermolecular features which can also be observed with

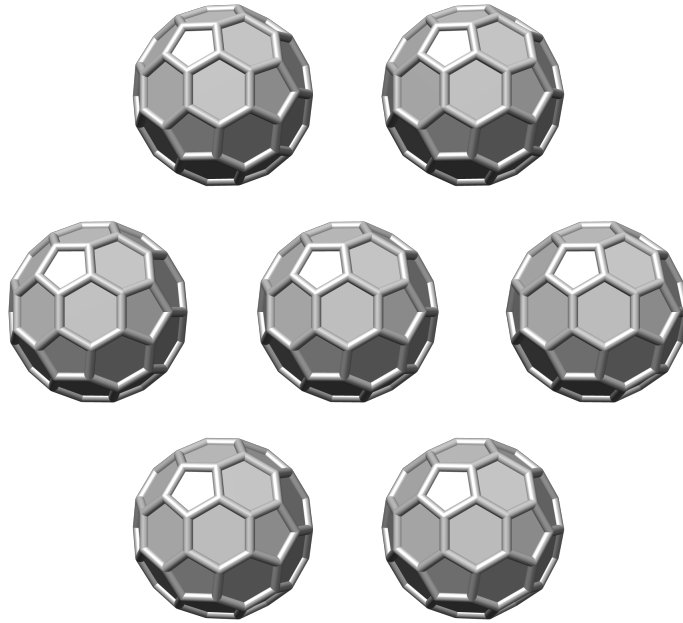


**Figure 5.1:** Assembly of  $C_{60}$  molecules as found in  $C_{60}$  island. Each molecules drawn here with hexagon-up as seen from above the  $xy$  plane.

NC-AFM even when no bonding interaction is present [45], which has led to a controversy in interpreting these kind of features. Hydrogen bonding may have a contribution to these bond-like features seen in the systems (e.g. assemblies of PTCDA, NTCDI) where hydrogen bonds are present. However the report presented in [45] suggests that the features can not originate solely from hydrogen bonds but are an artefact and can not be interpreted as a real-space image of an intermolecular bond.

We investigate the assembly of  $C_{60}$ , a system that definitively has no hydrogen bonding, to clarify the controversy. In each of the reported cases where intermolecular resolution has thus far been observed, the molecules under study have all been planar in structure. The assemblies are also generally stabilised through hydrogen bonding interactions with the interatomic separations below the sum of the van der Waals (vdW) radii. We studied two dimensional assemblies of  $C_{60}$  molecules that are neither planar in structure, nor stabilised through any other intermolecular bonding mechanism beyond vdW forces. Our study on the assembly of fullerene molecules using a simple approach based around pairwise Lennard-Jones (12-6) potentials

reproduced the experimental images, giving us insight into the origin of sharp bond like features between the molecules.

### 5.3 NC-AFM study of $C_{60}$ monolayer

In Figure 5.2 (A) and (B) we show NC-AFM frequency shift images of islands of  $H_2O@C_{60}$  ( $C_{60}$  molecules with water molecule inside the  $C_{60}$ ) deposited on Cu(111) surface using thermal sublimation, and  $C_{60}$  on a  $C_{60}$ -terminated Si(111) surface (i.e. the substrate is a monolayer of  $C_{60}$  chemisorbed on Si(111), on which there are physisorbed  $C_{60}$  islands) respectively, recorded in the constant height mode at small tip-sample separation. At these distances, repulsive contributions to the tip-sample force dominate the observed contrast, resulting in the fullerene molecules appearing brighter relative to the vdW background. The  $C_{60}$  molecules in these images are in a hexagonal arrangement with a nearest neighbour separation of  $\sim 10$  Å. Despite this large separation, clear interconnecting features are observed between nearest neighbour molecules. This is highlighted in the schematic shown in Figure 5.2 (D) and the line profile measurement in Figure 5.2 (C). Similar contrast in both the images of empty and filled  $C_{60}$  cages suggests that observations of interconnecting features are general across fullerene molecules.

### 5.4 Modelling NC-AFM images of $C_{60}$ assembly

We simulated constant height NC-AFM images of  $C_{60}$  islands using the simple mechanical model based on the Lennard-Jones potential which was described in Section 4.5. Three different tip terminations were used, namely a flexible CO tip, and both a rigid and flexible  $C_{60}$ -terminated tip. In NC-

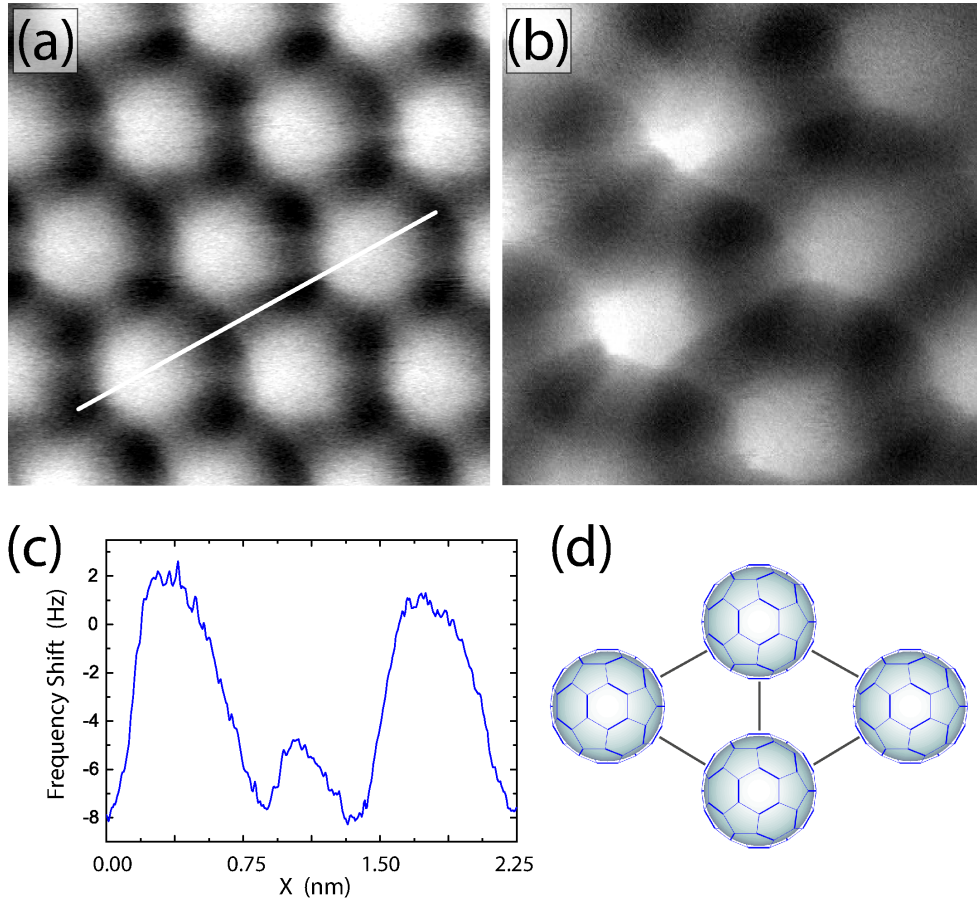


**Figure 5.2:** NC-AFM frequency shift images of a 2D assembly of (A) a thick (six-layer) film of  $H_2O@C_{60}$  and (B)  $C_{60}$  molecules recorded in the constant height mode, revealing interconnecting features between nearest neighbour molecules. Sizes of the images (A) and (B) are  $32 \text{ \AA} \times 32 \text{ \AA}$  and  $23 \text{ \AA} \times 23 \text{ \AA}$  respectively. (C) Line profile measurement along the white line shown in (A). (D) Schematic of the  $C_{60}$  packing arrangement and locations of apparent intermolecular features.

AFM imaging and to simulate those images, a flexible CO-terminated tip is commonly used [43–46], which is small enough in size to penetrate deep into hollow positions and voids between atoms of the sample, giving rise to a sharp resolution in the images [44]. We studied the system with a  $C_{60}$ -terminated tip as a  $C_{60}$  is likely to be picked up during AFM experiments.

The probe in our model is represented by a single spherical atom, an oxygen atom of  $r_\alpha = 1.661 \text{ \AA}$  in the case of a CO-terminated tip. For a  $C_{60}$ -functionalized tip, we take the  $C_{60}$  molecule to act in the same way as a single effective probe particle, similar to the CO tip. The L-J parameters

## Intermolecular artifacts in AFM images of $C_{60}$ lattices

---

that were used in the simulation of NC-AFM images are given in Table 5.1. For C, O and the tip base (with a CO probe) we used the same parameters as used in [44], however for the  $C_{60}$  probe i.e. for the  $C_{60}$ -functionalized tip, we made an adjustment of the parameters for both the tip base and the probe. Since  $C_{60}$  is a molecule with a vdW diameter of  $10.0 \text{ \AA}$ , we used  $r_\alpha = 5.00 \text{ \AA}$  for the  $C_{60}$ -functionalized probe. It is also logical to change the tip base radius accordingly to give the probe particle more freedom while rotating around the tip base during the relaxation of the force acting on the probe. For the tip base (with a  $C_{60}$  probe) we used  $r_\alpha = 5.00 \text{ \AA}$  (as compared to the radius of  $2.00 \text{ \AA}$  used for a CO probe). For the probe particle, we kept the same value for  $\epsilon_\alpha$  that was used for a CO-functionalized tip. However, for the tip base we used a much larger value of  $\epsilon_\alpha = 15000 \text{ meV}$ , compared to  $1000 \text{ meV}$  for CO, which we found to be the most appropriate in order to keep the probe particle bonded with the tip base without losing its flexibility in the  $z$ -direction. For the lateral harmonic force we used a lateral stiffness  $k_{xy} = 0.5 \text{ Nm}^{-1}$  for both types of probe particles as in [44]. A larger value of  $k_{xy}$  makes the tip more rigid while a smaller value provides more flexibility on the tip.

**Table 5.1:** Lennard-Jones parameters.

Atom/Particle	$\epsilon_\alpha$ (meV)	$r_\alpha$ ( $\text{\AA}$ )
C	3.729	1.908
O	9.106	1.661
$C_{60}$ (as a probe)	9.106	5.000
Tip base (for CO probe)	1000	2.000
Tip base (for $C_{60}$ probe)	15000	5.000

The “sample” we have used in our simulation consists of seven hexagon-up oriented  $C_{60}$  molecules with an intermolecular distance of  $10.2 \text{ \AA}$ , without periodic boundary conditions. We acquired the simulation data by scanning the sample laterally with a step of  $\Delta x, \Delta y = 0.2 \text{ \AA}$ . With the  $C_{60}$  tip

## Intermolecular artifacts in AFM images of $C_{60}$ lattices

---

at each lateral position  $(x, y)$  we placed the tip base at  $z_0 = 25 \text{ \AA}$  and approached the sample in steps of  $\Delta z = 0.1 \text{ \AA}$  until  $z = 17.5 \text{ \AA}$ , allowing the probe particle position to be relaxed at each step in the combined force,  $\mathbf{F}_{\text{net}}$  (Eq. (4.49)) of the sample and tip base. The vertical component,  $F_{\text{Surf}}(z)$ , (calculated using Eq. (4.46)) of the force experienced by the probe due to the atoms in the sample at the relaxed position is recorded for that particular tip position  $(x, y, z)$ , from which constant height tip-sample force images are generated for that particular tip height,  $z$ . We followed the same procedure with a CO-terminated tip starting at  $z_0 = 16.5 \text{ \AA}$  and approached the sample until  $z = 9 \text{ \AA}$ . Since the tip-sample separation,  $z$  is related to the sizes of the tip base and of the probe particle, we normalized each set of images relative to the  $F_{\text{Surf}}(z)$  minima above the central  $C_{60}$ .

Simulated images of the tip-sample force,  $F_{\text{Surf}}(z)$  are shown in Figure 5.3 at different tip-sample separations  $z$ . The flexible CO-functionalized tip and rigid  $C_{60}$ -terminated tip clearly fail to reproduce the intermolecular feature even at very small tip-sample separation, however the flexible CO-tip model clearly resolves the internal atomic structure of each  $C_{60}$  molecule within the island, revealing the hexagonal face at  $Z = -50 \text{ pm}$  (relative to the  $F_{\text{Surf}}(z)$  turn-around). Only when the large radius probe is allowed to relax do clear interconnecting features, akin to those observed in experiment, appear in the simulations. Just as was found in the experiment (Figure 5.2) the interconnecting intermolecular features become visible in the simulations at tip-sample distances below  $Z = -200 \text{ pm}$  (relative to the  $F_{\text{Surf}}(z)$  turn-around), past the point at which repulsion is observed within the individual molecules. The fixed  $C_{60}$ -tip simulation does not reveal the interconnecting features, even at very small tip-sample separations. This is surprising, as one of the important effects of the flexible tip model is usually to ‘normalise’ the intra- and intermolecular contributions to the image such that they appear with similar brightness. For instance, over a  $C_{60}$  molecule, at a tip height of  $Z = -200 \text{ pm}$  the fixed  $C_{60}$ -tip simulation reveals forces over an order of magnitude greater than the flexible tip simulation. This confirms that it is

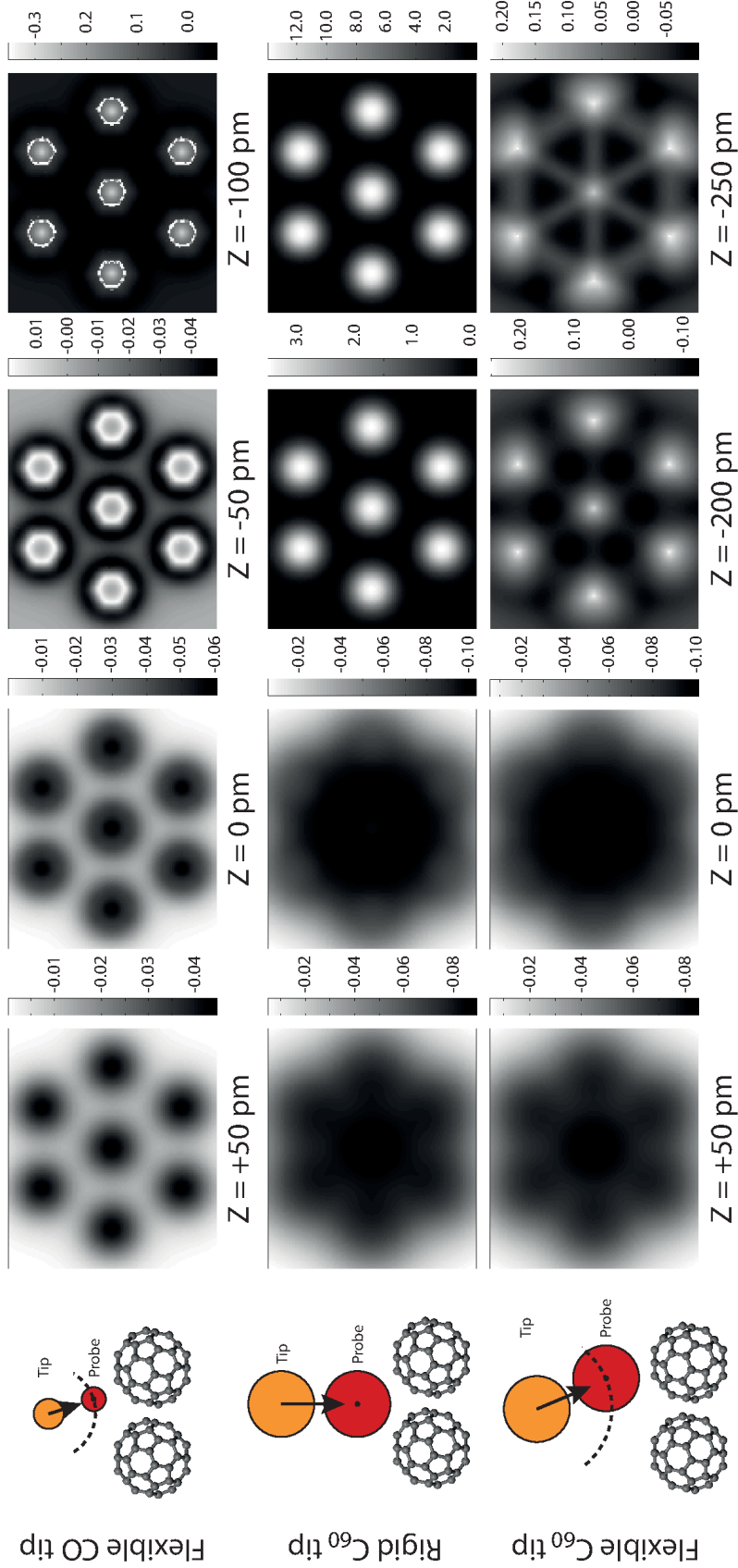


**Figure 5.3:** Simulated NC-AFM images using a flexible Lennard-Jones tip model. Using a flexible CO probe particle (of radius 1.661 Å) at decreasing tip-sample separation (top). At  $Z = -50$  pm the hexagonal faces of the molecules can clearly be observed. Simulated force images of the same island with  $C_{60}$ -terminated tip (a probe particle of radius 5.0 Å) are also shown either with a fixed tip (middle) or allowed to relax (bottom). Whilst internal features can no longer be resolved due to the large probe radius, clear interconnecting features can be seen for the flexible  $C_{60}$  tip model. Smaller tip-sample  $Z$  heights are shown for the large tip and probe radii due to different choice of Lennard-Jones parameters. The colour scale shown in nN for all images.

## Intermolecular artifacts in AFM images of $C_{60}$ lattices

only with the combination of both a large radius  $C_{60}$ -tip, and the flexible junction (which can be attributed to the weakly bound nature of a single  $C_{60}$  at the apex of a molecular tip-cluster), that the interconnecting features can be observed.

We show more simulated images of the assembly of  $C_{60}$  in Figure 5.4 for different tip-sample separations,  $Z$  to visualize how intermolecular features become more and more apparent with the decrease of tip-sample separation. At the beginning, the central  $C_{60}$  molecule of the sample appears like a large spherical ball (at  $Z = -150$  pm, Figure 5.4 a) while the shape of the surrounding molecules are slightly distorted because of broken symmetry. The spacing between the molecules in the sample becomes more visible as the tip approaches the assembly. Also with the decrease of tip-sample separation the brightness of the molecules as well as that of the bond-like feature increases (at  $Z = -240$  pm, Figure 5.4 d).

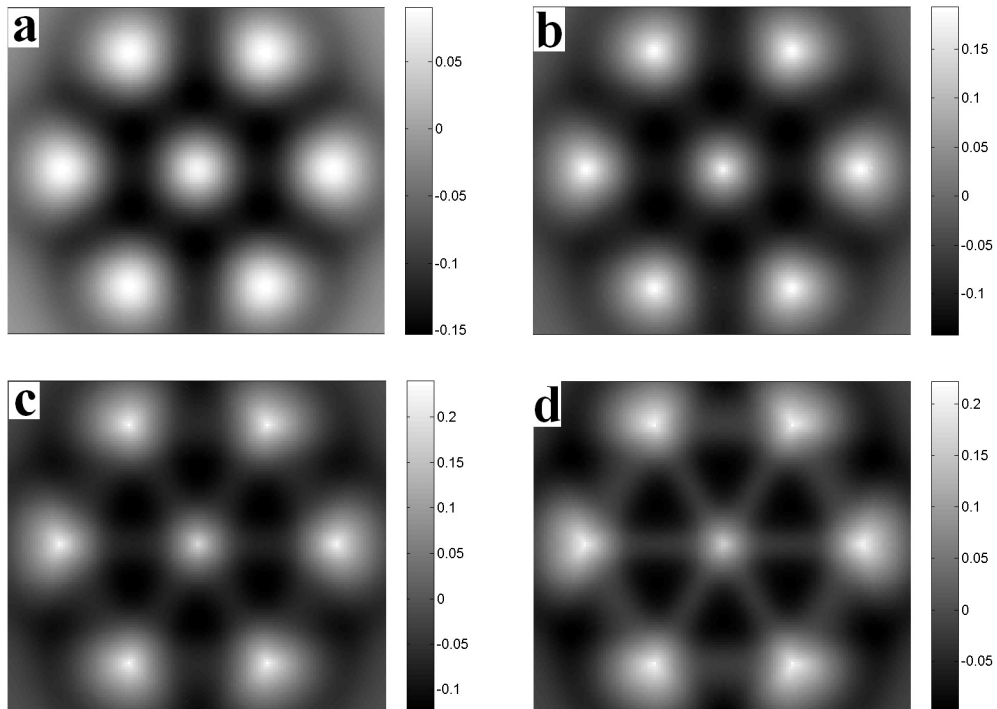


**Figure 5.4:** Simulated NC-AFM images with flexible  $C_{60}$ -functionalized tip for four different tip height: a) at  $Z = -150$  pm, b) at  $Z = -180$  pm, c) at  $Z = -210$  pm and d) at  $Z = -240$  pm. The sample contain 7  $C_{60}$  molecules with **hexagon up** and the colour scale shown in nN.

### 5.4.1 Variation in force experienced by the probe particle

To investigate the variation in the force experienced by the tip as it becomes closer to the  $C_{60}$  lattice, we plot the forces against the tip-sample separation,  $Z$  for five different points over the sample which are shown in Figure 5.5. The value  $Z = 0$  corresponds to the minimum of  $F_{\text{surf}}(z)$  when its plotted over the centre of the central molecule in the sample. The blue curve in the Figure 5.5 (bottom) shows this plot. From the force curves we observe that at large tip-sample separation the force experienced by the tip from the sample is almost same irrespective of the topology of the sample. As the tip approaches to the sample this starts to vary and the differences of the forces experienced by the tip become clear. The force experienced by tip is most when the tip is just over a molecule and it is least if the tip is placed over an empty space between the molecules, which of course is expected. The bending of the blue curve in Figure 5.5 (bottom) after  $Z = -1.9 \text{ \AA}$  originates from the fact that the force experienced by the probe when it approaches the sample over the centre of the central molecule is far greater than the force experienced by the probe when it approaches the sample over a hollow place in the sample, magenta curve (as in the Figure 5.5). As a result the probe bends largely (which are shown in Figure 5.6 and Figure 5.7) to minimize the force felt by it from sample. Physically this could also mean the bending of the functionalized STM tip or a deformation of the tip or the sample or both because of the large tip-sample force at small tip-sample separation.

The trajectory of the  $C_{60}$  probe particle as it approaches the  $C_{60}$  island above three key features of the image is shown in Figure 5.6 and Figure 5.7 to visualize the displacement of the probe particle during the simulation. We observe from the probe trajectories that the probe bends most when it is over a  $C_{60}$  molecule of the sample and least in a void space.

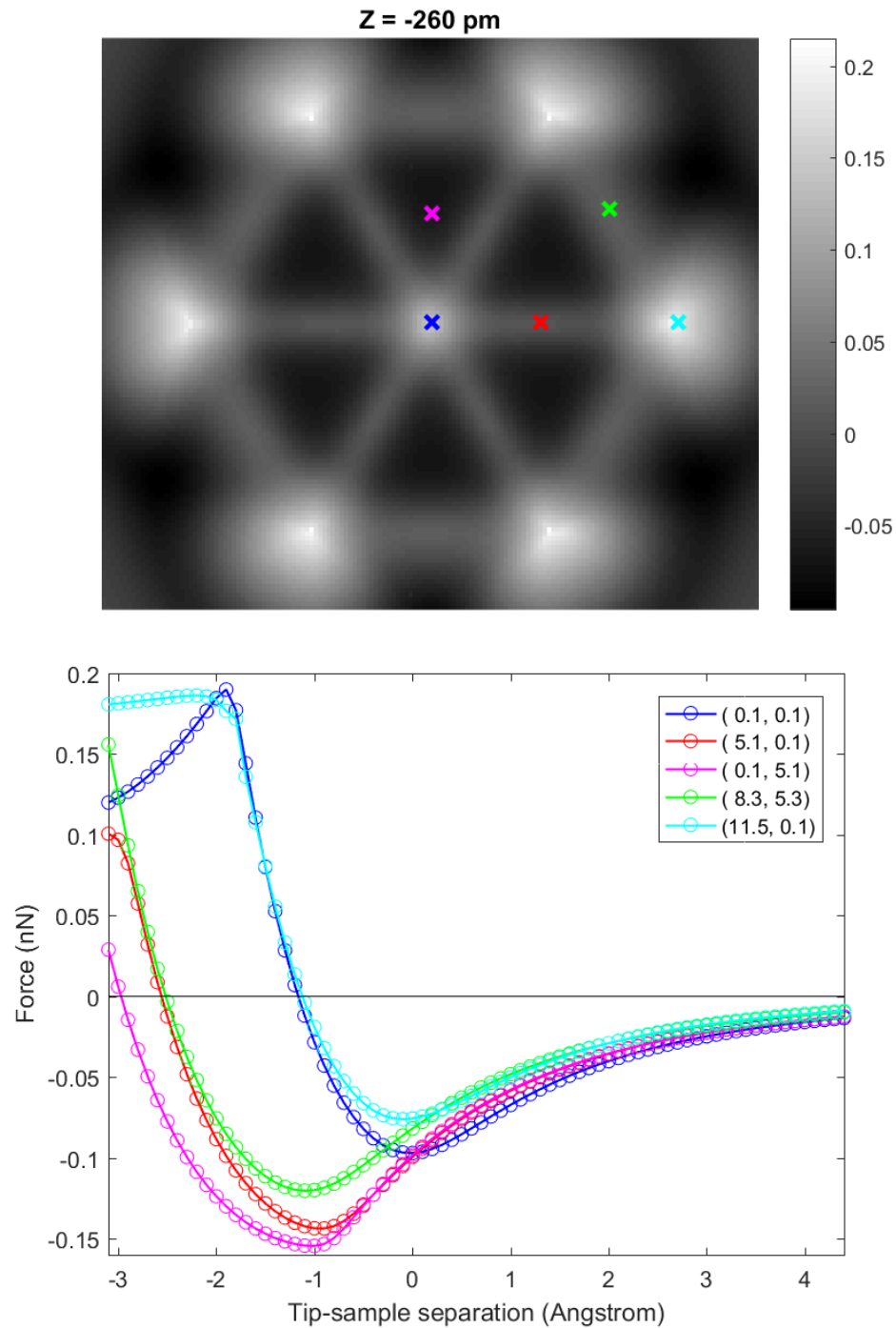


**Figure 5.5:** Variation in force curve over different positions of the assembly of  $C_{60}$  as the tip approaches the sample. The top image shows marks over different locations of  $C_{60}$  islands at which the forces are plotted which are shown at the bottom image. Legend marks on the force plots represents  $(X, Y)$  values at which the forces are plotted.

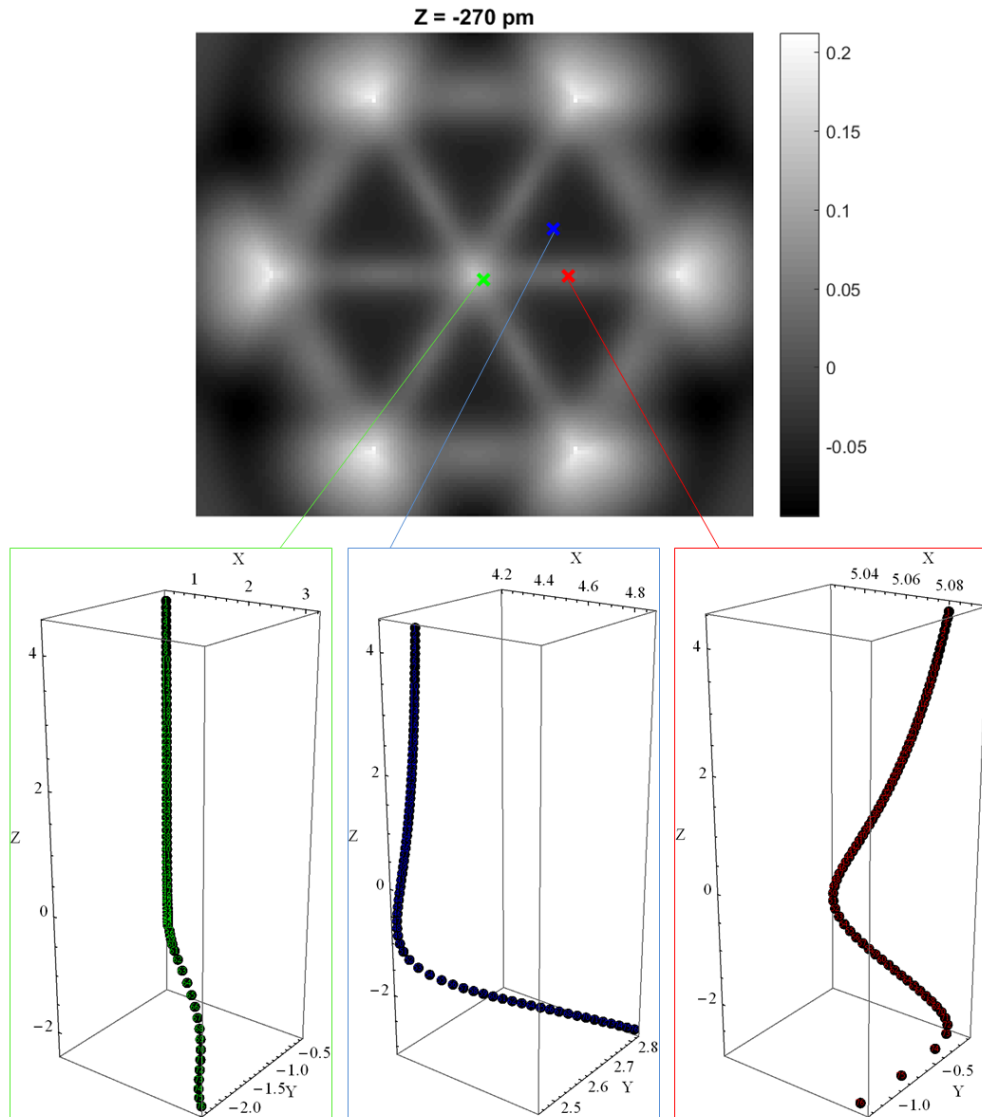


**Figure 5.6:** Probe trajectory from the simulated images using  $C_{60}$ -functionalized probe at three different position on the sample as the tip base approaches to the sample: above a  $C_{60}$  molecule (green), in the void between molecules (blue), and above an intermolecular artefact (red) using a “zoomed X-Y scale” to highlight features in the tip-displacement plots.  $Z$  corresponds to the probe particle position normalised to the force turnaround located in the centre of a  $C_{60}$  molecule (Figure 5.5).

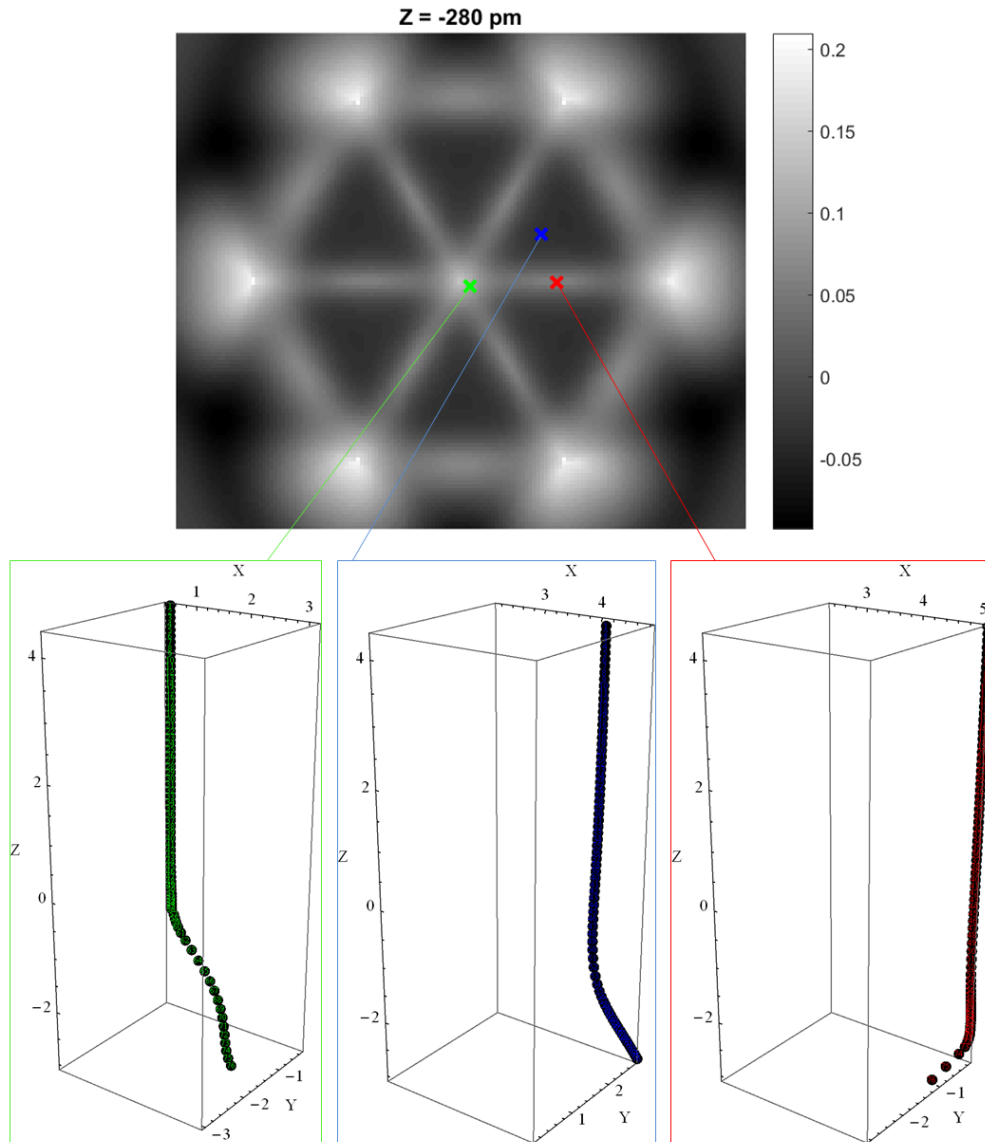


**Figure 5.7:**  $C_{60}$ -functionalized probe trajectories, which shown in Figure 5.6, are plotted using a “constant  $X$ - $Y$  scale”. These fixed scale plot provide a better understanding on the deviation of the probe particle at different positions on the sample. The probe deflects most when the tip is at the top of a  $C_{60}$  molecule. The simulated constant height force image is also at different tip-sample separation,  $Z = -280$  pm.

### 5.4.2 Effect of stiffness parameter in the contrast of the simulated AFM images

To understand the effect of the variation of lateral stiffness  $k_{xy}$  of the interaction between the tip base and the functionalized probe particle, we also simulated AFM images of the assembly of C<sub>60</sub> with different  $k_{xy}$  values other than  $0.5 \text{ Nm}^{-1}$ , which are shown in Figure 5.8, Figure 5.9, and Figure 5.10. Each of the other parameters used in producing these images was kept the same as the values used for Figure 5.4. A smaller value of  $k_{xy}$  means a softer probe, which can easily move around the tip base, while the flexibility of the probe particle decreases with increasing  $k_{xy}$ . This means that the value of lateral stiffness  $k_{xy}$  is a measure of the rigidity of the functionalized probe particle. From these images we observe that the appearance and the sharpness of the bond like features between the C<sub>60</sub> molecules in the assembly greatly depends on the choice of  $k_{xy}$  during simulation. With a smaller value of  $k_{xy}$  i.e. with a soft probe, we can observe the very sharp bond like features between the C<sub>60</sub> molecules in the island even when there is a considerable amount of separation between the tip and the sample (Figure 5.8). While with a higher  $k_{xy}$  value we only observe the bond like feature when the tip is very close to the sample (images in Figure 5.10 with  $k_{xy} = 1 \text{ Nm}^{-1}$ ). When we use a very high  $k_{xy}$  value, e.g.  $10 \text{ Nm}^{-1}$  or more we hardly observe any intermolecular contrast between the molecules even if the tip is brought very close to the sample (Figure 5.10). Please note that the value of  $Z$  corresponds to the probe particle position normalised to the force turnaround located in the centre of the central C<sub>60</sub> molecule with  $k_{xy} = 0.5 \text{ Nm}^{-1}$  (Figure 5.5).

From Figure 5.9 we note that increasing the lateral stiffness shifts particular types of high resolution contrasts towards smaller tip-sample separations, e.g. compare  $k_{xy} = 0.3 \text{ Nm}^{-1}$  at  $Z = -210 \text{ pm}$  with  $k_{xy} = 0.7 \text{ Nm}^{-1}$  at  $Z = -240 \text{ pm}$ . At the same time dark features around the central C<sub>60</sub> molecule in the sample are observed with very soft tip at close tip-sample

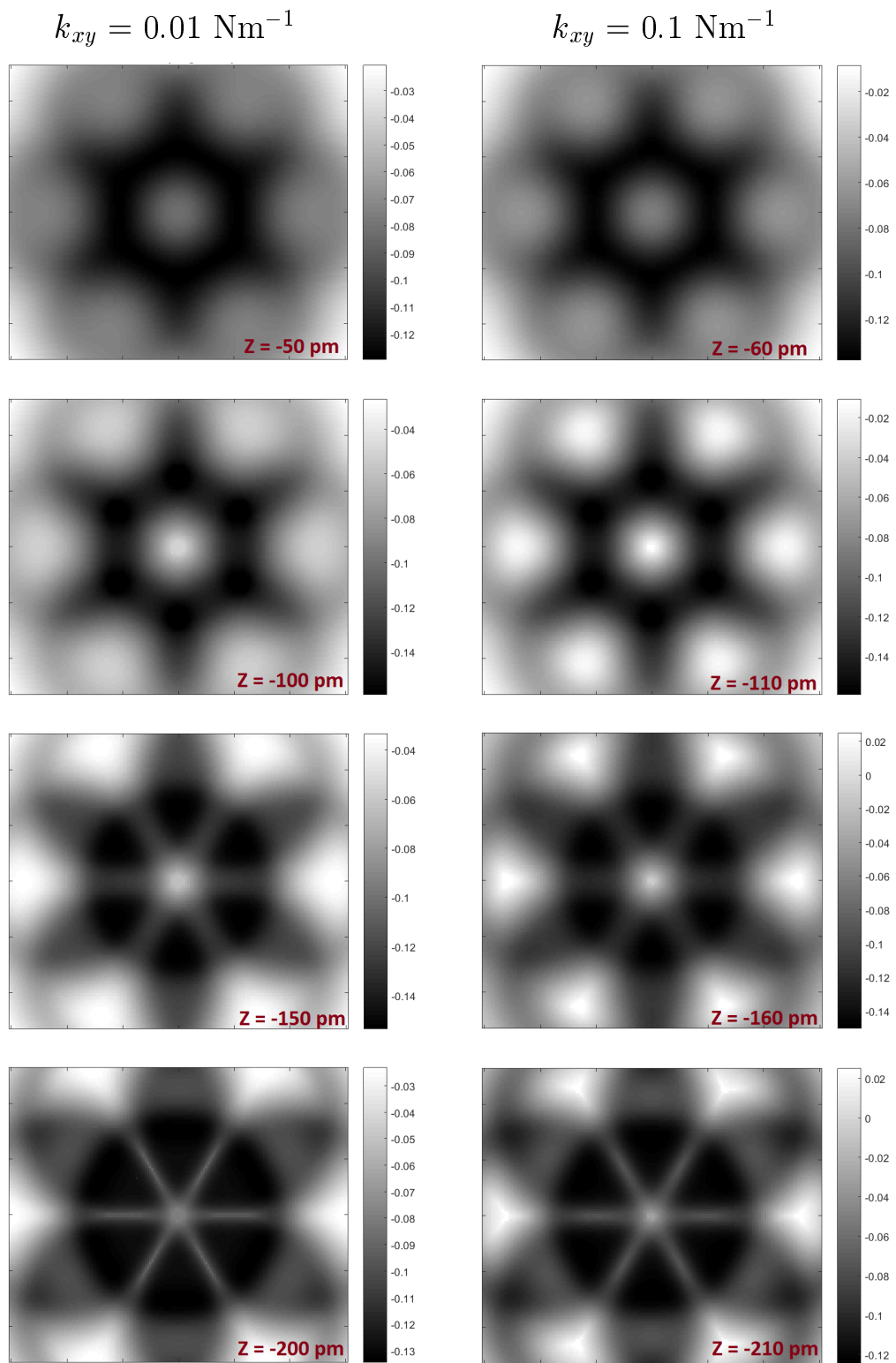


**Figure 5.8:** Constant height force images of a  $C_{60}$  island obtained with two different values of lateral stiffness  $k_{xy}$  of the interaction between tip base and the functionalized probe particle. Tip-sample distances are quoted on the images. The colour scale shown in nN for all images.

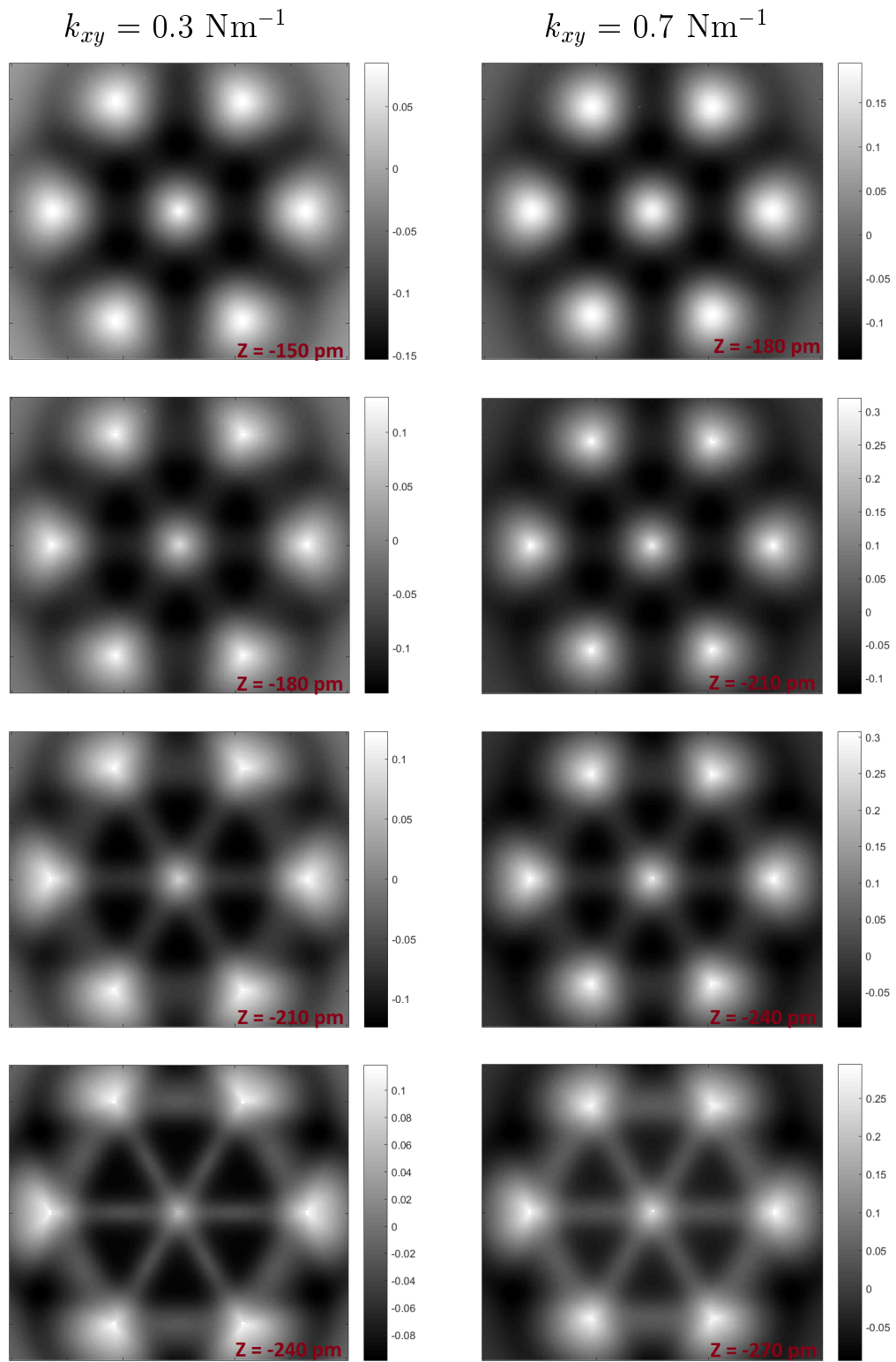


**Figure 5.9:** Constant height force images of a  $C_{60}$  island as shown in Figure 5.8 but for different values of lateral stiffness  $k_{xy}$  and tip-sample separation  $Z$ .

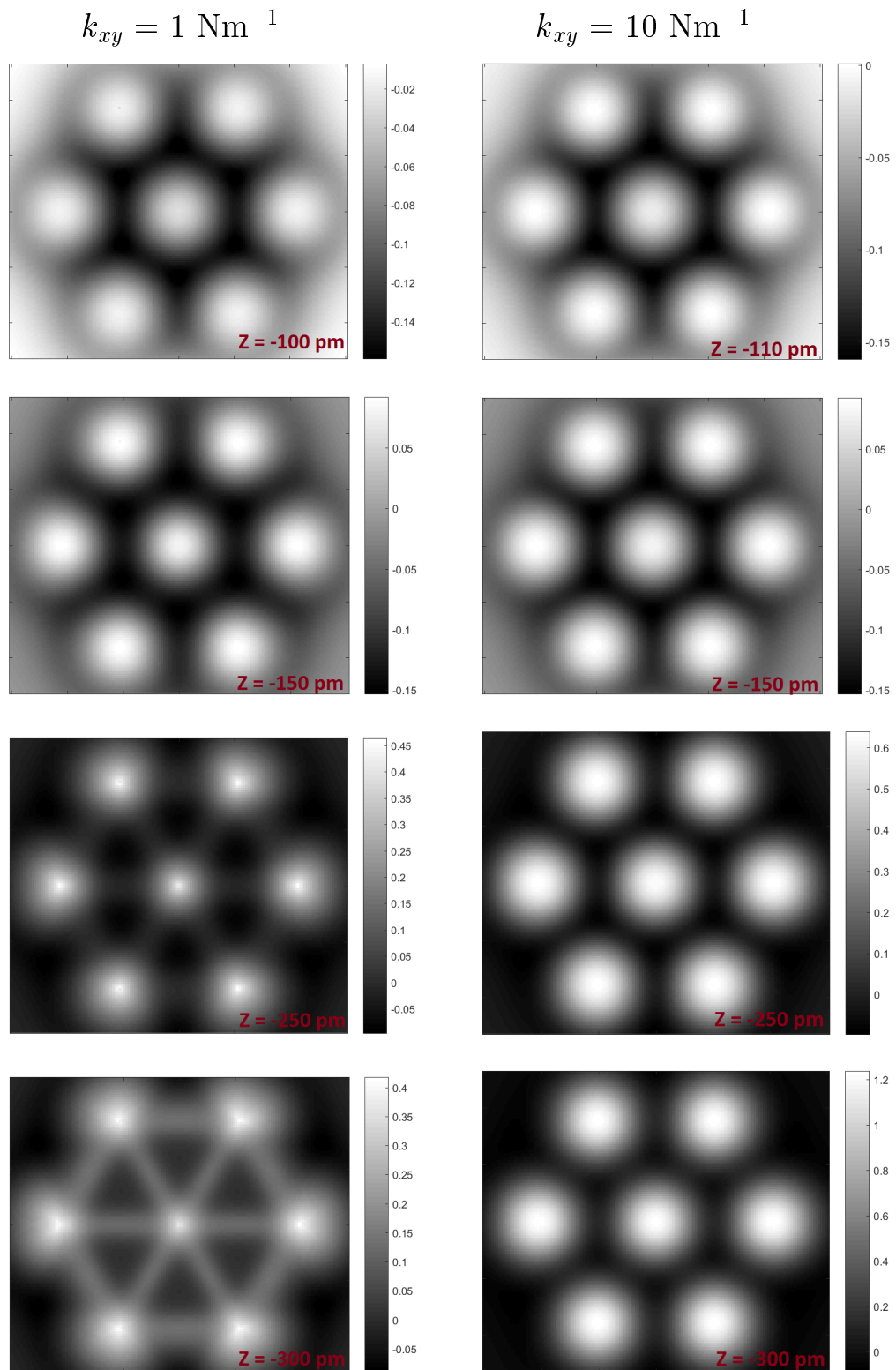


**Figure 5.10:** Constant height force images of a  $C_{60}$  island as shown in Figure 5.8 and 5.9 but for different values of lateral stiffness  $k_{xy}$  and tip-sample separation  $Z$ .

proximity. This originates from the strong repulsion force experienced by the probe as it approaches the sample. As a result, the functionalized probe particle is forced to jump out of the local minimum to some other of the neighbouring local minima. This kind of behaviour of the functionalized probe is also reported in the supplementary information of reference [44]. However the nature of this kind of jump of the probe particle cannot be described correctly with the current model and the feature is not observed for surrounding molecules because of broken symmetry.

### 5.4.3 The role of molecular orientation and symmetry

In Figure 5.11, we show simulated NC-AFM images of a  $C_{60}$  assembly where the orientation of  $C_{60}$  molecules is not hexagon up. In the first row of images, all the molecules are oriented with pentagon up while in the second row all the  $C_{60}$ s are with double bond up. Comparing these images with the images in Figure 5.4 we do not notice any significant differences in the bond-like features that are observed between the molecules. In all these sets of images we observe the same intermolecular features irrespective of the orientation of  $C_{60}$  in the sample. However, the force experienced by the tip varies slightly due to the orientation of  $C_{60}$ . This originates from the fact that there is a little change in the height of  $C_{60}$  due to its orientation, though the centre to centre tip-sample separation remain same.

To understand the effect of the symmetry on a  $C_{60}$  molecule in the island, we did the simulation with a sample having 19  $C_{60}$  molecules using the flexible  $C_{60}$ -functionalized tip (Figure 5.12). The effects of this symmetry-breaking on the images can be manifested in two ways. First, the thickness of the intermolecular “bonds” is different between molecules at the edge of the cluster as compared to the features connecting the inner molecules to its neighbours. And, second, the shapes of the molecules themselves differ. Each molecules at the edge of the cluster has a triangular shape, as compared to the much more circularly-symmetric appearance of inner

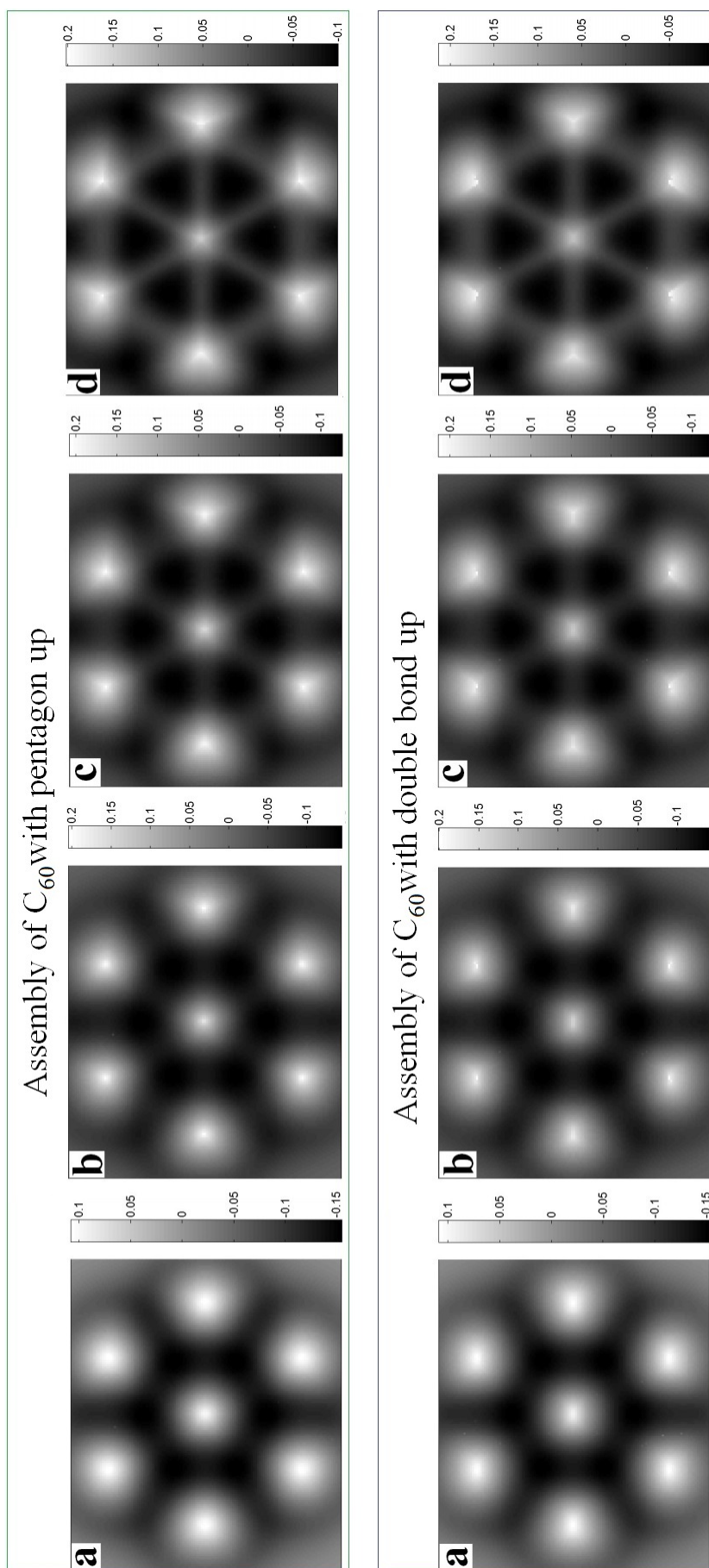


**Figure 5.11:** Simulated NC-AFM images with flexible  $C_{60}$ -functionalized tip for four different tip heights. The sample contain 7  $C_{60}$  molecules with pentagon up (top row) and double bond up (bottom row). The levels a, b, c and d on the images correspond to different values of tip-sample separation  $Z$ , namely -150 pm, -180 pm, -210 pm and -240 pm respectively and the colour scale shown in nN.

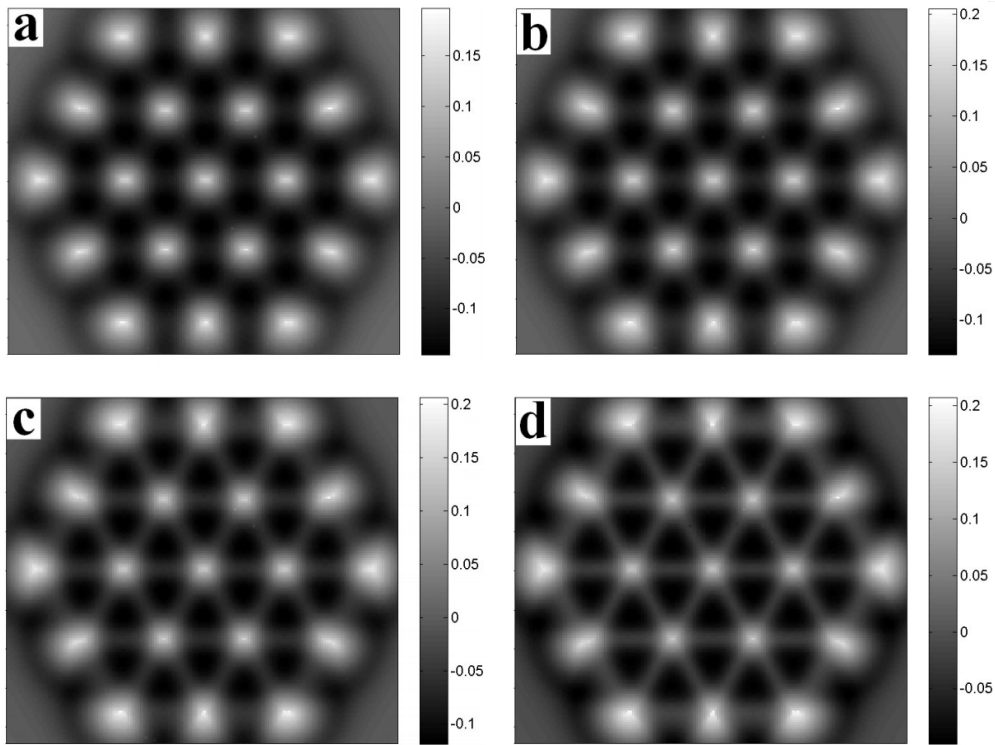


**Figure 5.12:** Simulated constant height NC-AFM images with flexible  $C_{60}$ -functionalized tip for four different tip positions: a) at  $Z = -190$  pm, b) at  $Z = -210$  pm, c) at  $Z = -230$  pm and d) at  $Z = -250$  pm. The sample contains 19  $C_{60}$  molecules and the colour scale shown in nN.

molecules. This is because the simulations do not have periodic boundary conditions and the symmetry is broken when the tip moves outside the physical boundary of the sample.

## 5.5 Simulating AFM images using EHMO theory

Thus far in our calculations, the Lennard-Jones potential has primarily been used to describe the interaction between the probe and sample, which only considers the atom as a sphere and does not include any electronic details. To map the interaction between the molecules while taking into account the interaction between orbitals a more detailed method is required. For this we used the method described in Section 4.4 which takes into account the

## Intermolecular artifacts in AFM images of $C_{60}$ lattices

interaction between orbitals and produces simulated AFM images of  $C_{60}$  island using a  $C_{60}$ -functionalized tip.

To produce constant height simulated AFM images within the repulsive regime through equation (4.44), we first calculated the MOs both for the tip and sample by using extended Hückel molecular orbital theory. The ideal situation would be to consider the overlap between all the orbitals of the tip with all the orbitals of the sample in calculating the kinetic energy change while moving the tip from one position to another over the sample. This requires reasonably good computational capacity, specially when there are several  $C_{60}$  molecules on the sample. However images can still be constructed within a reasonable time frame if only the interactions between the significantly contributing orbitals are considered. To do this, the overlap between all the orbitals on one molecule with all the orbitals on the other molecule is calculated, and only those orbitals with a large overlap are considered in the calculation of the kinetic energy change. As all the overlaps are still calculated, the complete orthogonalisation calculation remains, which greatly reduces the error this assumption imparts on the calculation.

A theoretical AFM image is obtained using a  $C_{60}$  molecule as a tip where two  $C_{60}$  molecules were on the sample separated by  $10.2 \text{ \AA}$  as in the case of a  $C_{60}$  island, shown in Figure 5.13. Please note that during the simulation the tip is not allowed to relax i.e. a rigid  $C_{60}$  terminated tip was used. Also, all the molecules in the system are with the hexagonal face up with respect to the  $+z$  axis. From the image it is clear that there is no bond-like feature between the  $C_{60}$  molecules that are on the sample, though the position of each of the atoms on the hexagonal face can easily be seen. It is also very clear from the image that the 5-6 and 6-6 bond lengths are not equal. During the simulation, when the tip is just above the centre of any  $C_{60}$  molecule on the sample, it experiences forces from all the atoms within the molecule close to the tip. The sum of all these forces produces the bright features that are observed in the middle of each  $C_{60}$  molecule

## Intermolecular artifacts in AFM images of $C_{60}$ lattices

---

on the sample. Presumably if the detailed method of simulating AFM images is adapted to incorporate tip-flexibility, bond-like features between the molecules of the  $C_{60}$  island would be seen. Since in that case the tip would move from higher force region to a local minima the bright feature in the middle of sample molecules would also disappear. However, the lack of bond-like features between the molecules in the simulated image (Figure 5.13) confirms that the tip-flexibility that are used in the simplistic model are the main reason for their appearance when images are simulated using those models (Figure 5.12).

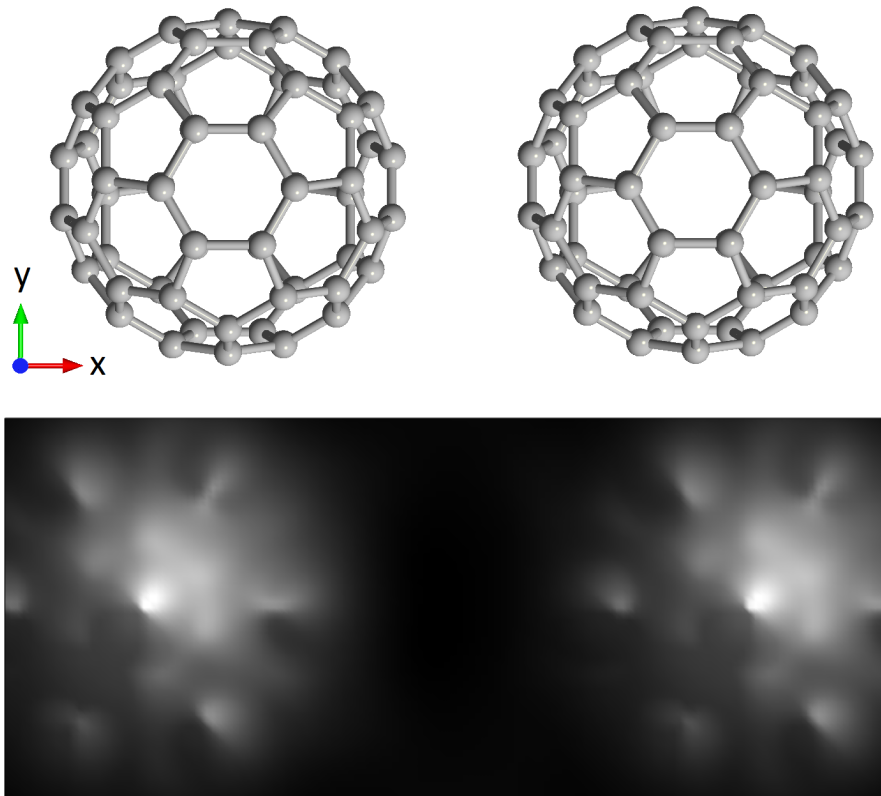


**Figure 5.13:** Ball and stick images of molecular arrangement of  $C_{60}$  (top) which are used to simulated AFM image (bottom) using extended Hückel MO theory.

## 5.6 Orientation-dependent simulation of AFM images

So far in simulating NC-AFM images using the mechanical L-J model (Section 5.4), we have been describing the probe particle as a sphere instead of the real atomic structure of the molecule. In that case, the orientation of the probe does not add any more details in the results. In addition, the experimental images, with which we were comparing our results, are from islands of  $C_{60}$  where all the molecules are orientated with hexagonal face up orientation.

To reveal details of individual molecule and understand the effect of orientations of the probe and sample on the results we now use a  $C_{60}$  as a probe with atomic details, that is we describe the probe with sixty small spheres (each one is a carbon atom) instead of a large sphere to represent the  $C_{60}$ -functionalized tip. The net force on the probe is now calculated by summing the forces experienced by each atom on the probe due to all the atoms in the sample and the tip base. We compare our results with experimental observations shown in Figure 5.14, where a  $C_{60}$  molecule on Si(111)- $7\times 7$  has been studied using a  $C_{60}$ -functionalized tip by Adam Sweetman, The University of Nottingham. It is to be noted that, because of the complex structure of both molecules (functionalized tip and sample), the intramolecular features in these images can not be easily assigned to the molecular structure of the surface-adsorbed molecule as was the case for images taken with simple (i.e. atomic point-like) tip terminations. Hence the orientations of the probe and the sample molecules are not easily determined from the experimental data.

In this particular simulation the Lennard-Jones parameters for the carbon atoms were chosen in light of the work of Girifalco *et al.* [96] and of Chiutu *et al.* [97] and are given in Table 5.2. These are slightly different than the previous case though no significant differences were found in the visual

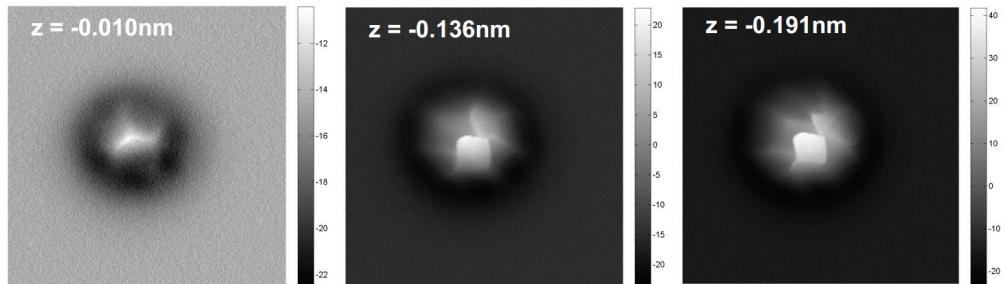


**Figure 5.14:** Constant height frequency shift,  $\Delta f$  AFM images where the tip-sample heights are given relative to the  $\Delta f$  setpoint used for atom-tracking over the molecule.

pattern of the simulated images obtained by using either set of L-J parameters. However, in terms of quantitative values, simulated results obtained using the values given in Table 5.2 provides a better match with the works of Girifalco *et al.* [96] and Chiotu *et al.* [97]. The lateral stiffness for the probe was set to  $k_{xy} = 0.5 \text{ Nm}^{-1}$ , though we discuss the effect of varying  $k_{xy}$  with a specific tip-sample orientation later. We acquired the simulation data by scanning the sample laterally with a step of  $\Delta x, \Delta y = 0.1 \text{ \AA}$ . At each lateral position we placed the tip base at  $z_0 = 22 \text{ \AA}$  and approached the sample in steps of  $\Delta z = 0.1 \text{ \AA}$  until  $z = 17.5 \text{ \AA}$  allowing the probe position to be relaxed at each step in the combined force of the sample and tip base.

**Table 5.2:** Lennard-Jones parameters.

Atom/Particle	$\epsilon_\alpha$ (meV)	$r_\alpha$ ( $\text{\AA}$ )
C	2.500	1.966
Tip base	1000	5.000

To visualize the variation of the potential energy across the molecules, we calculated the potential energy between the probe and the sample at each  $(x, y, z)$  position of the tip from the relaxed probe position during the relaxation. Although the orientations of the probe and the sample molecules used in the simulation are not the orientations of  $C_{60}$  molecules in the

## Intermolecular artifacts in AFM images of $C_{60}$ lattices

experiment (as the orientations of the tip and the sample are not known from the experiment), qualitatively similar features are found both in simulation (Figure 5.15) and experiment (Figure 5.14). In particular the simulations reproduce the ‘sharpening’ of the features observed in the constant height experimental images.

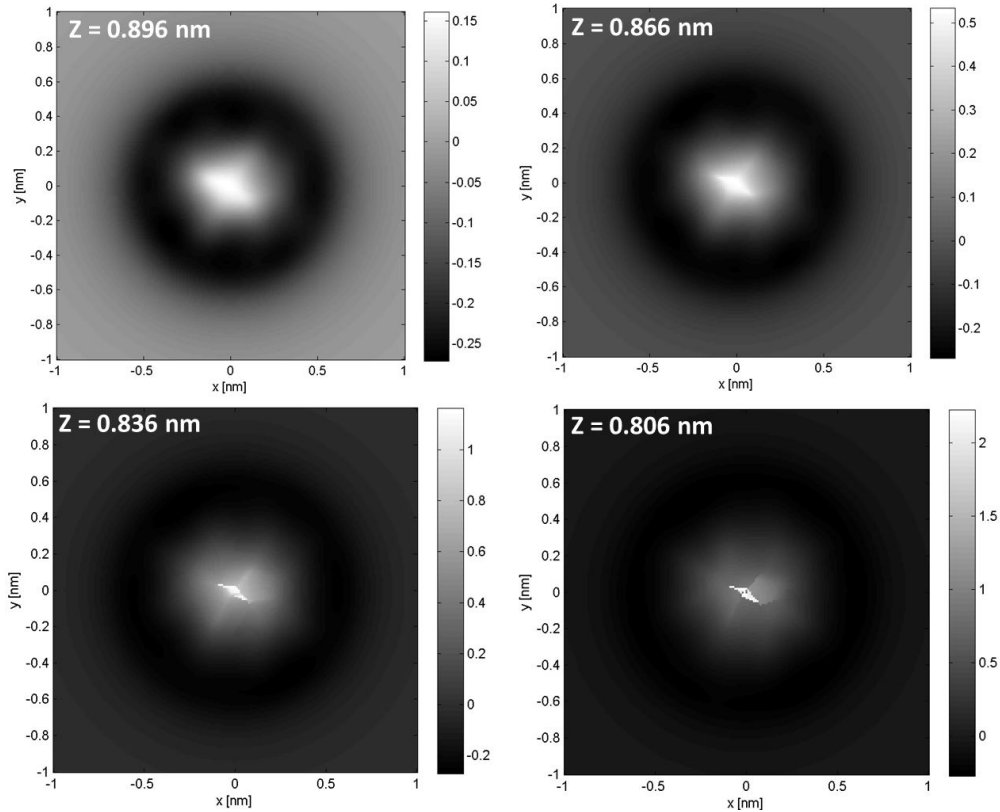


**Figure 5.15:** Constant height energy images using the tip-sample configuration described in Fig. 4i of Lakin *et al.* [98] where  $z$  is the distance between the centers of probe and sample  $C_{60}$  as shown in Figure 5.16 B.

A potential minima,  $U_{\min}$ , image is constructed by projecting the minimum value of the potential at each vertical column in the 3D data set over a  $xy$  plane, Figure 5.16 C. This provides an immediate and intuitive way of visualising the strength of the equilibrium interaction as the relative position of the functionalized tip and sample is varied. It is to be noted that the value of the minimum in the potential energy curve only has a directly interpretable physical meaning when the actual minimum of the potential

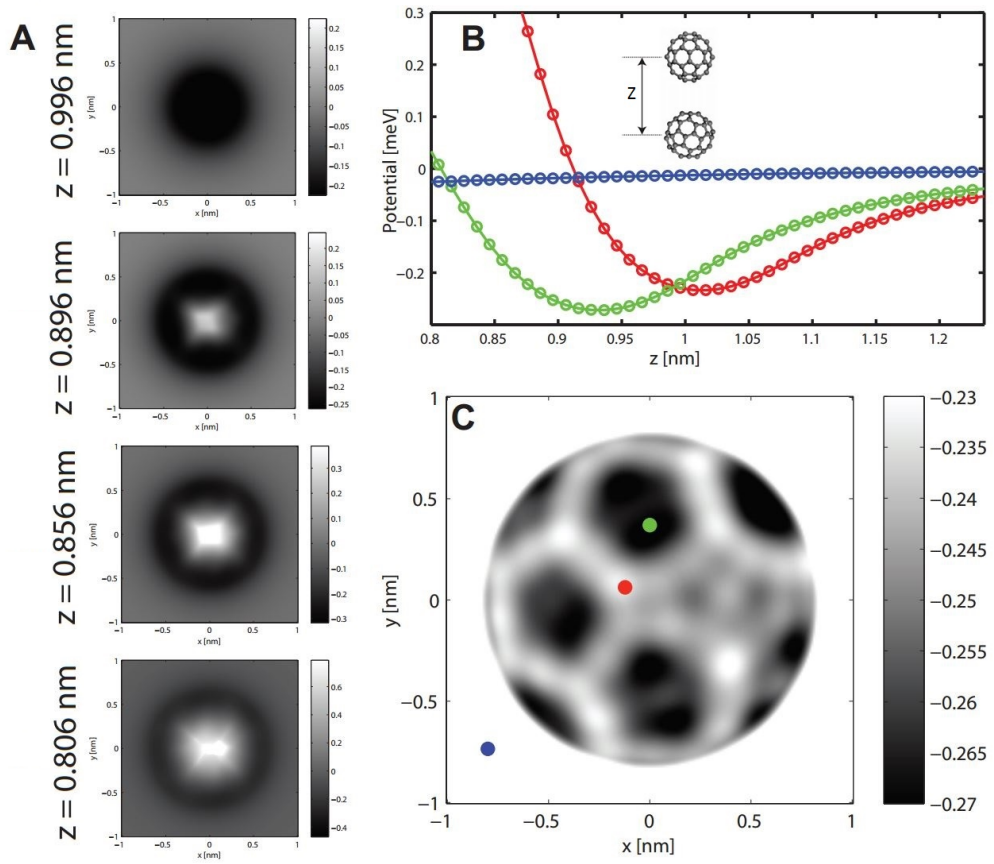


**Figure 5.16:** A) Constant height energy images and C)  $U_{\min}$  image showing contrast for probe  $C_{60}$  oriented double bond down on a surface  $C_{60}$  orientated in the orientation describe in Fig. 6d of Lakin *et al.* [98] B) representative single  $U(z)$  curves over the locations indicated in C).  $z$  is the distance between the centres of the probe and sample  $C_{60}$ s.

is present in a given  $U(z)$  curve (i.e. the turnaround in the  $U(z)$  curve is present in the data set). If the minimum is not reached then the closest point of approach will usually be identified as the minimum value. We therefore also map the height of the potential energy minimum in terms of  $z$ , which yields a complementary map of  $z_{\min}$ . By masking the  $U_{\min}$  map with the  $z_{\min}$  map we can exclude those curves which do not contain the  $U(z)$  turn around, and visualise only the region of the image which can be interpreted directly as representing the intermolecular interaction minima.

We show the effect of varying the lateral stiffness  $k_{xy}$  on the  $U_{\min}$  and energy images for high symmetry orientations, hexagon face probe on a hexagon

face sample in Figure 5.17. Though the effect is quite visible on the ‘sharpening’ features of the energy images, almost no variation is found in the  $U_{\min}$  images. This is expected and also reported by Hapala *et al.* [44]. This is because of the more complex interaction between the two C<sub>60</sub>s. Specifically, for lower stiffness we sometimes observe numerical convergence issues in the simulation that remain even when very high numerical tolerances and numbers of convergence steps are used. This could be because of artificially trapping the probe in certain positions over the sample, suggesting a more sophisticated energy minimisation routine is required to take into account the more complex energy landscape for the C<sub>60</sub>-C<sub>60</sub> interaction in this regime.

Most of the simulated AFM images presented in Section 5.4 have C<sub>60</sub> molecules at the sample with a hexagon-up orientation, and we did not find any noticeable difference in the results because of the orientation of C<sub>60</sub> molecules in the island. The probe in those simulations was a sphere of radius of  $r_{\alpha} = 5.00 \text{ \AA}$  in order to approximate a C<sub>60</sub>-terminated tip. However in the present case where we are using a C<sub>60</sub> as a probe with atomic detail, we find that different orientations of the probe and sample C<sub>60</sub>s yield qualitative and quantitative differences on the energy curves and energy images.

We present the energy curves and energy images for some of the well-known orientations in Figure 5.18. From these images we observe that the energy curves and energy images vary significantly because of the orientations of the probe and the sample C<sub>60</sub> molecules. Since because of different configurations of the sample and the tip molecules the distance between the bottom carbon atom of the tip C<sub>60</sub> and the top carbon atom in the sample C<sub>60</sub> changes while the distance between the centres of the molecules remain same, the minima of the energy curves shifts depending on the tip-sample configuration. To investigate the effect of orientations of the probe and the sample molecules in more detail, we also performed simulation with some

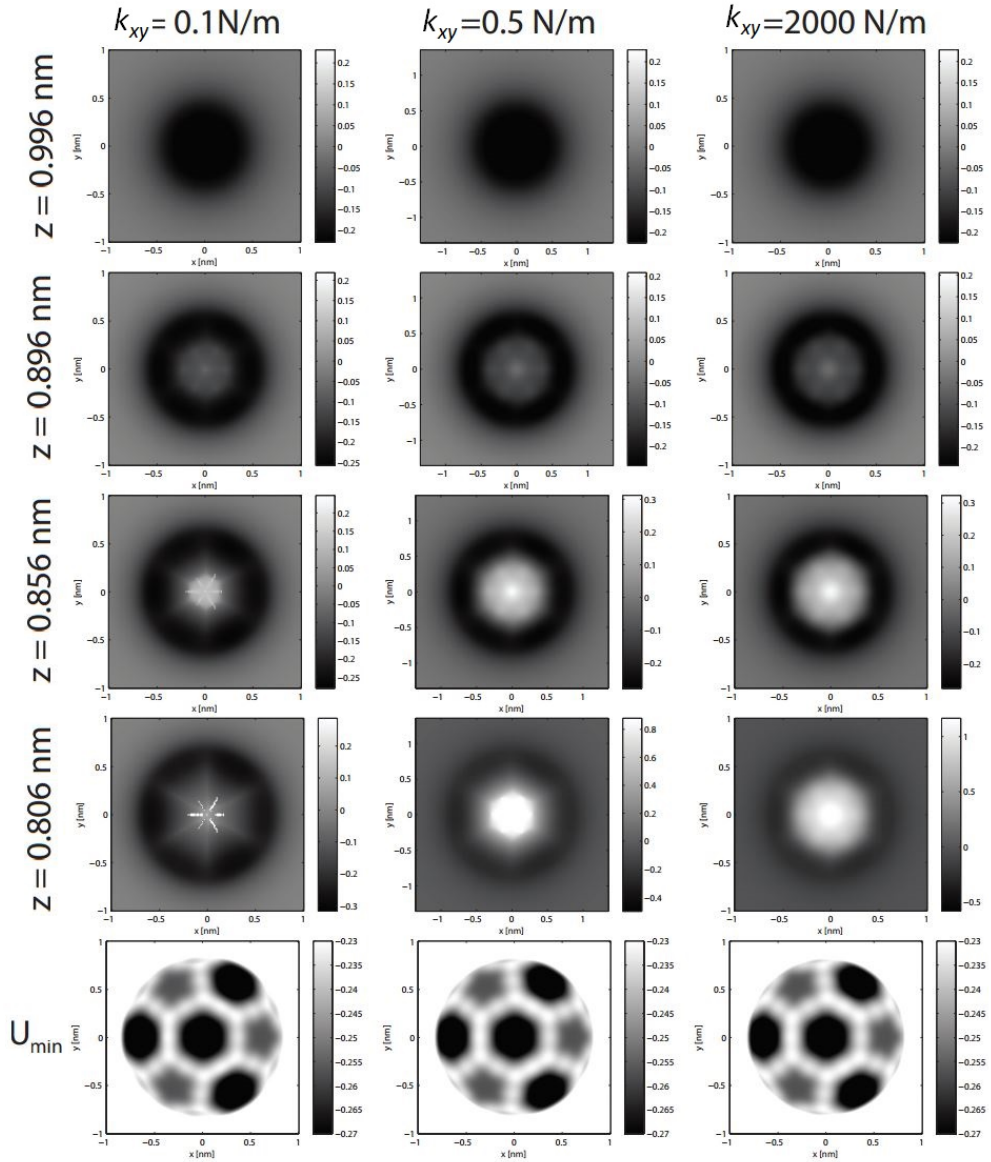


**Figure 5.17:** Constant height energy images and  $U_{\min}$  images showing changes in imaging due to variation in lateral stiffness  $k_{xy}$ . Almost no variation is found in  $U_{\min}$  images though the effect of  $k_{xy}$  on the ‘sharpening’ features of the energy images is quite visible.  $z$  is the distance between the centres of the probe and sample  $C_{60}$ s.

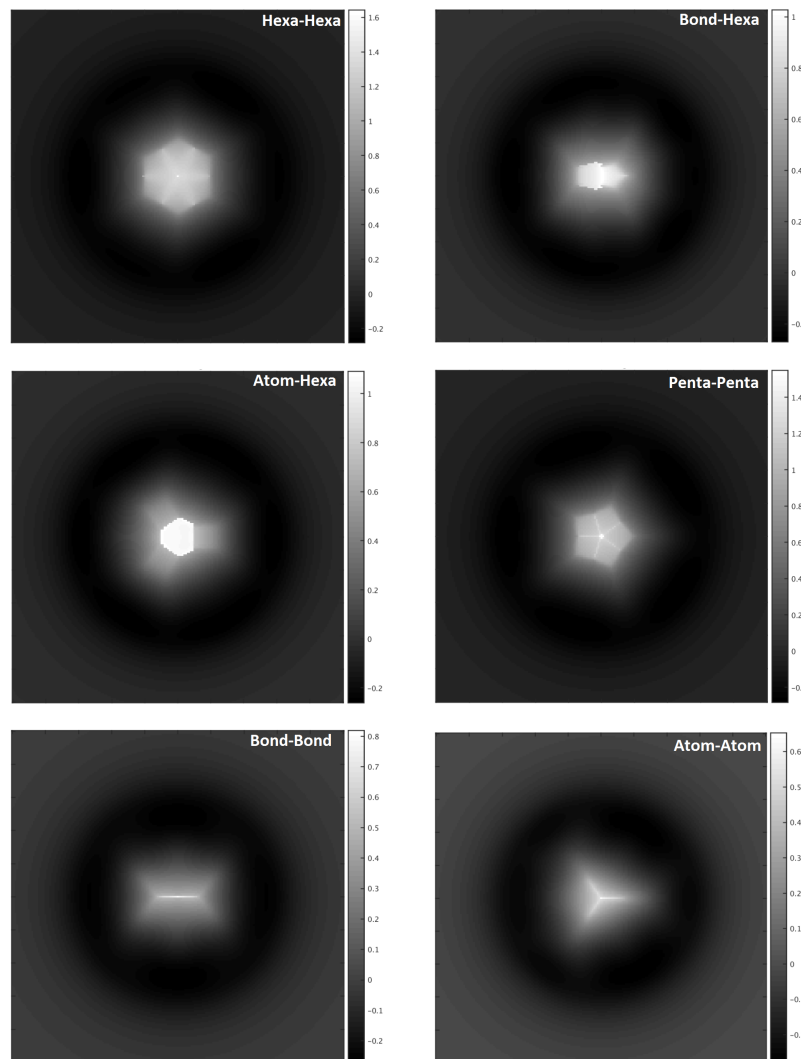
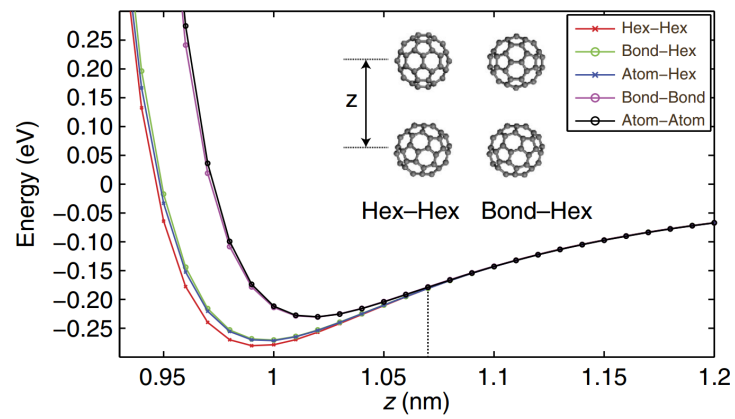


**Figure 5.18:** Variation in potential energy curve due to variation in rotational orientation of probe and sample  $C_{60}$  molecules (top); the terms in the legend refer to the facing part of the molecule and inset, representative ball-and-stick models showing two of the simulated orientations. Simulated AFM images for different tip-sample configurations are also shown and are labeled according to orientations of the tip and sample  $C_{60}$  molecules.

other orientations of the probe and the sample molecules. The configuration of the probe is shown in Figure 5.19, while the orientations of the sample and the obtained results are presented in Figure 5.20, Figure 5.21, and Figure 5.22. In each of these case we also present the  $U_{\min}$  image and energy curves at three different positions on the sample. From these results we conclude that molecular configurations with lower symmetry produce much more complex patterns in the  $U_{\min}$  and energy image, which is to be expected. By tuning parameters of the L-J potentials and the configurations of probe and sample, it is likely to have a very good agreement between the simulated and experimental images.

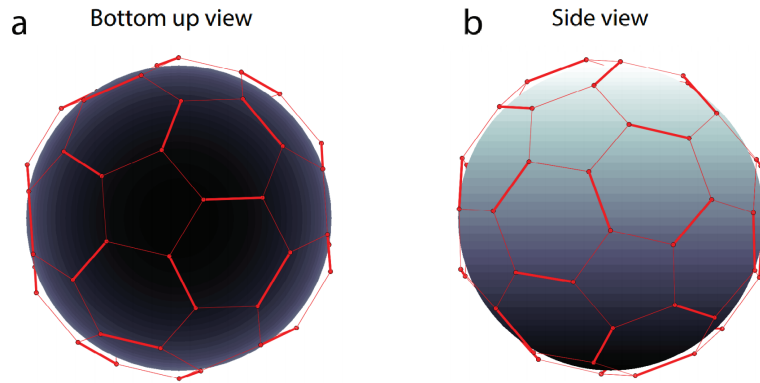


**Figure 5.19:** Bottom up view (i.e. view from the surface molecule position) of the tip  $C_{60}$ , orientated with a tilted pentagon down. b) Side view of probe  $C_{60}$ .

## 5.7 Conclusions

In summary, we have reproduced the experimental observation of features appearing as artificial intermolecular bonds in 2D assemblies of  $C_{60}$  molecules. During simulation these features are only visible if the NC-AFM probe is terminated with a flexible  $C_{60}$  molecule, capable of relaxing in the tip-sample junction. The choice of lateral stiffness  $k_{xy}$  of the interaction between tip base and the functionalized probe particle, which is a measure of the flexibility of the probe, plays a key role in observing the intermolecular features

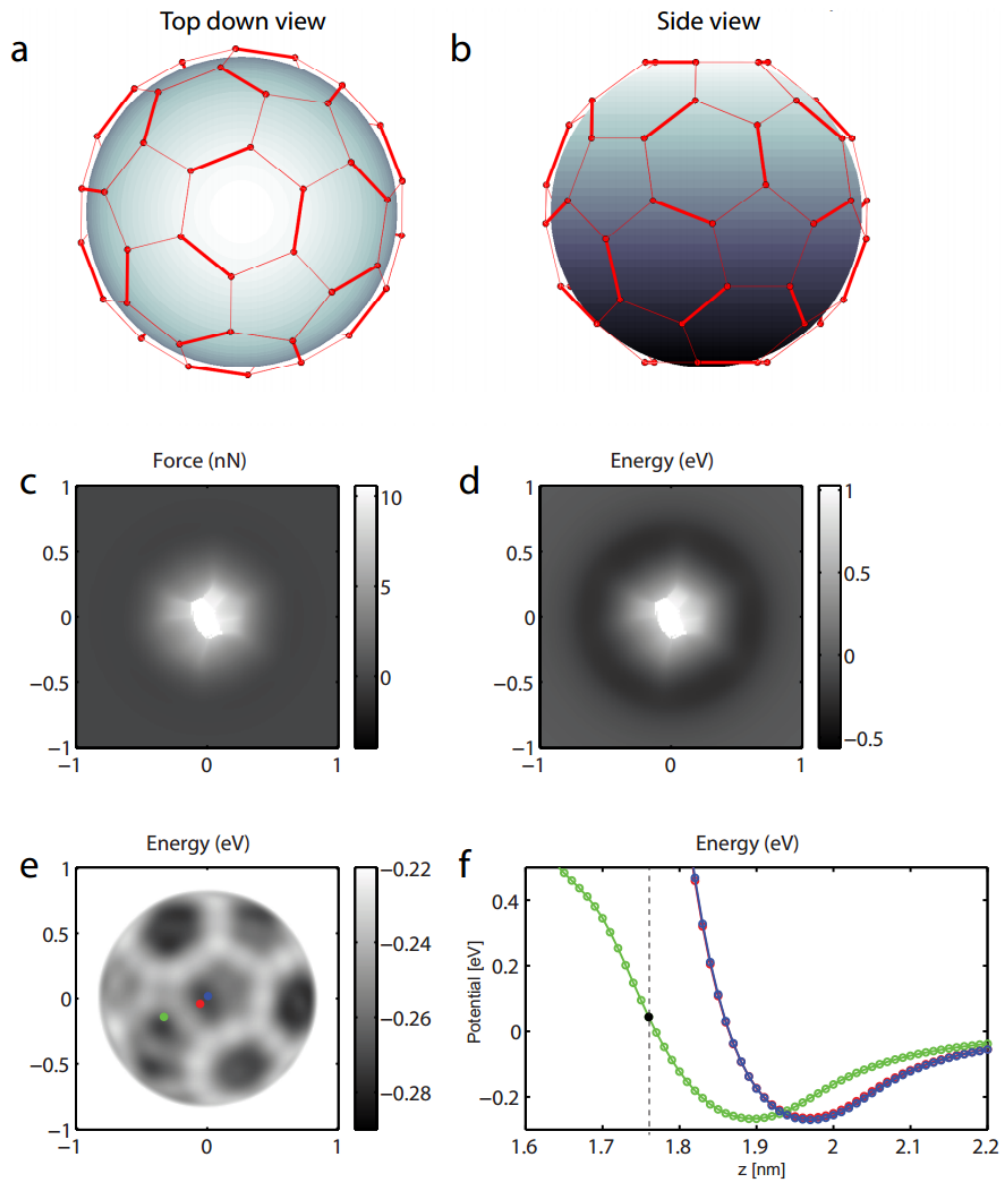


**Figure 5.20:** a) Top down view (i.e. view from the tip molecule position) of the surface  $C_{60}$ . b) Side view of surface  $C_{60}$  molecule c) Simulated constant height force image (in nN) at close approach. d) Simulated constant height energy image (in eV) at close approach e) Simulated  $U_{\min}$  image. f) Representative  $U(z)$  curves taken at the positions indicated in e), black dot indicates position of constant height images.

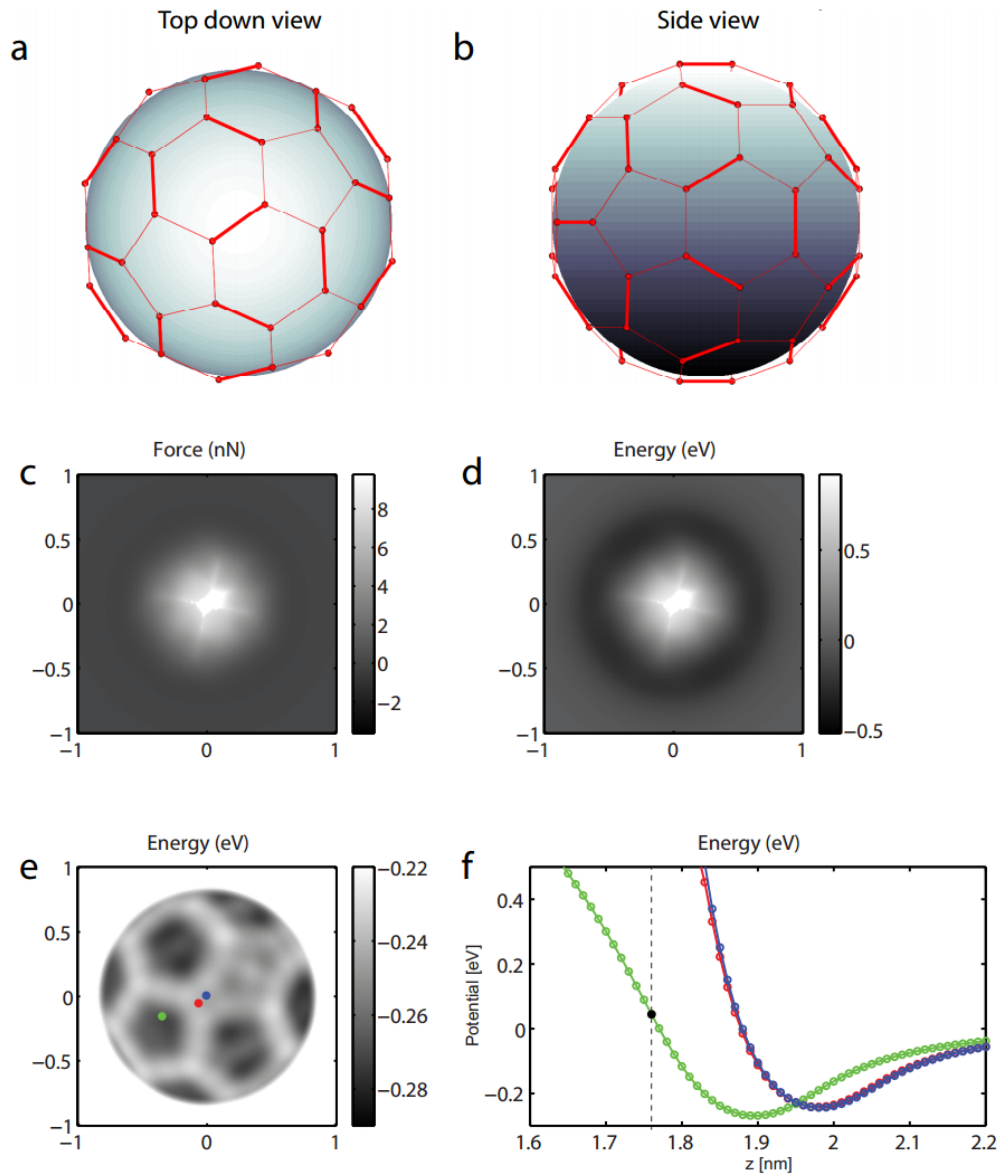


**Figure 5.21:** Same as Figure 5.20 but for different orientation of the sample.

in the non-planar, van der Waals-mediated fullerene system. For a isolated  $C_{60}$  molecule, the AFM images were simulated with atomic detailed  $C_{60}$ -terminated probe. Our results suggests that if the actual configuration of the tip and sample  $C_{60}$  molecules during the AFM experiment is known, it would be possible to have a better match between the experimental and simulated results.

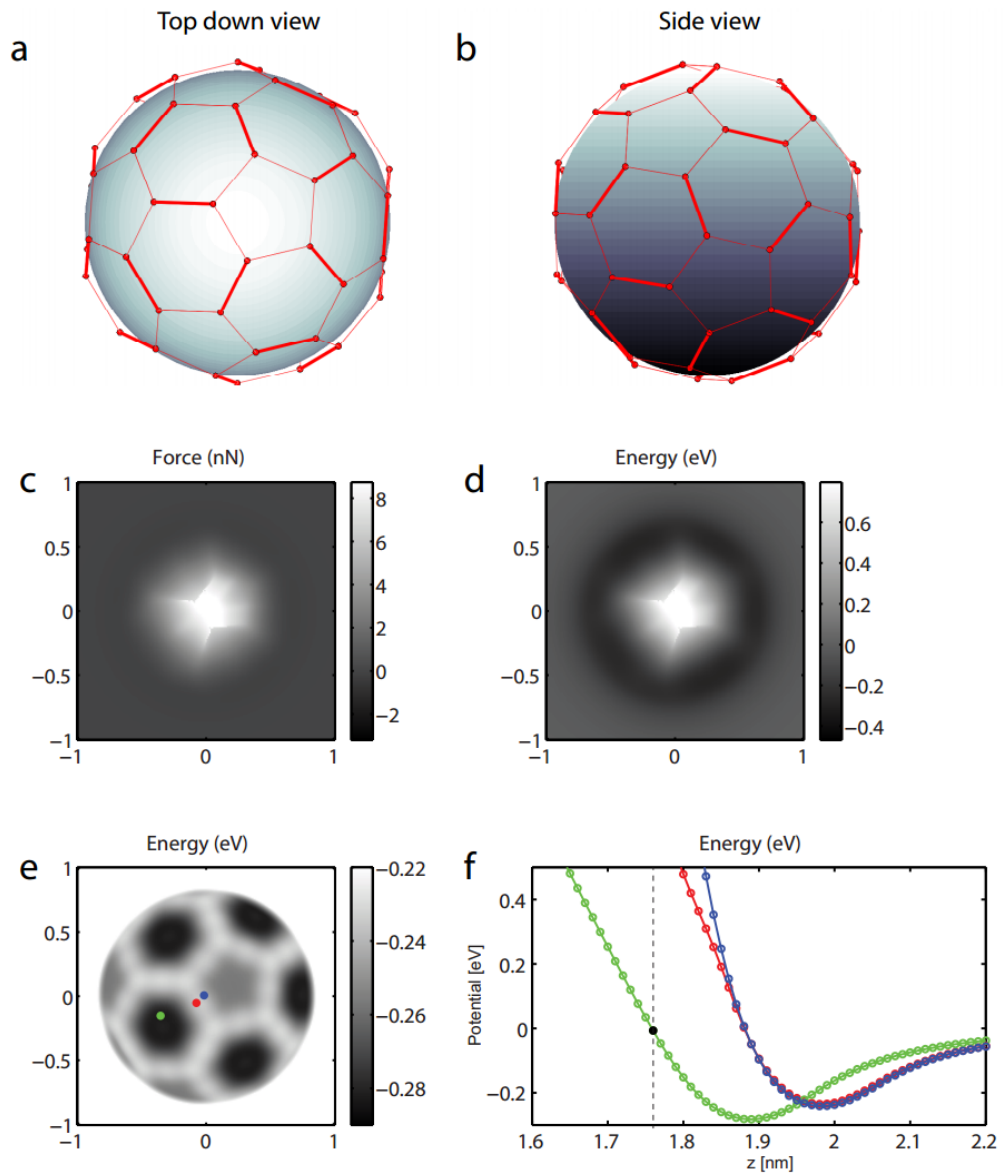


**Figure 5.22:** Same as Figure 5.20 but for different orientation of the sample.

# Modeling STM images of $C_{60}F_{48}$ using Hückel theory

---

Among the known fluorofullerenes,  $C_{60}F_{48}$  is the highest intact adduct derived from  $C_{60}$  to be obtained in significant quantities, and has the highest fluorine content per fullerene. Because of its high electron affinity even in the gas phase [99] and high reduction potential [100], it is interesting to study  $C_{60}F_{48}$  (both theoretically and experimentally) to explore its properties.  $C_{60}F_{48}$  also has the probability to be used as a dopant. The presence of isomers of  $C_{60}F_{48}$ , with  $D_3$  and  $S_6$  symmetries, are proven by experiment [101] (Figure 6.1). The typical C-F bond length in the molecule is 1.368 Å and the distance of all the C atoms from the centre is not the same, unlike  $C_{60}$ . In  $C_{60}F_{48}$  for the carbon shell the radii of the  $sp^3$  atoms that are not bonded to  $sp^2$  are 3.937 Å, for  $sp^3$  atoms bonded to  $sp^2$ , 3.78 Å while the radii of  $sp^2$  atoms lie between 3.017 Å to 3.190 Å [102].

The  $C_{60}F_{48}$  molecule, is a heteroatom system. Although we cannot use simple HMO theory, modified HMO theory and EHMO theory can be used to construct the MOs of the  $C_{60}F_{48}$ . As a starting point we considered the molecule to be spherical of radius 3.555 Å for the carbon cage, just like

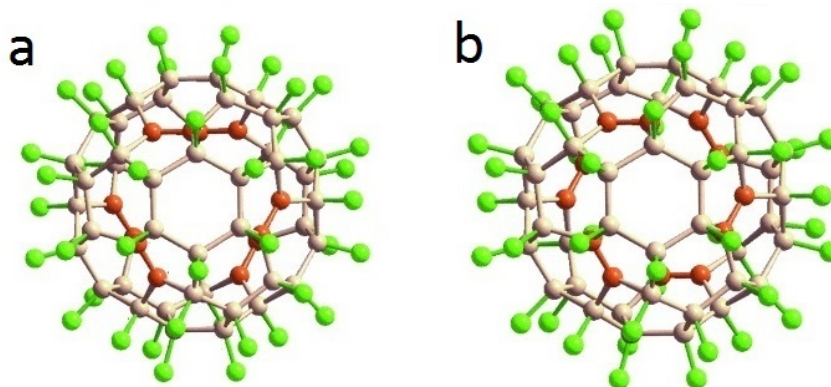


**Figure 6.1:** a)  $D_3$  and b)  $S_6$  isomers of  $C_{60}F_{48}$  with double bonds and  $sp^2$  carbons in orange colour. Images are taken from reference [101].

$C_{60}$  with fluorine sticking out from carbon atoms having a C–F distance of 1.368 Å. With this in mind, first we shall discuss the construction of MOs of  $C_{60}F_{48}$  using modified HMO theory then we shall extend this for EHMO theory. Finally, theoretical constant current images will be produced which will then be compared with experimental results.

## 6.1 Constructing molecular orbitals of $C_{60}F_{48}$ using modified HMO theory

The first step in constructing the Hückel Hamiltonian using modified HMO theory is to identify the atoms within the molecule that are contributing to the  $\pi$  bonding. All 108 (= 60 carbon + 48 fluorine) atoms in  $C_{60}F_{48}$  have their share in the  $\pi$ -bonding network of the molecule. Next, since the nearest neighbour of C can be F or C or both, while for F it is only C, we need to choose the scaling factors,  $k_{C-C}$ ,  $h_F$  and  $k_{C-F}$ . The scaling factors  $h_F$  and  $k_{C-F}$  for fluorine, taken from [63], are 3.0 and 0.7 respectively. For C–C interaction we used  $k_{C-C} = 1$ , neglecting the variation in bond lengths for 5-6 bond and 6-6 in the carbon cage, which simplifies the calculation. With these parametric values a  $108 \times 108$  Hückel Hamiltonian is constructed for  $C_{60}F_{48}$  in a similar way as described for  $C_4H_6$  in Section 4.1. The Hamilto-

nian is a purely numerical matrix and is diagonalized using Mathematica.

While using the simple or modified HMO theory for planar molecules it is enough to consider the  $p$  orbital that are normal to the plane of the molecule. However, as  $C_{60}F_{48}$  is three dimensional and all atoms are contributing to the  $\pi$  bonding it is necessary to define the basis as a set of 108  $p$  orbitals pointing radially outwards from each atomic position. To construct a radial  $p$  orbital  $p_r$ , the molecule is centered at the origin and a linear combination of  $p_x$ ,  $p_y$  and  $p_z$  orbitals are used. The dot product between the unit vector pointing an atom at  $(a_x, a_y, a_z)$  in  $C_{60}F_{48}$  and three  $p$  orbitals centered at that atomic position gives the required  $p_r$  orbital for that particular atom:

$$\begin{aligned}
 p_r &= \frac{1}{\sqrt{a_x^2 + a_y^2 + a_z^2}} (a_x, a_y, a_z) \cdot (p_x, p_y, p_z) \\
 &= \frac{1}{\sqrt{a_x^2 + a_y^2 + a_z^2}} (a_x(x - a_x) + a_y(y - a_y) + a_z(z - a_z)) \times \\
 &\quad \left(\frac{\alpha^5}{\pi}\right)^{1/2} e^{-\alpha\sqrt{(x-a_x)^2+(y-a_y)^2+(z-a_z)^2}}. \tag{6.1}
 \end{aligned}$$

Here we have used the Cartesian expression of  $2p$ -type STO. The mathematical function of each MO can then be found from the LCAO specified by the corresponding eigenvector.

## 6.2 Constructing molecular orbitals of $C_{60}F_{48}$ using EHMO theory

In the case of EHMO theory, the full electronic basis consists of  $2s$ ,  $2p_x$ ,  $2p_y$  and  $2p_z$  orbitals centered at each atomic position for all 108 atoms within the  $C_{60}F_{48}$  molecule are considered. As a result, the MOs will be given as a linear combination of 432 ( $= 4 \times 108$ ) atomic orbitals. To construct the Hückel Hamiltonian  $\mathcal{H}$ , of size  $432 \times 432$  of  $C_{60}F_{48}$  we first need to define the diagonal elements. These values are not calculated explicitly rather taken to be the negative of the ionisation potential for the particular orbital. In our

## Modeling STM images of $C_{60}F_{48}$ using Hückel theory

---

case we have taken them from reference [65] though they can be fine tuned to match the experimental results. The values of the diagonal elements are (in eV):

$$H_{ii}^{C2s} = -21.4$$

$$H_{ii}^{C2p} = -11.4$$

$$H_{ii}^{F2s} = -40.0$$

$$H_{ii}^{F2p} = -18.1$$

It is to be noted that each  $p$  orbital of an atom will have the same ionisation potential.

Next, we need to calculate the off-diagonal elements to complete the construction of the matrix. We start that by calculating electronic overlaps  $S_{ij}$ , of the atoms, which then will be used (as in Eq. (4.11)) to find the off-diagonal elements of the Hamiltonian. The overlap between the orbitals of the atoms can be calculated through the integral:

$$S_{ij} = \int \psi_i \psi_j d\tau \quad (6.2)$$

where  $\psi_i$  and  $\psi_j$  are the two orbitals, and  $\tau$  indicates an integral over all space. To calculate these integrals, along with STO-6G Gaussian basis set, the following Gaussian functions are used in this study ( $\alpha$  being Gaussian exponent).

$$\phi_{2s} = \left(\frac{2\alpha}{\pi}\right)^{3/4} e^{-\alpha(x^2+y^2+z^2)} \quad (6.3)$$

$$\phi_{2p_i} = 2\alpha^2 \left(\frac{2\alpha}{\pi}\right)^{3/4} i e^{-\alpha(x^2+y^2+z^2)}; \quad \{i = x, y, z\} \quad (6.4)$$

With these, the full Hamiltonian is constructed which for  $C_{60}F_{48}$  is a  $432 \times 432$  numerical matrix. This is then diagonalised to give the MOs of the molecule and their respective energies.

Finally, to normalize the MOs, consider a particular MO which can be written as:

$$\Psi = \sum_i c_i \psi_i, \quad (6.5)$$

where  $i$  sums over all atomic orbitals and  $c$  is the coefficient defined by the corresponding eigenvector. The normalization condition for the MO requires that

$$\int \left( N \sum_i c_i \psi_i \right)^2 d\tau = 1, \quad (6.6)$$

where  $N$  is the normalization constant. Rearranging the above equation we have

$$N^2 \sum_i \sum_j c_i c_j \int \psi_i \psi_j d\tau = N^2 \sum_i \sum_j c_i c_j S_{ij} = 1. \quad (6.7)$$

Hence, the normalization constant of a particular MO is given by

$$N = \left( \sum_i \sum_j c_i c_j S_{ij} \right)^{-\frac{1}{2}}. \quad (6.8)$$

Though in EHMO all the orbitals are used, it can be seen from the eigenvalues that some orbitals has very little contribution to the final MO and they decay at a higher rate. This means that their contribution at a distance observed during STM is insignificant compare to other orbitals.

### 6.3 Incorporating the surface interaction

The effect of the substrate on the adsorbed molecule during SPM can be incorporated by directly modifying the diagonal elements of the Hückel Hamiltonian. In our calculation we approximate the effect of the substrate

## Modeling STM images of $\text{C}_{60}\text{F}_{48}$ using Hückel theory

---

on the energies of the electrons associated with the orbitals of each atom using the Lennard-Jones potential, Eq. (2.2). The atoms closer to the surface were perturbed most and the effect become lesser with the increase of distance of an atom in the molecule from the surface. The interaction was included by adding a Hamiltonian  $H^s$  which represent the surface interaction to the Hückel Hamiltonian  $\mathcal{H}$ . Therefore, the resultant Hamiltonian becomes

$$H_{\text{eff}} = \mathcal{H} + H^s. \quad (6.9)$$

Here,  $H^s$  is a diagonal matrix which only modifies the diagonal elements of the Hamiltonian  $\mathcal{H}$  constructed from any of the Hückel theories and has the form

$$H_{ii}^s = E_i^s(z) \quad (6.10)$$

$$H_{ij}^s = 0. \quad (6.11)$$

$E_i^s(z)$  is the energy function of Lennard-Jones type acting on  $i$ th atom in the molecule,

$$E_i^s(z) = \epsilon \left[ \left( \frac{r_0}{r_i(z)} \right)^{12} - 2 \left( \frac{r_0}{r_i(z)} \right)^6 \right]. \quad (6.12)$$

$r_i(z)$  is the perpendicular distance of  $i$ th atom to the surface. The multiplication constant  $\epsilon$  is used to alter the strength of the interaction. It is found that the value of  $\epsilon$  does not affect the MOs significantly unless its extremely large. In our calculation it was 0.25 eV. The value of  $r_0$  is usually chosen to be the bond length between the atom of the molecule and the atom of the surface. For our calculation we have taken  $r_0 = 5 \text{ \AA}$  since we didn't specify the surface type. The values of  $\epsilon$  and  $r_0$  may be tuned to match the experimental outcomes. Diagonalising the effective Hamiltonian  $H_{\text{eff}}$ , provides the MOs, and reveals any degeneracies caused by the external interaction.

## 6.4 Simulating a constant current STM image

The STM image of a molecular orbital can be simulated by using the formalism discussed in Section 4.2. Here we shall simulate constant current images since we are comparing our results with experimental constant current images only. However, theoretical constant height images can also be produced following a similar procedure. For an  $s$ -type tip, the current  $I_s$ , observed during STM is proportional to the sum of the squares of the MOs under consideration, evaluated at tip position  $(x, y, z)$ . This can be written mathematically as:

$$I_s \propto \sum_{i=1}^j \Psi_i(x, y, z)^2, \quad (6.13)$$

where  $\Psi_i$  is the  $i$ th MO for a  $j$ -fold degenerate state. The exact value of the current  $I_s$ , can be determined by knowing the tunnelling transition probability i.e. by accurately determining the tunnelling matrix element. However, it is not necessary to know the value of true current when constructing qualitative images rather a current  $I'_s$ , can be chosen to have a best match with the experiment. With this in mind we can rewrite Eq. (6.13) as:

$$\sum_{i=1}^j \Psi_i(x, y, z)^2 = I'_s, \quad (6.14)$$

where the value of the current  $I'_s$ , is proportional to the true current that is observed experimentally.

In simulating a theoretical image, the height adjustment of the tip is taken to always be along the  $z$  axis, while the raster scan is taking place in  $x$  and  $y$  directions. Once the value of  $I'_s$  is chosen, for a particular  $(x, y)$  position Eq. (6.14) is solved to find the correct tip height value i.e. the  $z$  value. As

## Modeling STM images of $C_{60}F_{48}$ using Hückel theory

---

there are multiple solution of this equation, the highest solution of  $z$  is taken to be the tip height. This corresponds to the point at which the tunnelling current would first be observed by an  $s$  orbital approaching the sample from above. The process is repeated with different  $(x, y)$  values as the tip scans over the sample. The solutions of  $z$  are saved for the corresponding  $(x, y)$  values and the simulated constant current image is produced by plotting this three dimensional data.

Images are plotted for several MOs and simulated constant current images are produced by solving Eq.(6.14) for the corresponding MO by using Hückel theory. Thses results are shown in Figure 6.2 and Figure 6.3. Results obtained through modified HMO theory are shown in Figure 6.2 while Figure 6.3 shows the images obtained through modified HMO theory. Simulated constant current STM images that are found to have stripes similar to those of experiment images are shown in Figure 6.4. The STM experiment was performed by Sharp [103] as a part of his PhD work at the University of Nottingham. Although theoretical images have similar pattern, no exact match was found with experiment. One reason for this could be the choice of a simple tip in producing the theoretical images. In our calculation the tip is assumed to be  $s$ -type while the exact state of the experimental tip is not known. However, due to the presence of fluorine atoms in the system it is very likely that the tip could have one or more fluorine atoms attached to it, or it could even have an attached  $C_{60}F_{48}$ . In addition, from the experimental images neither the condition of the substrate on which  $C_{60}F_{48}$  molecules were nor the type of interaction that the molecule has with the surface can be understood clearly. We do not know if there is any defect on the substrate under the  $C_{60}F_{48}$  molecule. The orientation of the molecule during the STM experiment was also unknown .

Constant current STM images with a  $p_z$ -type tip were also simulated for a few orientations of  $C_{60}F_{48}$ , but as expected no significant differences were seen comparing with the images produced with  $s$ -type tip, so they are not

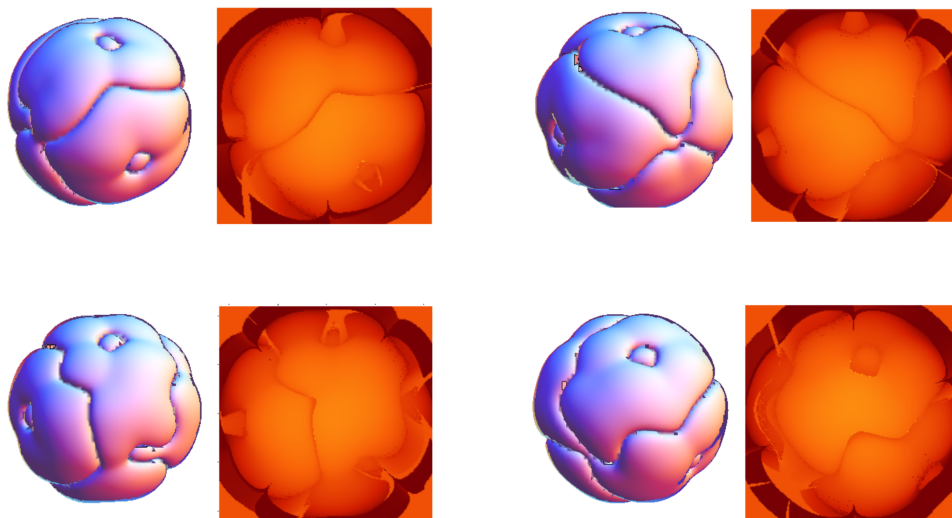


**Figure 6.2:** Plot of MOs and simulated constant current images of  $C_{60}F_{48}$  for different orientations of the molecule via modified HMO.

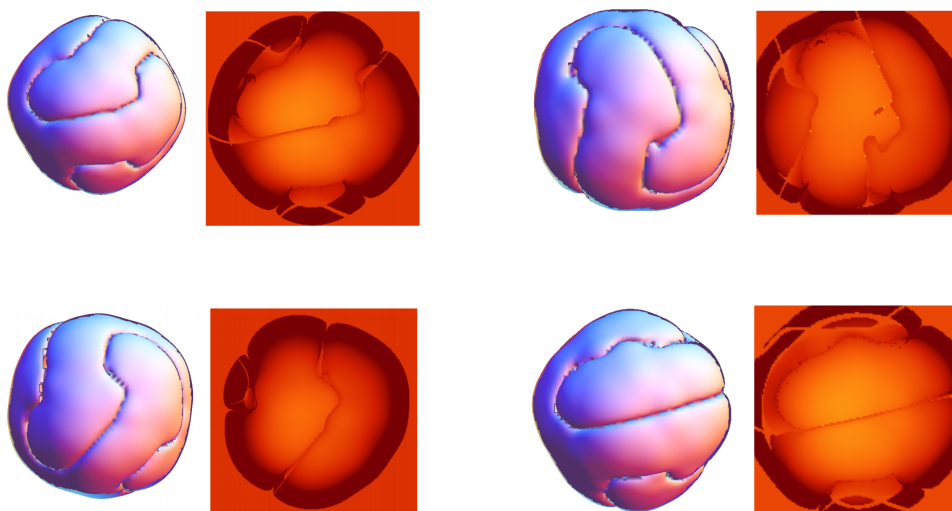


**Figure 6.3:** Plot of MOs and simulated constant current images of  $C_{60}F_{48}$  for different orientations of the molecule via EHMO.

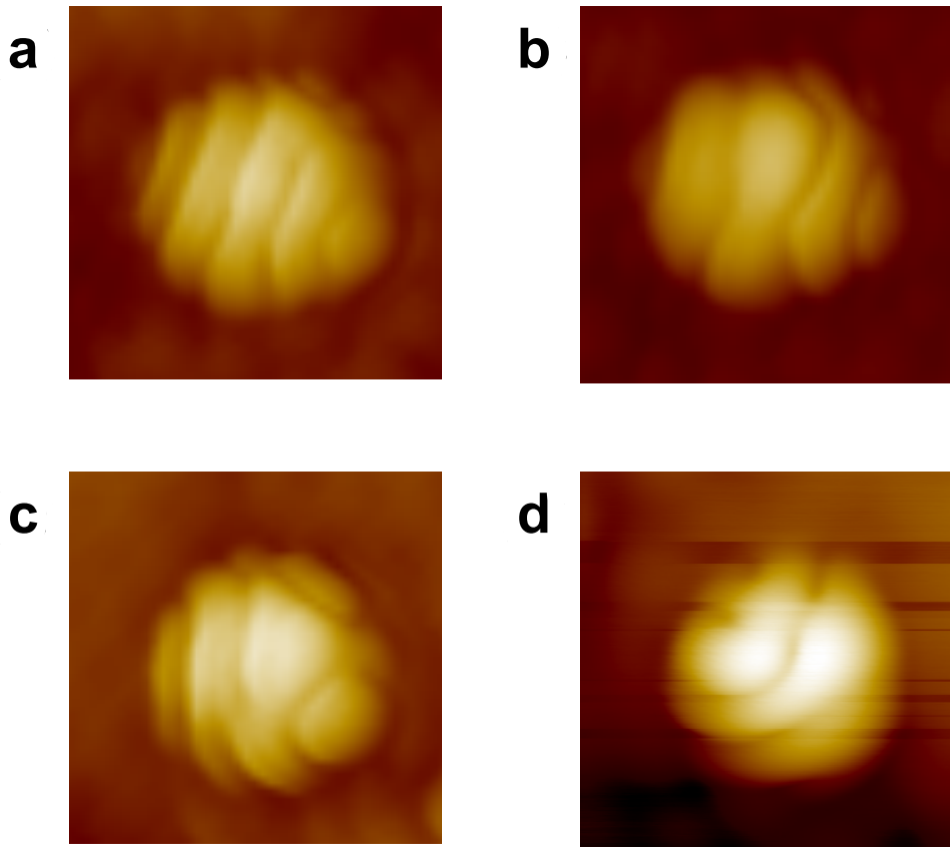


**Figure 6.4:** Images of single  $C_{60}F_{48}$  molecules on Ag:Si(111) acquired with a bias of +2.5V. The set points for the images were for a), b) and c) 10 pA, and for d) 350 pA. a) and b) were situated on Si(111)-(7×7) surface whereas c) and d) were on silver-passivated regions. The STM experiment was performed by Sharp [103].

presented here. This is also true for the case of  $C_{60}$  and was confirmed by Lakin [78] in his PhD thesis. Constant current simulation with  $p_x$  and  $p_y$  tip states was also produced. Figure 6.5 shows a typical result of the simulation having more stripes compare to  $s$  or  $p_z$  tip states. In principle it would be possible to simulate images with other tip states, even with  $C_{60}F_{48}$  tip. However, it was shown by Chiutu *et al.* [97] that  $C_{60}$  imaging with  $C_{60}$  has many unknown parameters relating to orientations, so  $C_{60}F_{48}$  imaging with  $C_{60}F_{48}$  would involve even more unknowns because of its lower symmetry. Also, in that case the images would be expected to look very different because of the complex tip state.

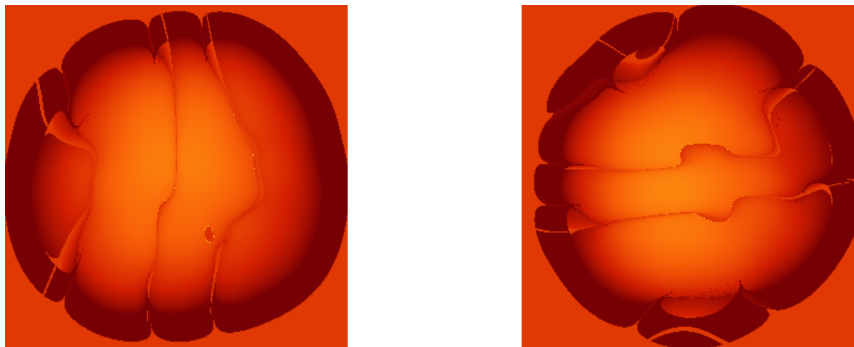


**Figure 6.5:** Constant current simulated images of LUMO of single  $C_{60}F_{48}$  using  $p_x$ -type (left) and  $p_z$ -type (right) tip functions. These images are from two different orientations of  $C_{60}F_{48}$ .

It is also important to mention that, so far a symmetric carbon cage was used for  $C_{60}F_{48}$  just like  $C_{60}$  with a radius of  $3.555 \text{ \AA}$ . However using  $D_3$  or  $S_6$  symmetry would not make any significant changes in the simulated images. A good STM has lateral resolution of about  $1.0 \text{ \AA}$  while using exact configuration of  $C_{60}F_{48}$  would make a maximum deviation of  $0.538 \text{ \AA}$  from our symmetric carbon cage. This amount of changes is not expected to be seen by STM. To reproduce exact experimental result we would require more details about the experimental tip, the substrate and possible orientations of  $C_{60}F_{48}$  on the substrate.

# Interpreting NC-AFM images of Si(111)-(7×7) surface

---

In Chapter 5, we reported simulated NC-AFM images of the assembly of C<sub>60</sub> and isolated C<sub>60</sub> molecule using the theoretical model detailed in Section 4.5. The results for the assembly of C<sub>60</sub> matches with experiment and for isolated C<sub>60</sub> we found similar pattern as seen in experiment. In this Chapter we shall report the application of the same model for another systems, Si(111)-(7×7) reconstruction. We discuss the contributions of different layers of Si atom to the triangular shaped features that are observed both in experiment and in simulation. The work presented in this chapter was done in collaboration with the group of Prof Philip Moriarty and the results were published in Beilstein Journal of Nanotechnology **7**, 937–945 (2016) [104].

### 7.1 The Si(111)-(7×7) reconstructed surface

The (7×7) reconstruction of Si(111), discovered through low-energy electron diffraction by Schlier and Farnsworth in 1959 [105], is one of the most com-

## Interpreting NC-AFM images of Si(111)-(7×7) surface

---

plex and widely studied surfaces. An adatom model was suggested by Binnig *et al.* [20] in 1983 while reporting the first real space image of the surface observed using STM. Later the dimer adatom stacking-fault (DAS) model for Si(111)-(7×7) reconstructed surface was proposed by Takayanagi [106] and backed by *ab initio* calculation [107] in 1992, which is now commonly accepted as the true structure of the surface. The bottom layer of the three layers of the reconstructed surface is the stacking fault layer, which distinguishes one side of the unit cell from the other. Atoms in this layer are also known as backbonding atoms. The top layer contains twelve adatoms, whereas the middle layer is the dimer layer. There are six atoms in the dimer layer which are also known as rest atoms. Each adatom in the Si(111)-(7×7) reconstruction is bounded to three silicon atoms within the stacking fault layer by covalent bonds formed by  $sp^3$  hybridization. A ball and stick model of the unit cell is shown in Figure 7.1.

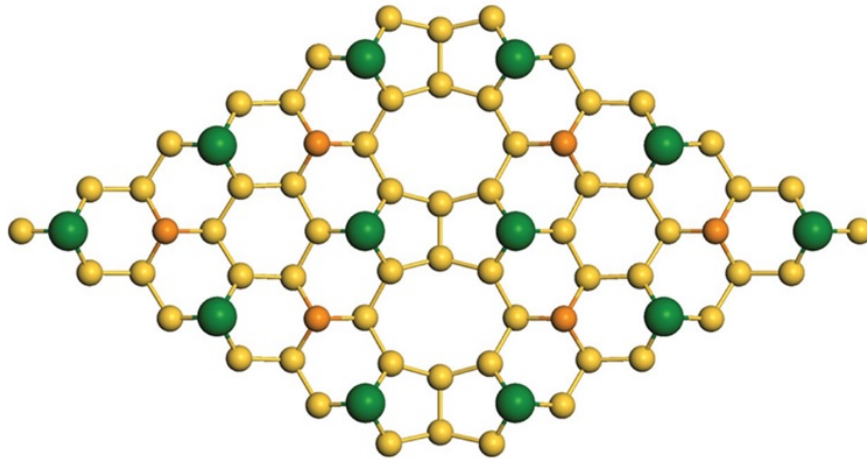


**Figure 7.1:** Ball and stick model of the Si(111)-7×7 unit cell with adatoms highlighted in green and rest atoms highlighted in orange [108].

The complexity and stability of the Si(111)-7×7 surface made it a surface of interest to many scientists. A very recent study of the surface reported a very clear triangular symmetry for the atoms [108] (Figure 7.2). The report also shows that the symmetry changes between the faulted and unfaulted half of the unit cell. The features cannot arise from the orbital structure of the atoms because of the nature of the dangling bond structure of the

## Interpreting NC-AFM images of Si(111)-(7×7) surface

---

silicon adatom. The symmetry of the features also contradicts the idea. Rather it suggests that the contrast could only arise from the backbonding symmetry of the surface adatoms. However, no modelling of the system has been performed in order to understand the precise origin of the contrast. The successful application of mechanical L-J model for  $C_{60}$  assembly and individual  $C_{60}$  molecule inspired us to apply the same model for the Si(111)-7×7 surface. Our study shows that the experimentally-observed triangular features arise from exploration of the asymmetric potential created due to the positioning of the surrounding atoms by a flexible tip without considering the detailed electronic structure of the surface.

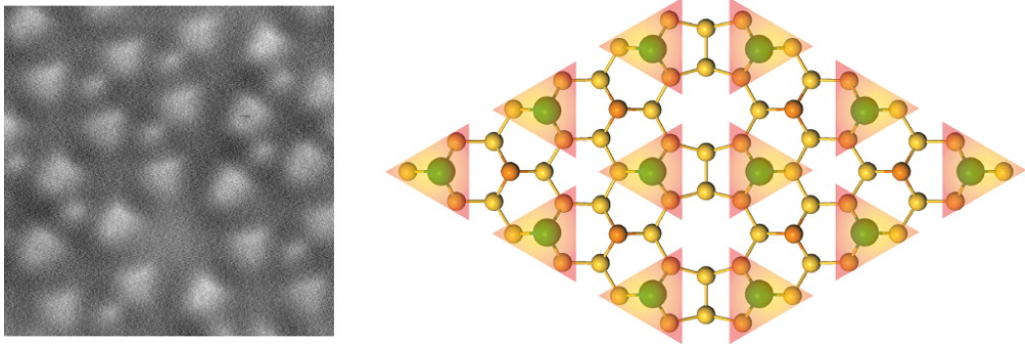


**Figure 7.2:** Subatomic feature on Si(111)-(7×7) surface observed during NC-AFM imaging operated in a low-temperature cryostat cooled to approximately 78 K using liquid nitrogen in ultrahigh vacuum. Figure taken from reference [108].

In our study to model the Si(111)-7×7 surface we imported the relaxed geometry from previous density functional theory simulations performed by Chiutu *et al.* [97].

## 7.2 L-J parameters

In order to interpret the experimental results, we simulated constant height NC-AFM images of the Si(111)-(7×7) reconstructed surface using the simple Lennard-Jones model described in Section 4.5 using a flexible CO tip. We

## Interpreting NC-AFM images of Si(111)-(7×7) surface

---

used the same L-J parameters as described by Hapala *et al.* [44] to model the functionalized tip, which are given in Table 7.1. We also used the same lateral stiffness  $k_{xy}$  of the interaction between tip base and the functionalized probe particle, which is  $0.5 \text{ Nm}^{-1}$ . We acquired the simulation data by scanning the sample laterally with a step of  $\Delta x, \Delta y = 0.1 \text{ \AA}$ . At each lateral position, we placed the tip base at an initial separation  $z_0 = 15 \text{ \AA}$  from the surface molecule and approached the sample in steps of  $\Delta z = 0.05 \text{ \AA}$  until  $z = 6 \text{ \AA}$ , allowing the probe position to be relaxed at each step due to the combined force of the sample and tip base. From these data, constant force images are generated.

**Table 7.1:** Lennard-Jones parameters.

Atom/Particle	$\epsilon_\alpha$ (meV)	$r_\alpha$ ( $\text{\AA}$ )
Tip base	1000	2.000
O	9.106	1.661
Si	25.489	1.900

During the force field calculations the positions of all the atoms in the surface slab were kept fixed. We note that more sophisticated versions of the probe-particle model also incorporate the effect of electrostatics via introduction of the Hartree potential, which has been shown to have important consequences for the imaging of certain classes of molecules [46]. In our simulations the effect of the Hartree potential is not included, primarily as electrostatic forces are not expected to result in significant differences in contrast due to the small variation in electrostatic force over the different atoms of the Si(111)-7×7 unit cell [109].

### 7.3 Origin of triangular contrast

Our simulation reproduces the striking subatomic features on Si(111)-(7×7) reconstructed surfaces (Figure 7.3) seen in experiment [108, 110, 111] (Fig-

## Interpreting NC-AFM images of Si(111)-(7×7) surface

---

ure 7.2). It is clear from the simulated images that as the tip moves closer to the surface, the features become more and more apparent. In the following we shall compare the outcome of the simulation with the experimental images in more detail to understand the possible origin of the triangular shapes in the Si(111)-(7×7) reconstructed surface.

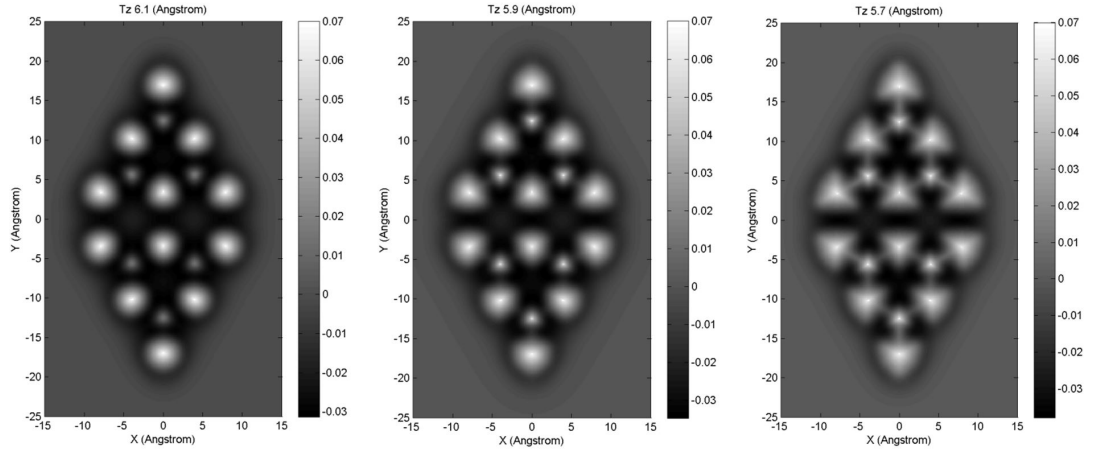


**Figure 7.3:** Subatomic feature on Si(111)-(7×7) surface observed by mechanical AFM model at different tip-sample separation.

In Figure 7.4 we show how the contrast in the simulated images evolve with the decrease of tip-sample distance. We compare the experimental constant height frequency shift,  $\Delta f$  images and with the simulated constant height  $\Delta f$  images using two different tip apices namely a flexible, and a very rigid tip apex. Simulated images have been selected from full data sets to illustrate the evolution of the contrast best. The  $\Delta f$  images were simulated with with an oscillation amplitude of 1.0Å. In all three sets of images when the tip is far from the surface (second row from top) the adatoms of the surface appear as attractive features which is expected from Lennard-Jones interactions. As the tip approaches to the surface, the contrast changes from dark to bright (third row from top) indicating repulsive features for the adatoms of the surface. Further into the repulsive regime (second row from bottom), triangular adatoms and rest atoms are clearly observed experimentally, and these features are reproduced well in the simulations using

## Interpreting NC-AFM images of Si(111)-(7×7) surface

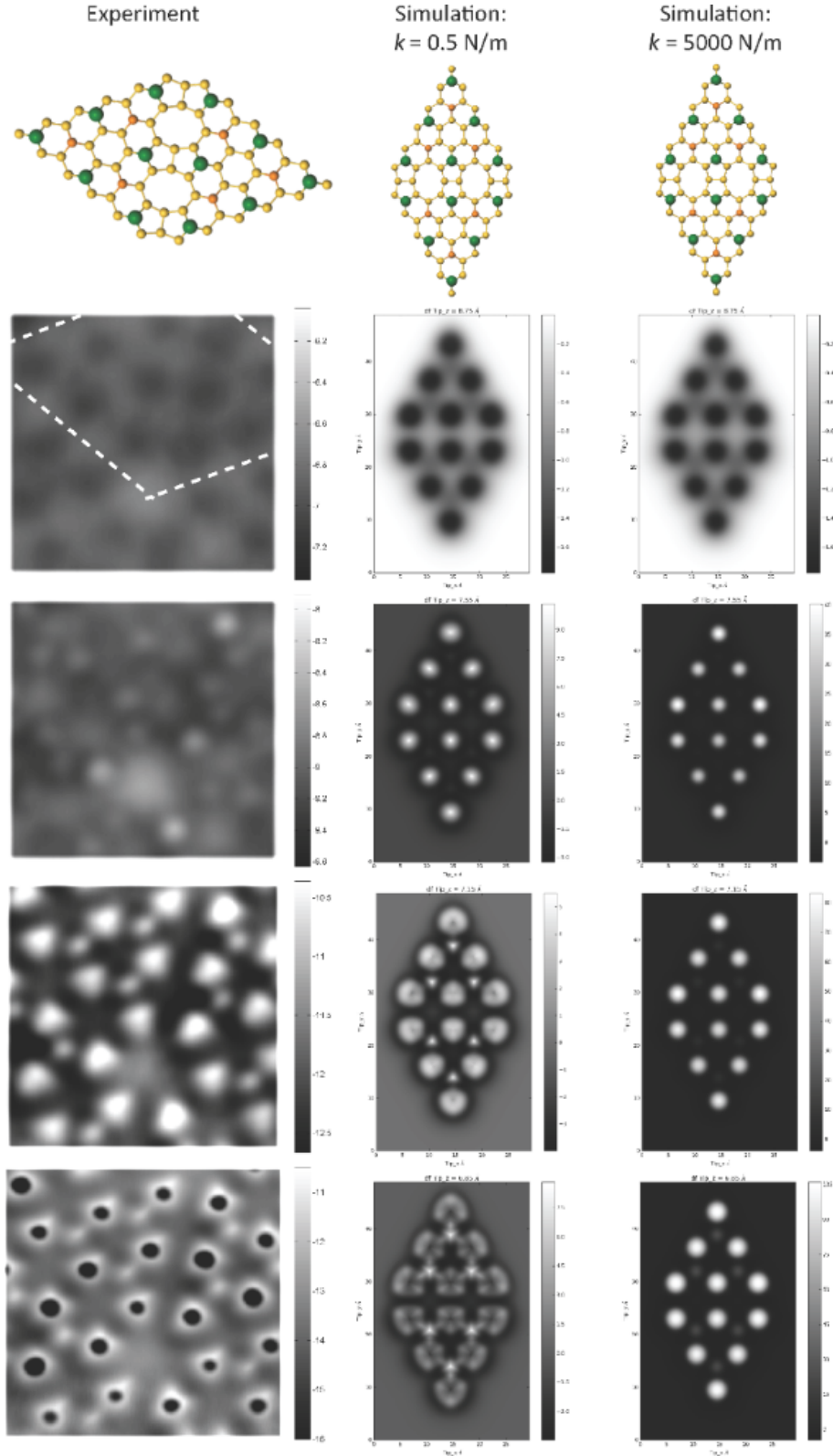


**Figure 7.4:** Experimental constant height  $\Delta f$  images at decreasing tip-sample separation (left column). Simulated images over a Si(111)-7×7 unit cell using a flexible tip with stiffness  $k_{xy} = 0.5 \text{ Nm}^{-1}$  (middle column) and  $k_{xy} = 5000 \text{ Nm}^{-1}$  (right column). At close approach with  $k_{xy} = 0.5 \text{ Nm}^{-1}$ , triangular adatoms and rest adatoms become apparent, similar to the experimental images. Simulated tip heights: (top to bottom) 8.75 Å, 7.55 Å, 7.15 Å, 6.85 Å.

## Interpreting NC-AFM images of Si(111)-(7×7) surface

the flexible tip ( $k_{xy} = 0.5 \text{ Nm}^{-1}$ ). Experimentally, at very close approach, dark depressions are observed in the centre of the adatoms indicating the onset of strong attractive interaction. The origin of this could be because of the change in the tip state due to the strong tip-sample repulsive forces or some modification of the chemical reactivity of the tip due to mechanical deformation. Surprisingly, similar features are reproduced in simulations using the flexible tip even though the Lennard-Jones potential does not take into account chemical interactions, or changes in the chemical reactivity of the tip. However this change in contrast is not observed with a rigid tip (right column of Figure 7.4). Since during the simulation no boundary conditions were used and the unit cell was finite, non-physical asymmetric distortions in the atoms at the edge of the unit cell were observed. Despite this, the reproduction of the experimentally observed features in the simulation using a flexible tip make it essential to consider the tip flexibility in interpreting contrast obtained in the repulsive regime during experiments using functionalized tips.

In order to understand the contribution of atoms in different layers of the Si(111)-(7×7) reconstructed surface to the observed contrast, we perform simulation using three toy systems i) adatoms only, ii) adatoms with backbonding atoms only and iii) adatoms with rest atoms only as shown in Figure 7.5. The value of the lateral stiffness parameter,  $k_{xy}$ , that is used in these simulations is  $0.5 \text{ Nm}^{-1}$ , in line with previous work presented in Chapter 5. Comparison of simulated images from the first two toy models (left and middle column of the Figure 7.5) shows that when only adatoms are considered they appear as uniform spheres at all heights, but when backbonding atoms are added to the adatoms they evolve from spherical to triangular contrast with close approach of the tip. Interestingly, for the third model when only the adatoms and rest atoms are considered (right column) the rest atoms appear clearly triangular, and the adatoms also have a triangular symmetry, despite the lack of atoms in the backbonding positions. However, the contrast inversion in the centre of the adatoms is observed

# Interpreting NC-AFM images of Si(111)-(7×7) surface

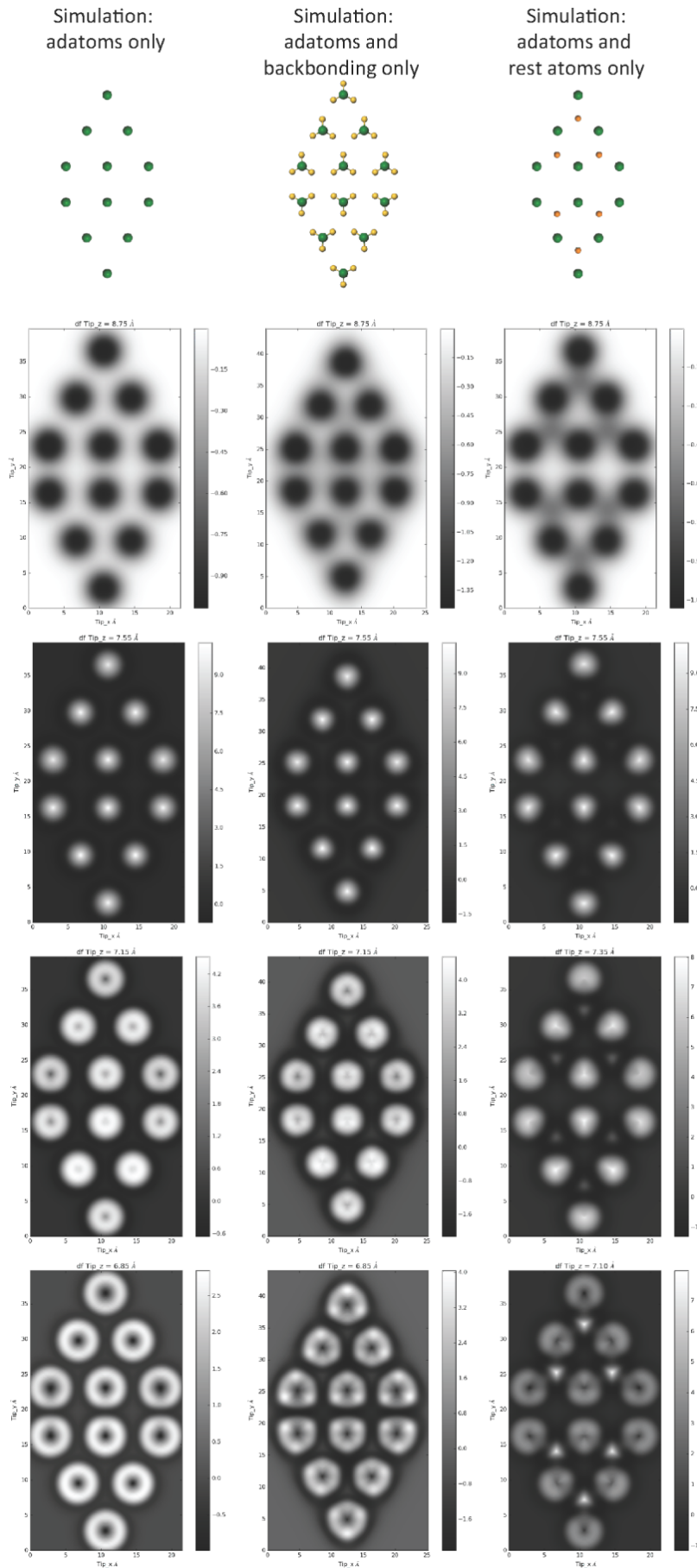


**Figure 7.5:** Simulated constant height frequency shift images at decreasing tip-sample separation, over a Si(111)-7×7 unit cell containing (left column) only the upper adatoms, (middle column) only the adatoms and their backbonding atoms and (right column) the adatoms and rest atoms without backbonding atoms.

in all three cases when the tip-sample separation is very small. The effect of the different elements of the surface slab illustrates how the appearance of the atoms is shaped due to the potential created by the entire surface. The simulations suggest that the experimentally-observed triangular shape of the adatoms results from the potential that results from a combination of the effect of the backbonding atoms, and presence of the rest atoms. The highest contribution to the contrast is from the backbonding atoms, while the rest atoms have least influence because of their lower height.

So far in most of the simulations we were using lateral stiffness  $k_{xy} = 0.5 \text{ Nm}^{-1}$ . To study the effect of the flexibility of the tip apex in the contrast and shape of atoms we compare the images from  $k_{xy} = 0.5 \text{ Nm}^{-1}$  simulations with a very low stiffness tip ( $k_{xy} = 0.1 \text{ Nm}^{-1}$ ), and a relatively rigid tip ( $k_{xy} = 5 \text{ Nm}^{-1}$ ). The outcomes of these results are summarised in Figure 7.6. Although for all stiffnesses we observe triangular shaped adatoms at small tip-sample separation, the extent and shape of the contrast inversion in the centre of the adatoms is directly affected by the change in lateral stiffness. The simulations with stiffnesss around  $k_{xy} = 0.5 \text{ Nm}^{-1}$  best reproduce the experimental contrast.

## 7.4 Conclusions

Using the simple L-J potentials and a flexible tip model we have successfully modelled the sub-atomic contrast seen in AFM images of Si(111)-7×7 reconstructed surface. From our results we are able to show that sub-atomic contrast can arise as the result of a flexible tip exploring the asymmetric potential around an atom which may not be related to its electronic orbital configuration. The contribution from the other atoms (specially from the nearby atoms) that are present in the substrate can contribute to produce this kind of asymmetric potential. This is supported by our calculations in which we show the contributions of different parts of the Si(111)-7×7

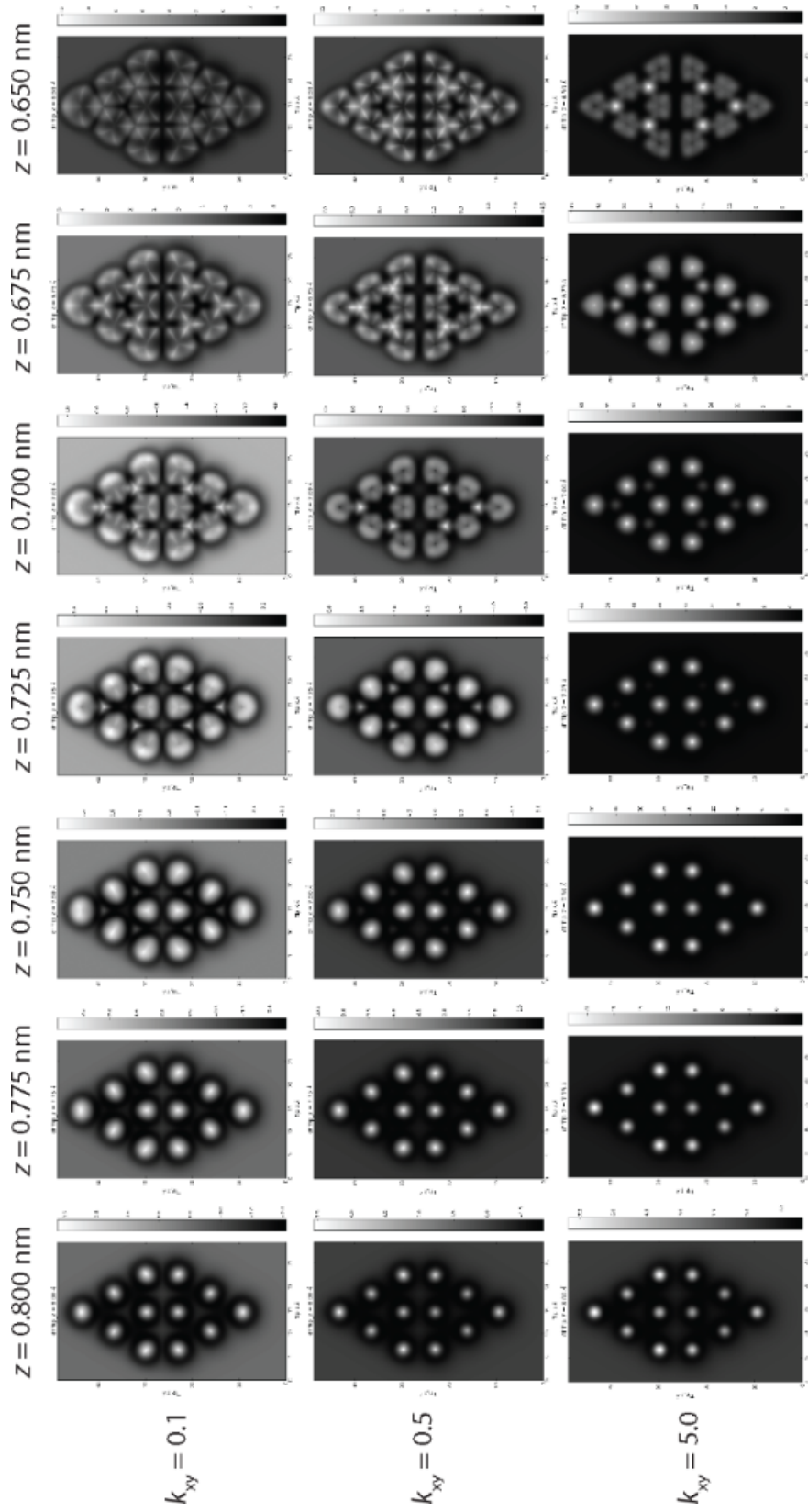


**Figure 7.6:** Simulated constant height frequency shift images over a Si(111)-7×7 unit cell at decreasing tip-sample separation for three different probe lateral stiffness,  $k_{xy}$ . The unit of  $k_{xy}$  is  $\text{Nm}^{-1}$ .

## **Interpreting NC-AFM images of Si(111)-(7×7) surface**

substrate to the sub-atomic contrast. Though our model does not take into account any electronic or chemical properties of the tip or sample it reproduces the contrast observed over the adatoms and rest atoms in a Si(111)-7×7 reconstructed surface. In summary the ability of simple L-J model to reproduce the AFM contrast for the assembly of C<sub>60</sub> and Si(111)-7×7 reconstructed surface suggests that attention must be given in interpreting apparent sub-atomic features. The possible contribution of the different parts of the system to the contrast must be examined with care before reaching to any conclusion.

# Interpreting ultrahigh resolution images of 2D bi-isonicotinic acid islands

---

Bi-isonicotinic acid (2,2-bipyridyl-4,4-dicarboxylic acid) is one of the most efficient dyes used in dye-semiconductor systems for solar cell applications [112–115]. Dye molecules in dye-sensitized solar cells absorb light in the visible region of the electromagnetic spectrum. As a result, the efficiency of the solar cell is increased [116, 117]. Through the ligand group formed by the bi-isonicotinic acid molecule, other technologically important dye molecules also anchor to model solar cell surfaces [118, 119]. Therefore many investigations have been made to understand the interaction of bi-isonicotinic acid with metallic and metallic oxide surfaces using different techniques [118–123]. Alexander Allen, of the Nottingham nanoscience group has studied the assembly of bi-isonicotinic acid molecules on Au(111) using atomic force microscopy to understand the structural properties of the molecule. We have simulated these images using the mechanical AFM model described in Section 4.5 and compared the result with experiment.

## Interpreting ultrahigh resolution images of 2D bi-isonicotinic acid islands

We also used density functional theory to optimize the structure of individual molecules and of small assemblies of bi-isonicotinic acid.

### 8.1 Structure of bi-isonicotinic acid molecule

Two isomers of bi-isonicotinic acid are found in nature: *cis* and *trans*. In the *cis* isomer of bi-isonicotinic acid both carboxyl groups (COOH) are attached to the pyridine rings are on the same side, whereas for the *trans* geometry they are on the opposite side of the C=C joining the pyridine rings. Both of the isomers have been studied to understand their properties [118,119,121]. In our case we have focused on the *trans*-bi-isonicotinic acid as the AFM image shown in Figure 8.1 suggests that the isomer present on Au(111) has the *trans* structure. The geometry of the molecule was first optimized using

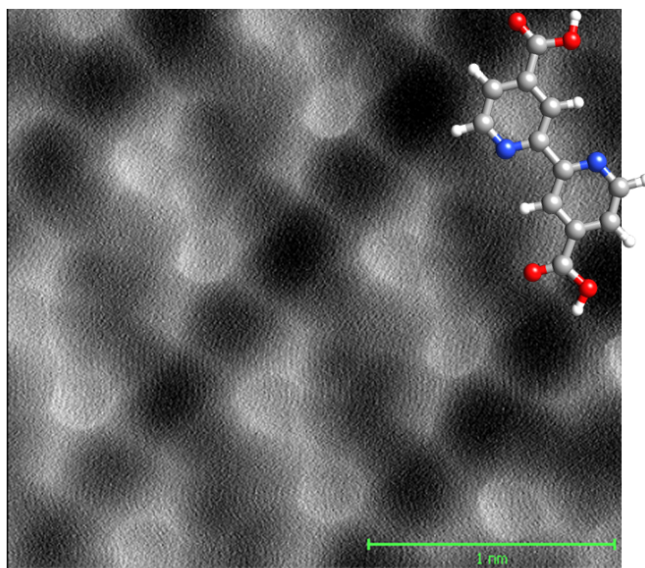


**Figure 8.1:** Constant height frequency shift AFM image of bi-isonicotinic acid assembly obtained by Alexander Allen in the group of Prof Philip Moriarty. Overlaid is the ball and stick model of a *trans*-bi-isonicotinic acid molecule. Small white spheres represent hydrogen, grey spheres represent carbon, blue spheres represent nitrogen, and red spheres represent oxygen.

DFT and then the relaxed structure is used to produce AFM images of the molecule, details of which will be given in the following sections. Figure 8.2

## Interpreting ultrahigh resolution images of 2D bi-isonicotinic acid islands

---

shows the ball and stick model of the DFT optimized geometry of the *trans* bi-isonicotinic acid molecule. In the rest of the chapter whenever we mention the bi-isonicotinic acid, we shall refer to the *trans* isomer of the molecule.

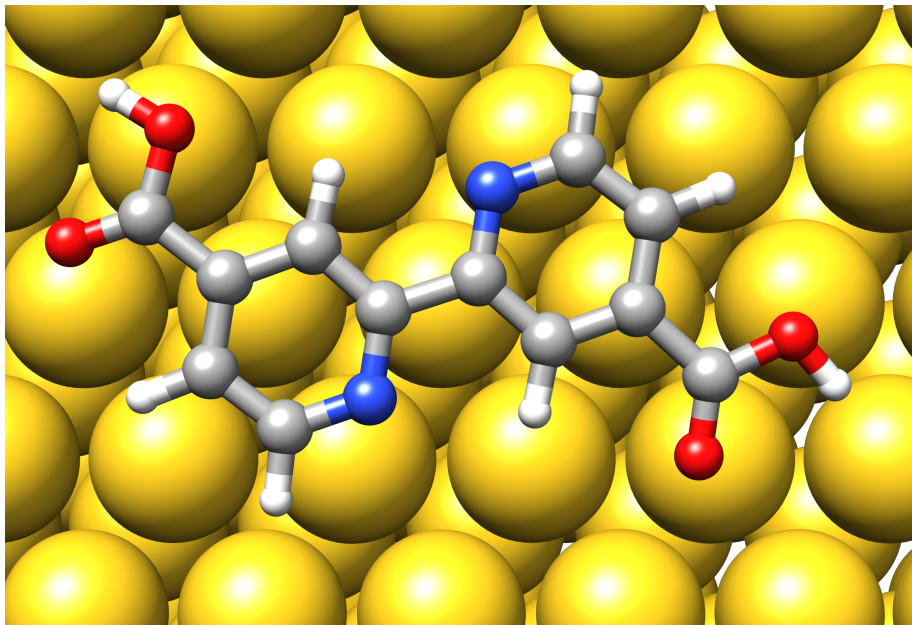


**Figure 8.2:** Ball and stick model of a *trans*-bi-isonicotinic acid molecule after optimizing the structure over a Au(111) slab using DFT. Small white spheres represent hydrogen, grey spheres represent carbon, blue spheres represent nitrogen, and red spheres represent oxygen. Atoms in Au(111) slab are shown as large golden spheres.

## 8.2 Geometry optimization using Kohn-Sham DFT

The process of finding the three-dimensional arrangement of atoms in a system that minimizes the energy is known as geometry optimization. Optimized structures often correspond to a substance as it is found in nature and the geometry of such a structure can be used in a variety of experimental and theoretical investigations in the fields of chemical structure, thermodynamics, chemical kinetics, spectroscopy and others. In our study

## Interpreting ultrahigh resolution images of 2D bi-isonicotinic acid islands

---

to find the optimized geometry of the island of bi-isonicotinic acid we implemented Kohn-Sham density functional theory. The DFT calculations were performed using the open source CP2K/Quickstep code [85–87] utilizing a hybrid Gaussian and augmented-plane-wave (GAPW) method [124]. Goedecker, Teter and Hutter pseudopotentials [125–127] and the Perdew Burke Ernzerhof generalized gradient approximation method [128] were used. To account for dispersion interactions we employed the Grimme DFT-D3 method [129, 130]. A double-zeta Gaussian basis set plus polarization (DZVP-MOLOPT) [131] was used with a force convergence criterion for geometry relaxation of  $0.005 \text{ eV}\text{\AA}^{-1}$ .

We divided the process of relaxation of geometry of the assembly of bi-isonicotinic acid in four parts. First, we relaxed the geometry of a single isolated bi-isonicotinic acid molecule. During this process no constraints were added and the atoms are allowed to move in any direction. A 400 Ry plane-wave energy cutoff was used. Then we relaxed the geometry of three layers of the Au(111) slab consisting a total of 162 Au atoms keeping bottom two layers of Au atoms fixed. The previously relaxed geometry of bi-isonicotinic acid was then placed over the relaxed geometry of the Au(111) slab which is then optimized with a plane-wave cutoff of 1000 Ry. Using the structure of bi-isonicotinic acid from the optimized bi-isonicotinic acid on Au(111) system a network of four bi-isonicotinic acid molecule is constructed. This was finally optimized to get the minimum energy configuration of the assembly of bi-isonicotinic acid. During this relaxation the unit cell is periodically repeated in both the  $X$  and  $Y$  directions while a  $30 \text{ \AA}$  gap was included in the  $Z$  direction. The adsorption energy of single bi-isonicotinic acid molecule on the Au(111) slab is found to be 1.242 a.u. When optimizing the geometry of the assembly of bi-isonicotinic acid the atoms within the molecules are only allowed to move in the  $xy$  plane keeping the  $z$  coordinates of all the atoms in the assembly fixed since we have taken the geometry of individual molecules from the geometry of bi-isonicotinic acid molecule relaxed on a Au(111) slab.

## Interpreting ultrahigh resolution images of 2D bi-isonicotinic acid islands

---

The procedure of generating the optimized structure of the bi-isonicotinic acid network starting from single isolated bi-isonicotinic acid molecule is shown in a flow chart in Figure 8.3. We show the change of total energy of the system during two relaxation processes in Figure 8.4. The top graph shows the total energy of the system containing bi-isonicotinic acid over the Au(111) slab while in the bottom graph we plotted the total energy of the network of four bi-isonicotinic acid molecule against the relaxation steps.

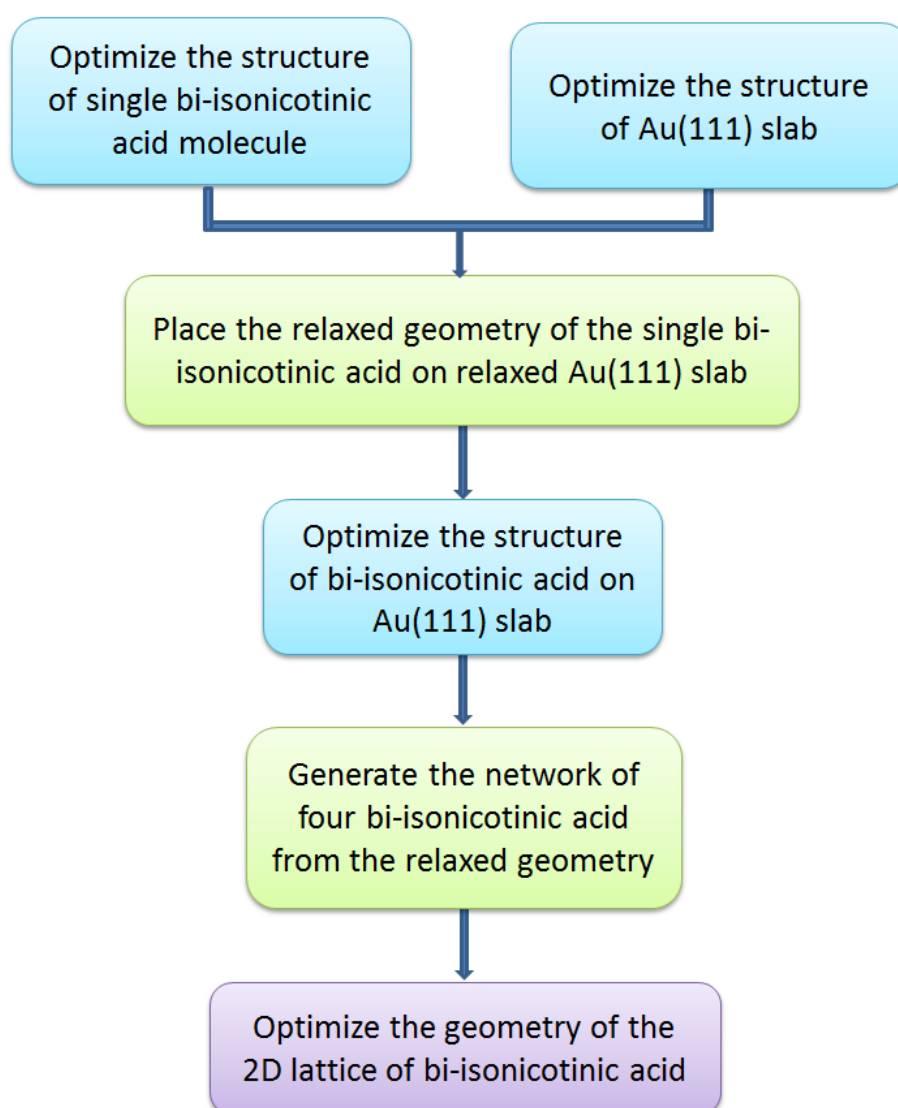


**Figure 8.3:** Procedure of optimizing the geometry of 2D lattice of bi-isonicotinic acid.

## Interpreting ultrahigh resolution images of 2D bi-isonicotinic acid islands

---

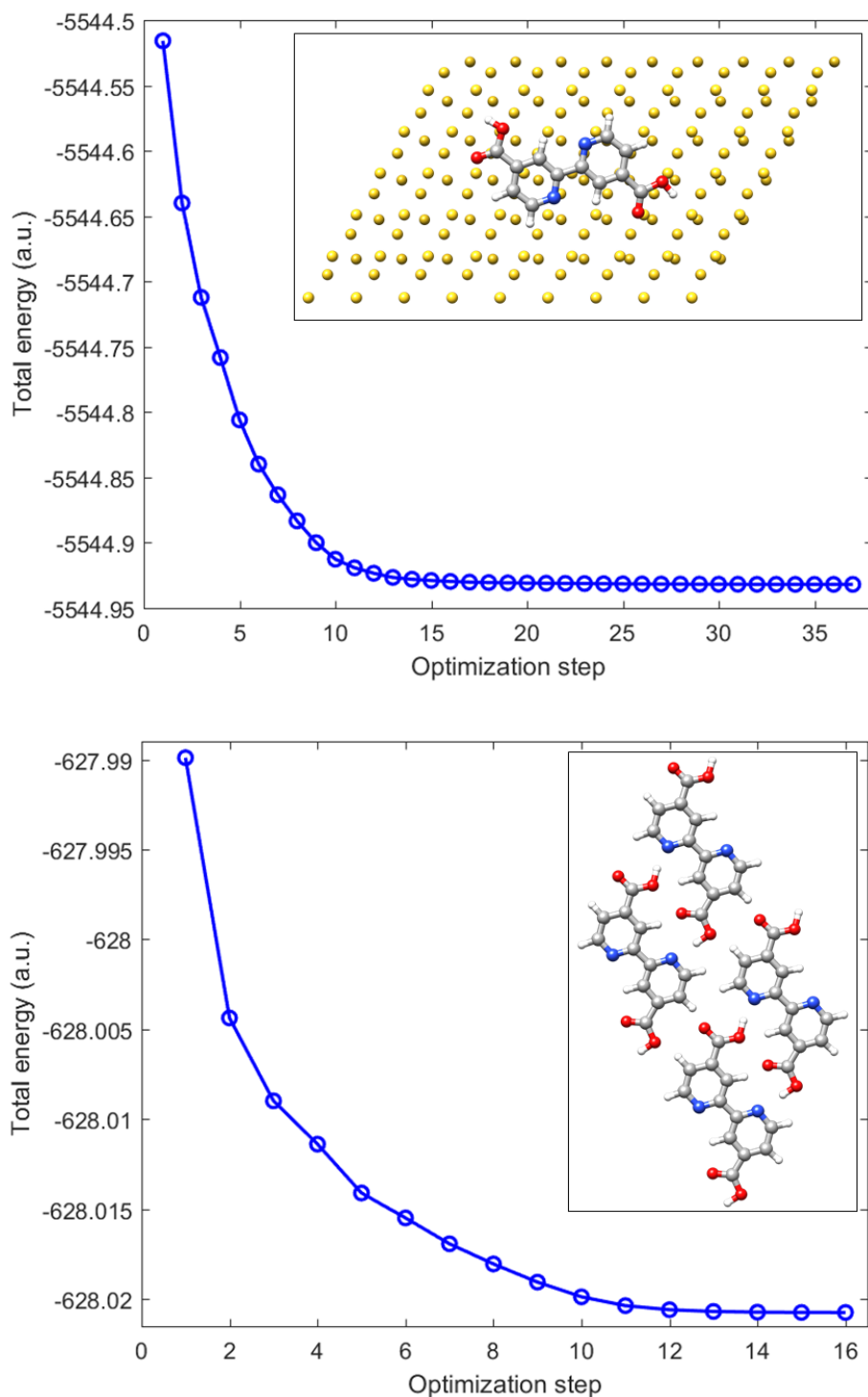


**Figure 8.4:** The total energy of the system during two relaxation process is plotted against the relaxation steps for system of bi-isonicotinic acid molecule on Au(111) slab (top) and an assembly of four bi-isonicotinic acid molecules. Insets are corresponding structures.

### 8.3 Generating simulated AFM images of bi-isonicotinic acid molecules

We acquire the simulated data of the sample using the same mechanical model (described in Section 4.5) which we used to construct NC-AFM images of the island of  $C_{60}$  and individual  $C_{60}$  (Chapter 5). We have used a CO-terminated flexible probe attached to the tip base to model the experimental CO-functionalized AFM tip. In our model the probe particle is represented by a single spherical atom i.e. to represent the CO-tip an oxygen atom is used as a probe instead of a CO molecule. The simulated data were acquired by scanning the surface laterally with a step  $\Delta x, \Delta y = 0.1 \text{ \AA}$ . At each lateral position  $(T_x, T_y)$  we placed the tip base at  $T_{z0} = 12 \text{ \AA}$  i.e.  $12 \text{ \AA}$  above from the sample. In this tip position the probe is placed in the minimum of the tip potential. Therefore at this tip base position the probe-sample separation is

$$\begin{aligned} P_{z0} &= T_{z0} - (r_{\alpha(\text{tip base})} + r_{\alpha(\text{probe base})}) \\ &= [12 - (2.0 + 1.661)] \text{ \AA} \\ &= 8.339 \text{ \AA} \end{aligned} \tag{8.1}$$

for a CO-terminated probe.

The tip approaches the sample in steps of  $\Delta T_z = 0.05 \text{ \AA}$  until  $T_z = 6.0 \text{ \AA}$  allowing the probe particle position to be relaxed at each step of the vertical approach in the combined force,  $\mathbf{F}_{\text{net}}$  of the sample and tip base (Eq. (4.49)). The vertical component,  $F_{\text{Surf}}(z)$ , (calculated using Eq. (4.46)) of the total force experienced by the probe due to all the atoms in the sample at the relaxed position is recorded for that particular tip position  $(T_x, T_y, T_z)$ , from which constant height force images are generated for that particular tip height,  $T_z$ . As the tip approaches the sample the above relation (Eq. (8.1)) between the tip base position and the probe position may not be valid

## Interpreting ultrahigh resolution images of 2D bi-isonicotinic acid islands

---

because of the relaxation of the probe position.

In our simulation we used the same Lennard-Jones parameters and lateral stiffness as in references [44, 46]. The parameters of the pairwise Lennard-Jones potentials are given in Table 8.1 and the value of lateral stiffness was  $k_{xy} = 0.5$  N/m. In Figure 8.5 we show simulated force images of single bi-isonicotinic acid molecule for two different tip positions,  $T_z$ . The value of  $T_z$  corresponds to the tip base position during the simulation i.e. the perpendicular distance between the tip base and the plane of the sample. The structure of the molecule is taken from the optimized geometry of the molecule over the Au(111) slab which is shown in Figure 8.2. From the images, the internal atomic structure of the bi-isonicotinic acid molecule can be observed clearly.

**Table 8.1:** Lennard-Jones parameters used to simulate AFM images of the bi-isonicotinic acid molecules.

Atom/Particle	$\epsilon_\alpha$ (meV)	$r_\alpha$ (Å)
H	0.680	1.487
C	3.729	1.908
N	9.106	1.824
O	9.106	1.661
Tip apex	1000	2.000

## 8.4 Simulating AFM images of 2D bi-isonicotinic acid lattices

In Figure 8.6 we show the structure of the assembly of bi-isonicotinic acid molecules before and after geometry optimization. The structure of the assembly was optimized following the procedure described in Section 8.2. Theoretical AFM force images of the relaxed structure of the island of bi-

## Interpreting ultrahigh resolution images of 2D bi-isonicotinic acid islands

---

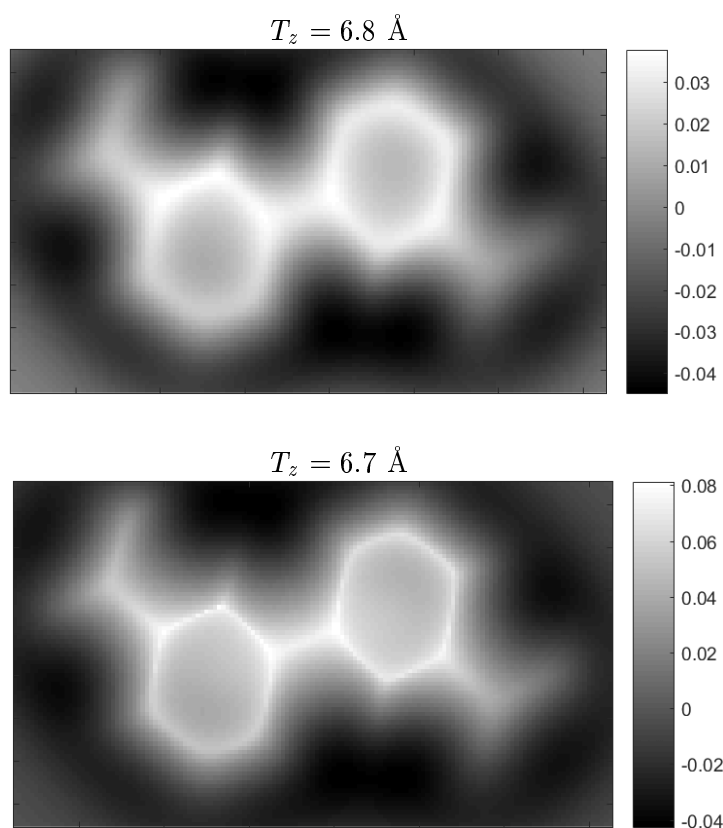


**Figure 8.5:** Simulated force images of single bi-isonicotinic acid molecule at different tip-sample separation,  $T_z$ . The colour scale shown in nN.

isonicotinic acid molecules are obtained using the mechanical AFM model based on the Lennard-Jones potential as we did for a single bi-isonicotinic acid molecule (Section 8.3). The simulated AFM images (which are shown in Figure 8.7) reveal a bond-like feature between the bi-isonicotinic acid molecules at the  $\text{N}\cdots\text{H}-\text{O}$  junction at small tip-sample separations ( $T_z = 6.7 \text{ \AA}$ ) while in the  $\text{C}=\text{O}\cdots\text{H}$  junction hardly any intermolecular contrast is observed even at very small tip-sample separation. However, the experimental frequency shift NC-AFM image (obtained by Alexander Allen at the University of Nottingham) reveals intermolecular contrast in both the  $\text{N}\cdots\text{H}-\text{O}$  and  $\text{C}=\text{O}\cdots\text{H}$  junctions (Figure 8.1).

Overlaying the structure of the bi-isonicotinic acid molecule on the AFM image (Figure 8.8) show that the molecules are aligned in a way that the  $\text{C}=\text{O}$  unit of one molecule faces the  $\text{H}-\text{C}$  unit of the other molecule while the DFT calculation suggests that the  $\text{N}\cdots\text{H}-\text{O}$  junction is favourable

## Interpreting ultrahigh resolution images of 2D bi-isonicotinic acid islands

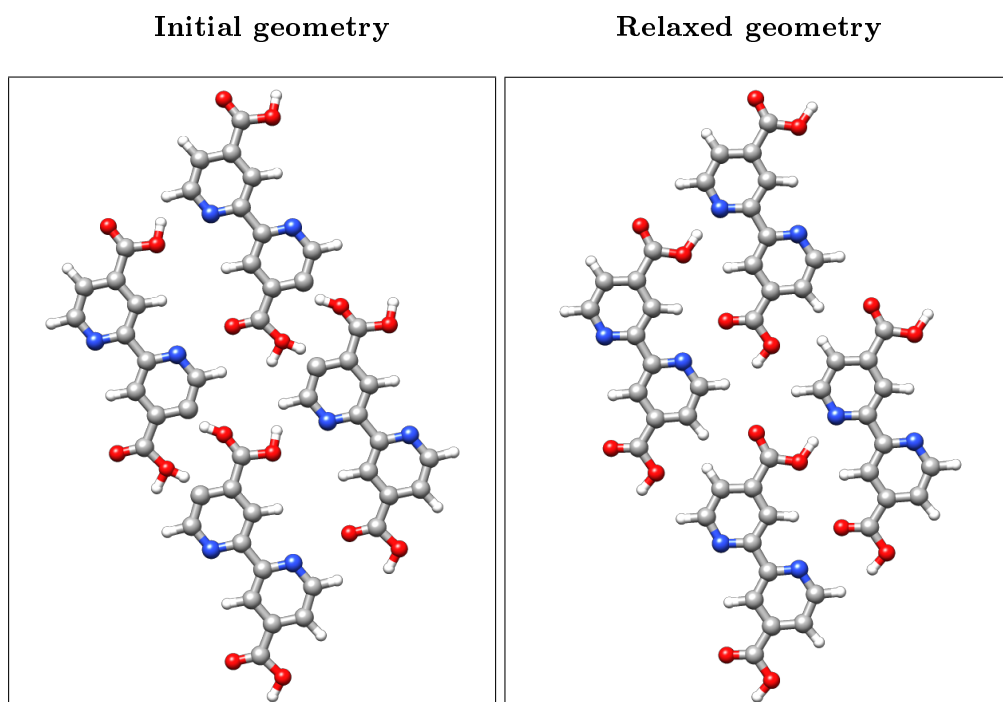


**Figure 8.6:** Ball and stick model of the assembly of four bi-isonicotinic acid molecule before (left) and after (right) relaxation (H in white, C in grey, N in blue and O in red).

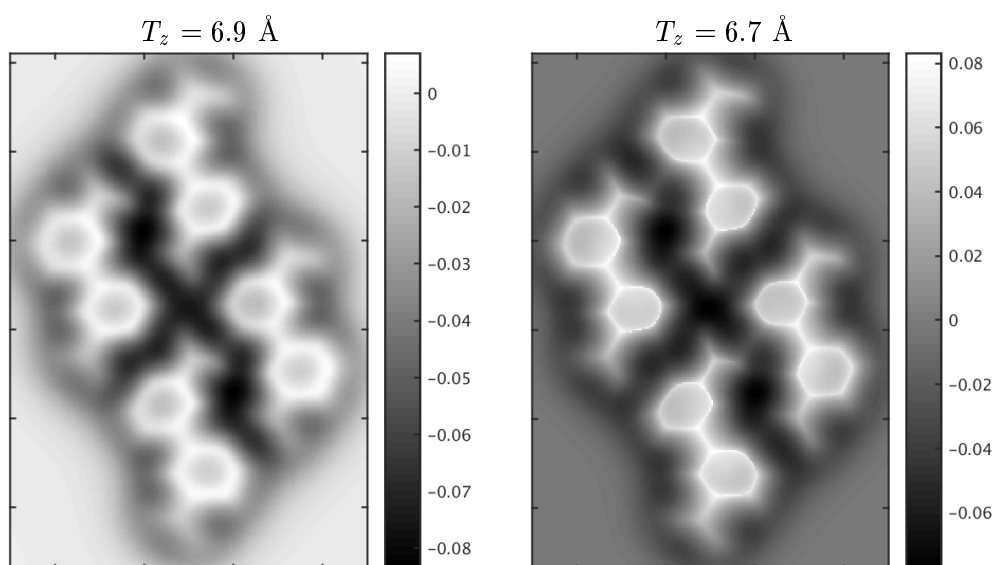


**Figure 8.7:** Simulated force images of the assembly of bi-isonicotinic acid molecules at different tip-sample separation,  $T_z$ . The relaxed geometry shown in Figure 8.6 is used in producing these AFM images. The colour scale shown in nN.

## Interpreting ultrahigh resolution images of 2D bi-isonicotinic acid islands

---

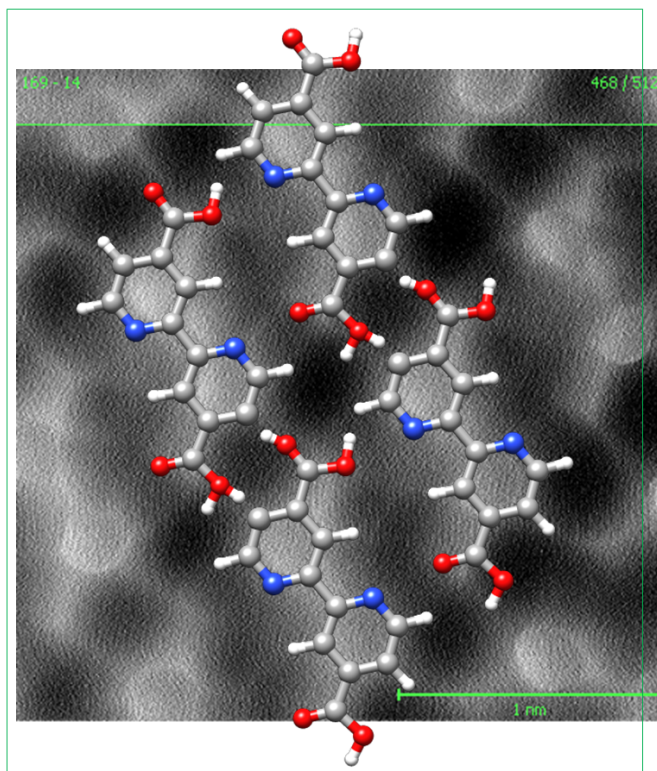


**Figure 8.8:** Overlay of the model of bi-isonicotinic acid molecule on the AFM image shown in Figure 8.1.

over the  $C=O \cdots H$  junction in the assembly of bi-isonicotinic acid molecule (Figure 8.6). In principle the DFT calculations are very close to exact, but practically it also involves many approximations and outcomes of the calculations greatly depend on the initial choice of the structure and boundary conditions. To study the structure of the assembly of bi-isonicotinic acid molecules further we moved the bottom two molecules of the relaxed structure shown in Figure 8.6 so the molecules are aligned facing  $C=O$  unit of one molecule to the  $H-C$  unit of the other keeping the  $N \cdots H-O$  junction same as in relaxed structure. The new structure is shown in Figure 8.9 (labelled as **Initial 01**) which is again optimized. We repeated the procedure two more times and the optimized structure of the bi-isonicotinic acid network obtained at the end of the relaxation is shown in Figure 8.9 (**Relaxed 03**). In this optimized assembly, not only are the  $C=O$  and  $H-C$  units of the neighbouring molecules are facing each other but they have the same  $N \cdots H-O$  junction length as found after first relaxation.

## Interpreting ultrahigh resolution images of 2D bi-isonicotinic acid islands

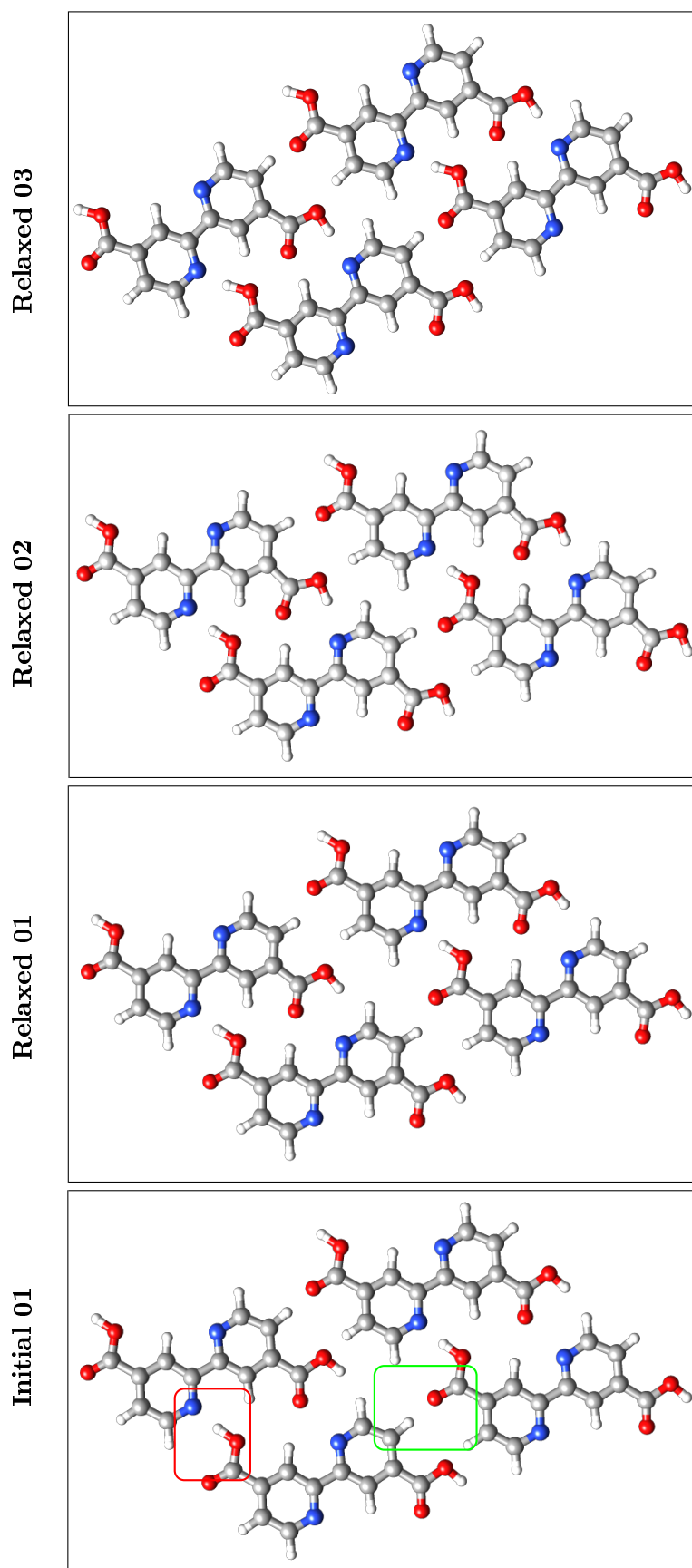


**Figure 8.9:** Ball and stick model of the assembly of bi-isonicotinic acid molecules at the different stage of the geometry optimization. Red and green rectangles in the left image highlight the  $N\cdots H-O$  and  $C=O\cdots H$  junctions. Small white spheres represent hydrogen, grey spheres represent carbon, blue spheres represent nitrogen, and red spheres represent oxygen. Total energies (in a.u.) of the relaxed geometries are -628.128, -628.021, and -627.856 respectively.

## Interpreting ultrahigh resolution images of 2D bi-isonicotinic acid islands

---

The simulated AFM images of the assembly of bi-isonicotinic acid molecules obtained using the geometry shown in Figure 8.9 (**Relaxed 03**) are shown in Figure 8.10. In the images, we observe the intermolecular contrast both in  $N\cdots H-O$  and  $C=O\cdots H$  junctions of the neighbouring molecules. The simulated AFM images shown in Figure 8.11 are obtained using the overlay structure shown in Figure 8.8. We observe similar contrasts in the two sets of images although the intermolecular feature is more apparent in the latter set of images. This is because of the spacing between the molecules in the two geometries that are used in simulating AFM images. The theoretical AFM images produced using overlay geometry of the assembly of bi-isonicotinic acid molecules match the experimental images almost exactly. However the AFM images produced from the relaxed geometry do not have the exactly same feature though they are very close to the experimental results. This indicates that we also need to consider other geometries of the assembly of bi-isonicotinic acid molecules for the DFT calculations with different spacing between the molecules in the assembly to achieve a very good match with the structure found in nature. The use of different potentials during the geometry optimization using DFT may also produce different results.

### 8.4.1 Effect of stiffness parameter in simulated AFM images

In our previous study of the assembly of  $C_{60}$  molecules, we have mostly used a large tip ( $C_{60}$  functionalized tip) to simulate the AFM images of the assembly while in the current study we are using a CO-terminated tip. Also the structure of the  $C_{60}$  island is different to that of the bi-isonicotinic acid molecule. The  $C_{60}$  molecule is large and spherical in shape while bi-isonicotinic acid is almost a planar molecule. Therefore it is important to study the effect of different parameters that are involved in simulating AFM images. In Figure 8.12 and Figure 8.13 we show two sets of simulated AFM images of the assembly of bi-isonicotinic acid produced using the

## Interpreting ultrahigh resolution images of 2D bi-isonicotinic acid islands

---

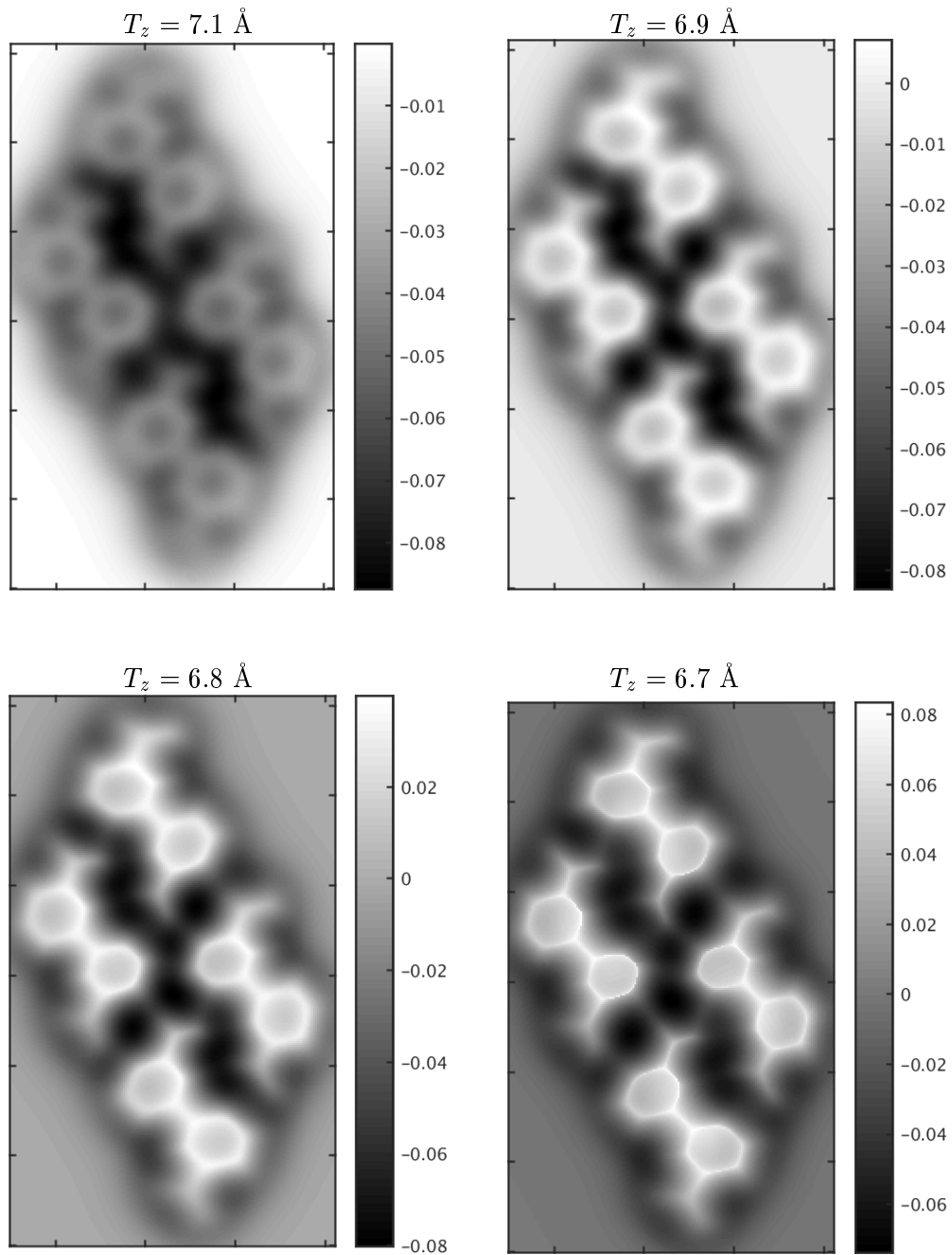


**Figure 8.10:** Simulated force images of the assembly of bi-isonicotinic acid molecules at different tip-sample separation,  $T_z$  obtained using the optimized geometry shown in Figure 8.9 (**Relaxed 03**). The colour scale shown in nN.

## Interpreting ultrahigh resolution images of 2D bi-isonicotinic acid islands

---

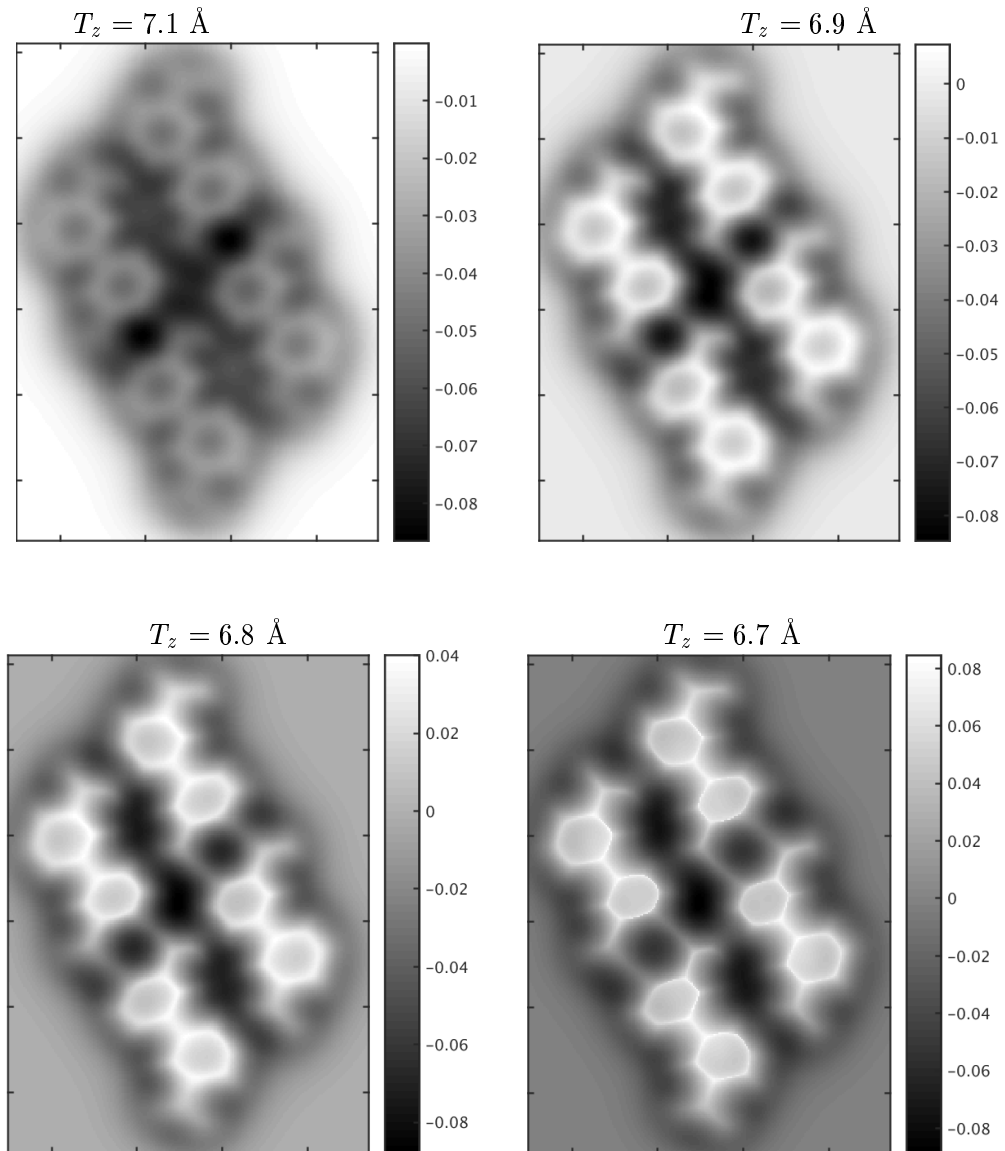


**Figure 8.11:** Simulated force images of the assembly of bi-isonicotinic acid molecules at different tip-sample separation,  $T_z$  obtained using the overlay geometry shown in Figure 8.8. The colour scale shown in nN.

optimized geometry shown in Figure 8.9 (**Relaxed 03**) for different tip-sample separation,  $T_z$  and stiffness parameter of the interaction between tip base and the functionalized probe particle,  $k_{xy}$ . From the images shown in Figure 8.12, we observe the variation of contrast in the constant height AFM images at a specific tip-sample separation  $T_z = 6.8 \text{ \AA}$  with the change of stiffness parameter,  $k_{xy}$ . This is because with a low value of  $k_{xy}$  the probe is more flexible compared to a high value to move around the tip base. When the tip approaches the sample, the force experienced by the

## Interpreting ultrahigh resolution images of 2D bi-isonicotinic acid islands

---

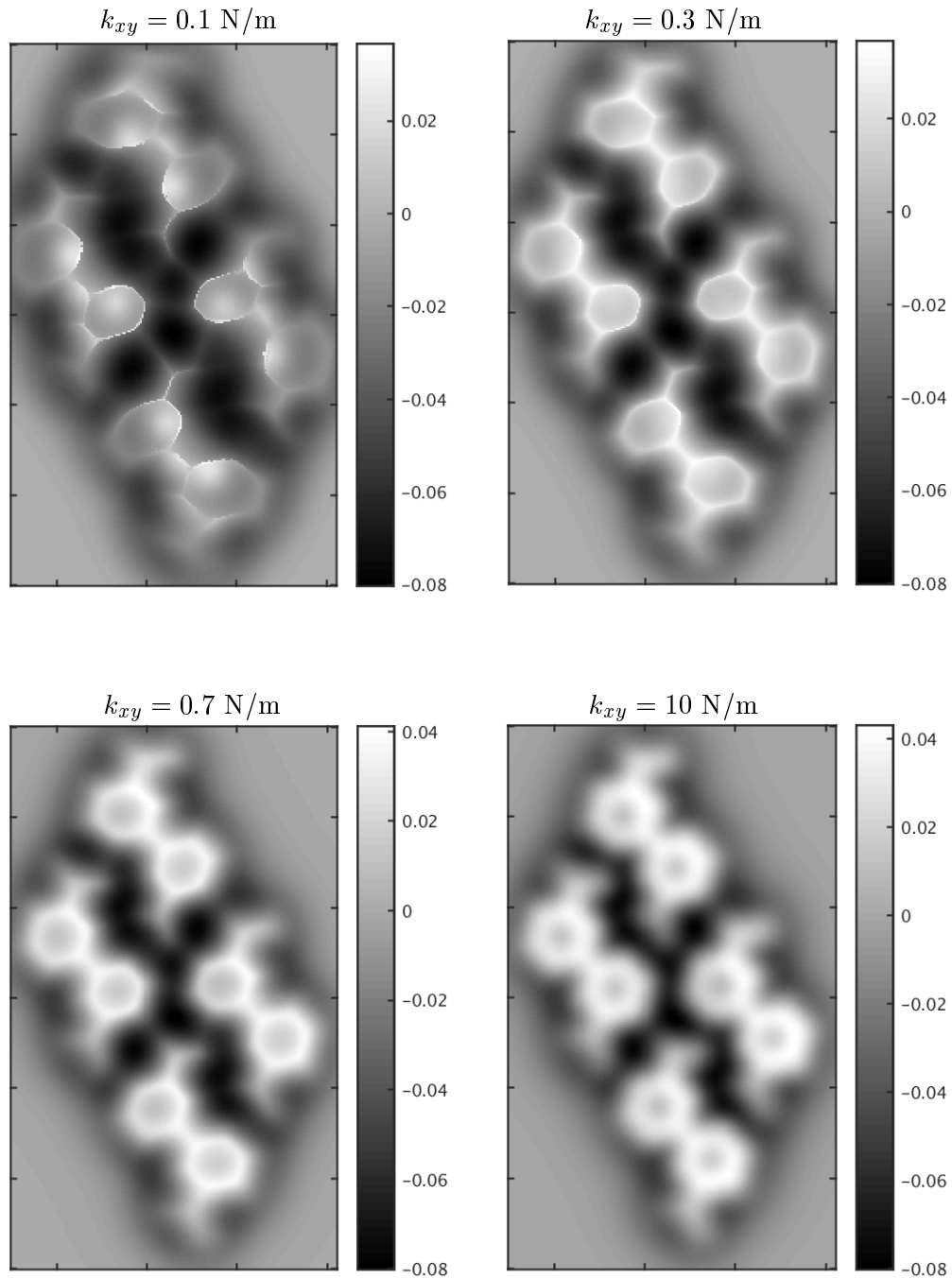


**Figure 8.12:** Simulated constant height AFM force images of the assembly of bi-isonicotinic acid molecules for tip-sample separation  $T_z = 6.8 \text{ \AA}$  with different stiffness parameter,  $k_{xy}$ . The colour scale shown in nN.

## Interpreting ultrahigh resolution images of 2D bi-isonicotinic acid islands

---

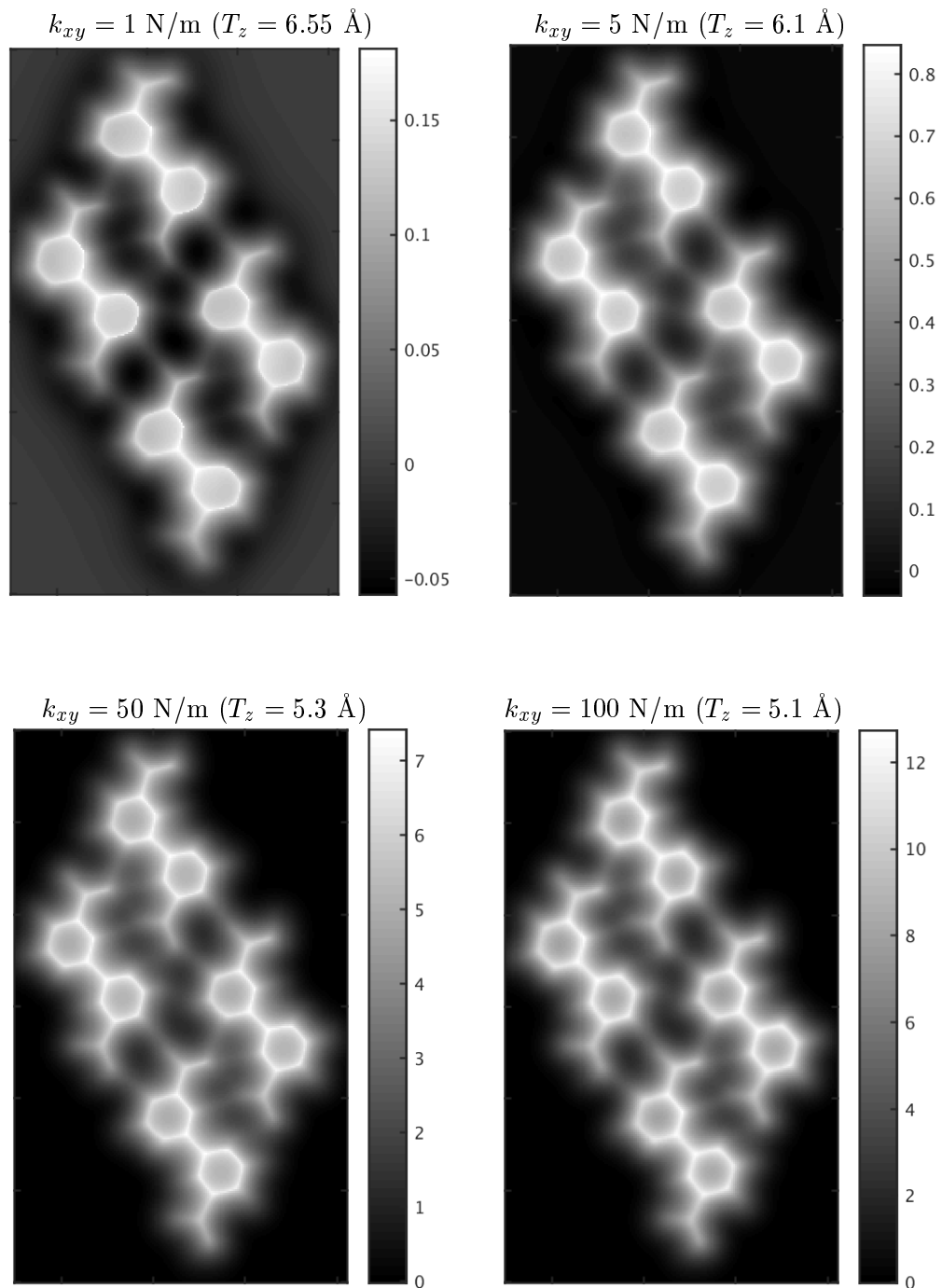


**Figure 8.13:** Simulated constant height AFM force images of the assembly of bi-isonicotinic acid molecules. All the images have similar contrast while both tip-sample separation,  $T_z$  and stiffness parameter,  $k_{xy}$  were varied. The colour scale shown in nN.

## Interpreting ultrahigh resolution images of 2D bi-isonicotinic acid islands

---

probe due to the atoms in the sample increases. Because of that, the probe bends during the minimization of the total energy to find a local minimum giving rise a sharp intermolecular contrast at  $T_z = 6.8 \text{ \AA}$ . However, as the value of  $k_{xy}$  increases, the tip become more rigid compared to the allowed value of  $k_{xy}$ . In this case we only see the intermolecular contrast when the tip is pushed very close to sample, which are shown in Figure 8.13. Similar dependency of the image contrast on the stiffness parameter,  $k_{xy}$  is also reported in the supplementary material of reference [44].

Figure 8.14 shows a comparison of simulated AFM image of 2D bi-isonicotinic acid lattice with the experimental result. In simulation, we are able to capture most of the features seen in experiment though some of the features are less apparent in theoretical images compare to experiment. The simulated image is obtained using the geometry shown in Figure 8.9 (**Relaxed 03**). We found the best match at  $T_z = 6.65 \text{ \AA}$ .

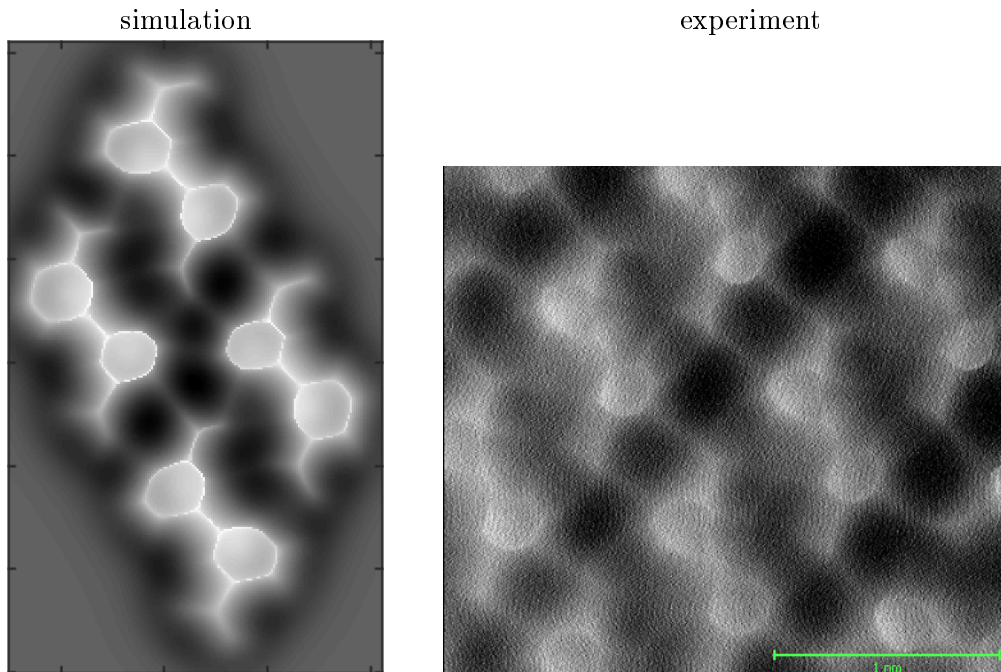


**Figure 8.14:** Comparison of simulated and experimental AFM images of 2D bi-isonicotinic acid lattice. Constant-height (at  $T_z = 6.65 \text{ \AA}$ ) simulated image is obtained using the geometry shown in Figure 8.9 (**Relaxed 03**).

## 8.5 Conclusion

We have studied the assembly of bi-isonicotinic acid using DFT and a simple mechanical AFM model. Our results on the theoretical AFM study using the DFT optimized geometry is able to reproduce most of the features as found in AFM experiment. The difference in the theoretical AFM images obtained using relaxed and overlay geometry of the assembly suggests that other variations of the geometry also need to be taken into consideration to have a even better match with the experimental result. If the geometry of the island of bi-isonicotinic acid molecules is optimized including the Au(111) surfaces and then the AFM images are simulated using that geometry, it may produce a better match with the experiment. However, this will consume much time, which could be done in future. All the simulations, both DFT and AFM, that are reported in this chapter are performed using High Performance Computing (HPC) Facility of the University of Nottingham. We used UCSF Chimera package [132] to produce the ball and stick images of the bi-isonicotinic acid molecule and its assemblies.

## Chapter 9

---

### Summary

---

In this thesis, we have shown that experimentally observed intermolecular features, which are sometimes claimed to be the intermolecular hydrogen bonds, can be simulated by using a simple mechanical AFM model based on the pairwise Lennard-Jones potential. In our study we have primarily focused on the assembly of  $C_{60}$  molecules which can not possibly have any hydrogen bond, as the  $C_{60}$  molecule is composed of carbon atoms only. The assembly is not only non-planar but also stabilized by weak van der Waals forces. Using a functionalized flexible  $C_{60}$  probe, we produced theoretical AFM images of the assembly of  $C_{60}$  molecules which clearly show the intermolecular contrast between the  $C_{60}$  molecules in the sample. The same feature was also confirmed experimentally by the group of Prof Philip Moriarty, the University of Nottingham.

Our theoretical study suggests that the artifact can only be observed with a rightly functionalized tip which is soft enough to move on the sample from a high energy position to a local minima during the experiment. The feature can neither be observed with a rigid tip nor if the tip is too small in size to feel significant forces simultaneously from the neighbouring molecules or atoms when placed in between the molecules or atoms. This is confirmed

## Summary

---

by repeating the simulation with a flexible CO-terminated tip and a rigid  $C_{60}$ -functionalized tip. In none of the cases were any intermolecular features observed even if the tip is pushed very close to the sample. The bulk of this work has been published in the Rapid Communication section of Physical Review B [88].

We also investigated the assembly of  $C_{60}$  using EHMO theory, which takes into account the interactions between the orbitals and the MOs of the system. We used Gaussian type orbitals as a basis set. In this case we studied the system consisting of two  $C_{60}$  molecules separated by 10.2 Å as in the case of a  $C_{60}$  island. The molecules were imaged by a  $C_{60}$  terminated rigid tip and no intermolecular feature is observed even with a small tip-sample separation. The ability of the mechanical model to produce the intermolecular contrast in a non-planar, van der Waals-mediated fullerene system with a  $C_{60}$  terminated flexible tip highlights that artifactual intermolecular contrast is a key issue for ultrahigh resolution force microscopy.

In addition, we report the theoretical study of the intermolecular potential between the  $C_{60}$  molecules in different relative orientations, using the same analytical model based around the Lennard-Jones potentials. In this case, both the flexible tip and the sample were described atomically while previously the probe was approximated as large sphere to represent the  $C_{60}$  terminated tip. Comparing a variety of simulated images with the experimental results, we conclude that for appropriate choices of the Lennard-Jones parameters and of relative tip-sample orientation, the method would allow us to predict the form of the intra- and intermolecular potential that would be observed using dynamic atomic force microscopy. Our work regarding individual  $C_{60}$  molecules has been published in Nature Communications [89]. All the results from the study of the assembly of  $C_{60}$  and individual  $C_{60}$  molecules are presented in Chapter 5.

Chapter 6 introduced the STM imaging of the neutral  $C_{60}F_{48}$  molecule, with the MOs constructed using both modified HMO theory and EHMO

## Summary

---

theory. We produced the constant current images of the molecule using three different tip states, namely  $s$ ,  $p_x$ , and  $p_z$ . We find similar patterns on the simulated STM images though they do not match exactly with the experiment.

The results for the Si(111)-(7×7) reconstructed surface is presented in Chapter 7. Applying the mechanical L-J model we are not only able to reproduce the experimental results but also able to explain the origin of the triangular features observed experimentally. We show that the triangular features observed experimentally arise naturally from the exploration of an “asymmetric potential” by a flexible tip and do not require consideration of the detailed electronic structure of the surface. The asymmetric potential is generated by the local atomic environment i.e. the neighbouring atoms present in the sample (e.g. rest atoms). From the results we conclude that distinction must be made between what might be termed as “orbital” imaging, which explicitly images the orbitals of single atoms, and “subatomic” imaging, which can arise from a number of multi-atom effects. These results has been published in Beilstein Journal of Nanotechnology [104].

In Chapter 8 we reported the study of a planar system, the assembly of bi-isonicotinic acid molecules. The assembly of  $C_{60}$  molecules composed of large spherical  $C_{60}$  molecules and in the unit cell of reconstructed surface of Si(111)-(7×7) 90 Si atoms are laid in different layers while in bi-isonicotinic acid all the atoms have almost the same values for  $z$  coordinate. Moreover, the assembly of bi-isonicotinic acid molecules contains both  $N \cdots H-O$  and  $C=O \cdots H$  junctions i.e. the system is stabilized through hydrogen bonds. We showed that with an appropriate choice of the lateral stiffness parameter  $k_{xy}$  we are able to produce similar results as observed in experiment. The ability of the simple L-J model, which does not include any electronic description of the system, to produce intermolecular contrast in systems with and without hydrogen bond suggests that utmost care must be taken in interpreting high resolutions AFM images. In some cases, where hydrogen

## Summary

---

bonding is present in the system, the features may have contributions from both the real hydrogen bond and tip artifact. However, for other systems like the assembly of  $C_{60}$  molecules, the feature solely arises from the artifact of the tip flexibility.

The work presented here regarding  $C_{60}F_{48}$  and assembly of bi-isonicotinic acid molecules are only at the preliminary stage. With the availability of more experimental results they could be studied further and comparisons could be made. With the exact geometry of  $C_{60}F_{48}$  and taking into account of the isomers of the molecule,  $C_{60}F_{48}$  could be studied in future using DFT for more orientations. Also considering different complex tip states other than  $s$ ,  $p_x$ , and  $p_y$  may produce a better match with the experiment. For the assembly of bi-isonicotinic acid molecules, taking into account a variety of initial configurations of the assembly and including the Au(111) slab during the geometry optimization may produce better results.

In conclusion, the SPM models presented here to study the molecules on the surface have very good potential and can be developed further to study more complex systems. Which could be done by adding more interactions (e.g. Hartree potential) and taking into account the mechanical deformation of the sample in the tip-sample junction.

## Appendix A

---

# Metal phthalocyanine (MPcs)

---

Metal phthalocyanines (MPc, where M refers to the metal and Pc to the phthalocyanine ligand) are metallorganic molecules which have numerous potential applications in molecular electronics and as a catalyst. MPcs are intensively studied in the field of light-emitting diodes [133], organic field-effect transistor [134], spintronic devices [135] and organic photovoltaic cells [136]. Because of conformational flexibility, MPc molecules also have potential application as molecular switches and memories at the nanoscale [137, 138]. The unique and complex nature of MPc-metal surface interface [139] demands a detail theoretical study of the MPc molecule to understand the physical and chemical properties of the interface alongside experimental studies. The large size of MPc ( $C_{32}H_{18}N_8M$ ) makes it difficult to use standard *ab initio* methods [140]. As an alternative we used the mechanical Lennard-Jones method to study MPc (M = Fe, Co, Pb, Sn) molecules.

In Figure A.1 we show the ball and stick model and the experimental AFM image of Fe-phthalocyanines islands. The experiment was carried out by Alex Saywell in the Nottingham nanoscience group. The  $\Delta f$  (frequency shift) image (Figure A.1, right) resembles the structure of FePc, particularly

## Metal phthalocyanine (MPcs)

---

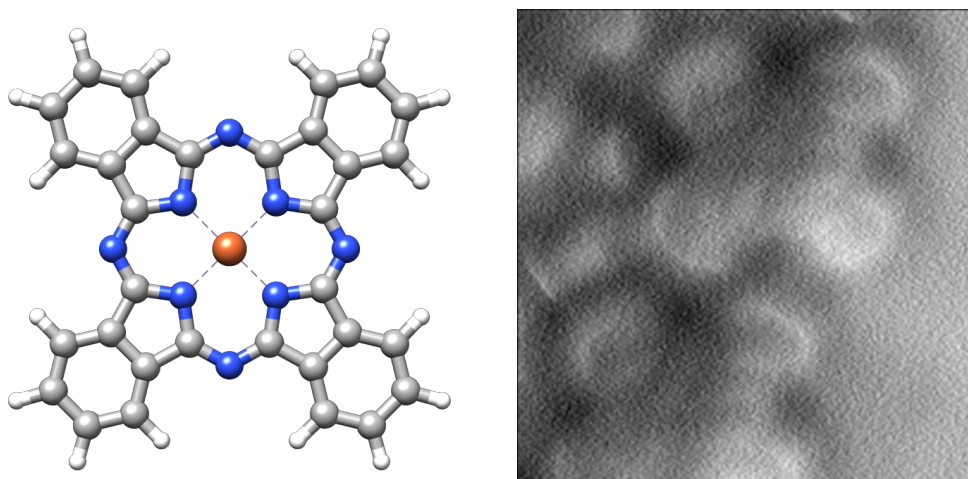


**Figure A.1:** Ball & stick model of FePc (Fe in rust, N in light blue, C in grey, H in white) and AFM image of FePc island as observed by Alex Saywell at the University of Nottingham.

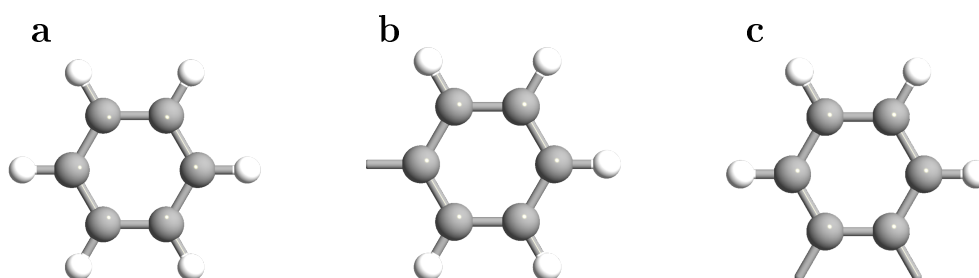


**Figure A.2:** Ball & stick model of a) benzene and b) & c) aryl groups. Aryl groups are derived from benzene by removing one or more hydrogen atoms from the ring. In the ball & stick images C is shown in grey and H is in white colour.

the four aryl rings of the molecule can be seen very clearly from the image. The aryl is a functional group derived from benzene, C<sub>6</sub>H<sub>6</sub> by removing one or more hydrogen atoms from the ring (Figure A.2). The four aryl rings in FePc are like the one shown in Figure A.2 c. From Figure A.3, where a stick model of FePc is superimposed on the  $\Delta f$  image of a FePc we observe that the centre of the FePc is not as visible as the four aryl rings. Comparing the AFM image with the simulated  $\Delta f$  images of an isolated FePc which are shown in Figure A.4 we see that the appearance and shape of four aryl rings becomes clearer as the tip approaches the molecule. Though the contrast at the centre of the molecule in the simulated image is completely opposite

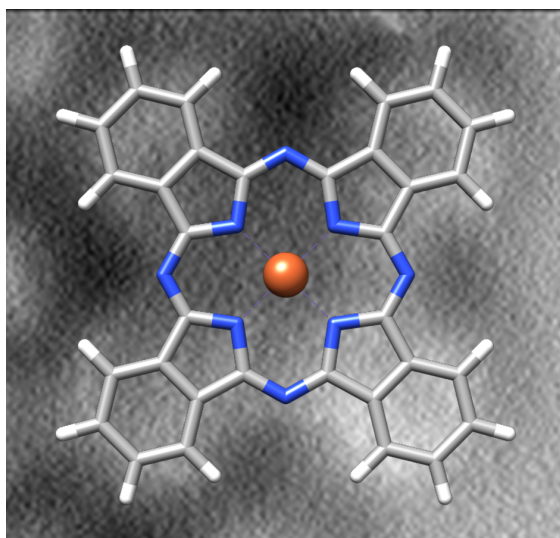


**Figure A.3:** The stick model of FePc superimposed on the  $\Delta f$  image of FePc obtained in experiment.

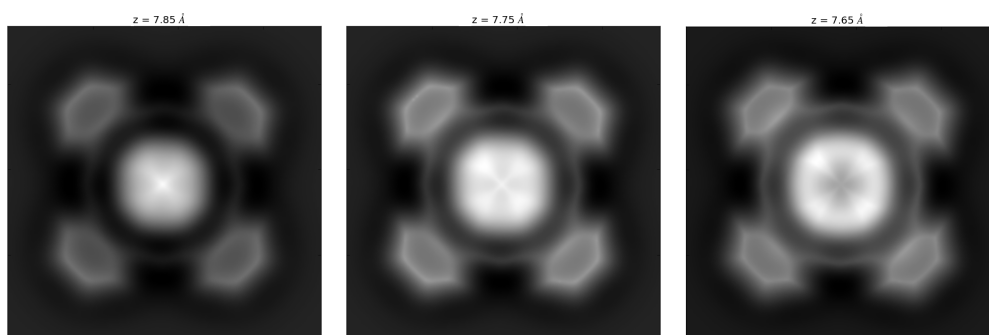


**Figure A.4:** Simulated AFM images of FePc using mechanical L-J model at different tip-sample separation.

to that of the experimental image. When we simulated the  $\Delta f$  images of phthalocyanine without Fe atom at the centre (Figure A.5), at large tip-sample separation they are similar to the AFM images of FePc. The central region again becomes brighter as the tip approaches the sample. The value of oscillation amplitude used during the simulation for the images shown in Figure A.4 and A.5 was  $1.0 \text{ \AA}$ . We have carried out simulation with other metal phthalocyanines (CoPc, NiPc, PbPc) and in all cases we have seen the similar contrasts in theoretical images which are not presented here. All these simulations were performed using a functionalized CO tip. The

## Metal phthalocyanine (MPcs)

---

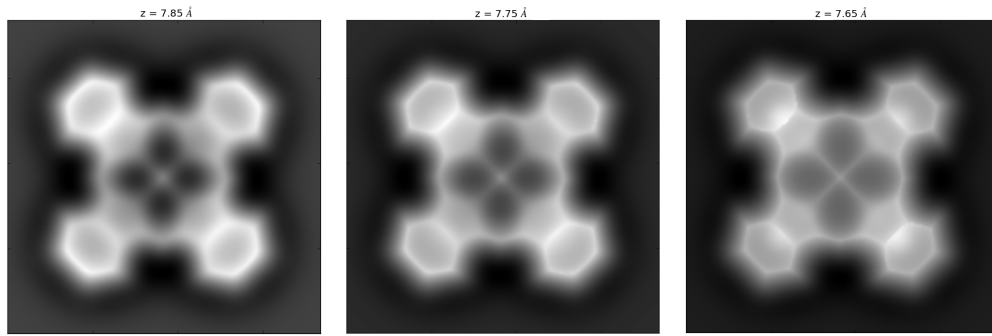


**Figure A.5:** Simulated AFM images of phthalocyanine without any Fe atom at the centre using mechanical L-J model at different tip-sample separation.

reasonable variation in the parameters of the potential did not produce significant changes in the outcome of the calculation.

Though the L-J model was not able to reproduce the AFM image of FePc island exactly, it clearly catches the features of the aryl rings of the FePc molecule. Since we do not have a great number of experimental results and initial attempt to reproduce available AFM images was not very successful, we did not carried out further calculation on MPcs. In future, simulating the AFM images with different tip termination, including the surface interaction, and tuning the parameters may produce better results.

---

# Bibliography

---

- [1] Li, J., Schneider, W.-D., Berndt, R., and Delley, B. *Phys. Rev. Lett.* **80**, 2893–2896 (1998).
- [2] Pascual, J. I., Lorente, N., Song, Z., Conrad, H., and Rust, H. P. *Nature* **423**, 525–528 (2003).
- [3] Jarvis, S. P., Taylor, S., Baran, J. D., Champness, N. R., Larsson, J. A., and Moriarty, P. *Nat. Commun.* **6** (2015).
- [4] Eigler, D. M. and Schweizer, E. K. *Nature* **344**, 524–526 (1990).
- [5] Sugimoto, Y., Abe, M., Hirayama, S., Oyabu, N., Custance, O., and Morita, S. *Nat. Mater.* **4**, 156–159 (2005).
- [6] Grill, L., Rieder, K. H., Moresco, F., Rapenne, G., Stojkovic, S., Bouju, X., and Joachim, C. *Nat. Nanotech.* **2**, 95–98 (2007).
- [7] Binnig, G., Rohrer, H., Gerber, C., and Weibel, E. *Phys. Rev. Lett.* **49**, 57–61 (1982).
- [8] Binnig, G., Quate, C. F., and Gerber, C. *Phys. Rev. Lett.* **56**, 930–933 (1986).
- [9] Lehn, J.-M. *Proc. Natl. Acad. Sci. U.S.A.* **99**, 4763–4768 (2002).
- [10] Lehn, J.-M. *Chem. Soc. Rev.* **36**, 151–160 (2007).
- [11] Theobald, J. A., Oxtoby, N. S., Phillips, M. A., Champness, N. R., and Beton, P. H. *Nature* **424**, 1029–1031 (2003).
- [12] Grill, L., Dyer, M., Lafferentz, L., Persson, M., Peters, M. V., and Hecht, S. *Nat. Nanotech.* **2**, 687–691 (2007).

## Bibliography

---

- [13] Barth, J. V., Costantini, G., and Kern, K. *Nature* **437**, 671–679 (2005).
- [14] Gross, L., Mohn, F., Moll, N., Liljeroth, P., and Meyer, G. *Science* **325**, 1110–1114 (2009).
- [15] Gross, L., Mohn, F., Moll, N., Schuler, B., Criado, A., Guitián, E., Peña, D., Gourdon, A., and Meyer, G. *Science* **337**, 1326–1329 (2012).
- [16] Pavliček, N., Fleury, B., Neu, M., Niedenführ, J., Herranz-Lancho, C., Ruben, M., and Repp, J. *Phys. Rev. Lett.* **108**, 086101–5 (2012).
- [17] de Oteyza, D. G., Gorman, P., Chen, Y.-C., Wickenburg, S., Riss, A., Mowbray, D. J., Etkin, G., Pedramrazi, Z., Tsai, H.-Z., Rubio, A., Crommie, M. F., and Fischer, F. R. *Science* **340**, 1434–1437 (2013).
- [18] Sweetman, A., Jarvis, S. P., Rahe, P., Champness, N. R., Kantorovich, L., and Moriarty, P. *Phys. Rev. B* **90**, 165425 (2014).
- [19] Jarvis, S. P., Sweetman, A. M., Lekkas, I., Champness, N. R., Kantorovich, L., and Moriarty, P. *J. Phys.: Condens. Matter* **27**, 054004 (2015).
- [20] Binnig, G., Rohrer, H., Gerber, C., and Weibel, E. *Phys. Rev. Lett.* **50**, 120–123 (1983).
- [21] Binnig, G. and Rohrer, H. *Surf. Sci.* **126**, 236–244 (1983).
- [22] Chen, C. J. *Introduction to Scanning Tunneling Microscopy*. Oxford University Press, (2008).
- [23] Bai, C. *Scanning Tunneling Microscopy and Its Application*. Springer, (2000).
- [24] [http://home.iitk.ac.in/~gopan/index\\_files/STM.htm](http://home.iitk.ac.in/~gopan/index_files/STM.htm) (Visited on February 2017).
- [25] Pham, T. A. *Constructing low-dimensional molecular networks on metal surfaces*. PhD thesis, University of Groningen, Netherlands, (2016).

## Bibliography

---

- [26] Montanari, S. *Fabrication and characterization of planar Gunn diodes for Monolithic Microwave Integrated Circuits*. PhD thesis, Research Center Juelich, Germany, (2004).
- [27] Giessibl, F. J. *Appl. Phys. Lett.* **73**, 3956–3958 (1998).
- [28] Giessibl, F. J. *Rev. Mod. Phys.* **75**, 949–983 (2003).
- [29] Erlandsson, R., Olsson, L., and Mrtensson, P. *Phys. Rev. B* **54**, R8309–R8312 (1996).
- [30] Albrecht, T. R., Grütter, P., Horne, D., and Rugar, D. *J. Appl. Phys.* **69**, 668–673 (1991).
- [31] Nony, L., Baratoff, A., Schär, D., Pfeiffer, O., Wetzels, A., and Meyer, E. *Phys. Rev. B* **74**, 235439 (2006).
- [32] Giessibl, F. J. *Phys. Rev. B* **56**, 16010–16015 (1997).
- [33] Giessibl, F. J. *Appl. Phys. Lett.* **78**, 123–125 (2001).
- [34] Gross, L., Mohn, F., Moll, N., Meyer, G., Ebel, R., Abdel-Mageed, W. M., and Jaspars, M. *Nat. Chem.* **2**, 821–825 (2010).
- [35] Sun, Z., Boneschanscher, M. P., Swart, I., Vanmaekelbergh, D., and Liljeroth, P. *Phys. Rev. Lett.* **106**, 046104 (2011).
- [36] Kohn, W. and Sham, L. J. *Phys. Rev.* **140**, A1133–A1138 (1965).
- [37] Grimme, S. *J. Chem. Phys.* **124**, 034108 (2006).
- [38] Caciuc, V., Hlscher, H., Blgel, S., and Fuchs, H. *Phys. Rev. B* **74**, 165318 (2006).
- [39] Yurtsever, A., Fernandez-Torre, D., Gonzalez, C., Jelnek, P., Pou, P., Sugimoto, Y., Abe, M., Prez, R., and Morita, S. *Phys. Rev. B* **85**, 125416 (2012).
- [40] Chan, T. L., Wang, C. Z., Ho, K. M., and Chelikowsky, J. R. *Phys. Rev. Lett.* **102**, 176101 (2009).
- [41] Kim, M. and Chelikowsky, J. R. *Appl. Surf. Sci.* **303**, 163–167 (2014).

## Bibliography

---

- [42] Ralf, B., Csar, G., Jens, S., Pavel, J., Rubn, P., and Angelika, K. *Nanotechnology* **20**, 505703 (2009).
- [43] Boneschanscher, M. P., Hämäläinen, S. K., Liljeroth, P., and Swart, I. *ACS Nano* **8**, 3006–3014 (2014).
- [44] Hapala, P., Kichin, G., Wagner, C., Tautz, F. S., Temirov, R., and Jelnek, P. *Phys. Rev. B* **90**, 085421 (2014).
- [45] Hämäläinen, S. K., van der Heijden, N., van der Lit, J., den Hartog, S., Liljeroth, P., and Swart, I. *Phys. Rev. Lett.* **113**, 186102 (2014).
- [46] Hapala, P., Temirov, R., Tautz, F. S., and Jelnek, P. *Phys. Rev. Lett.* **113**, 226101 (2014).
- [47] Temirov, R., Soubatch, S., Neucheva, O., Lassise, A. C., and Tautz, F. S. *New J. Phys.* **10**, 053012 (2008).
- [48] Weiss, C., Wagner, C., Kleimann, C., Rohlfing, M., Tautz, F. S., and Temirov, R. *Phys. Rev. Lett.* **105**, 086103 (2010).
- [49] Weiss, C., Wagner, C., Temirov, R., and Tautz, F. S. *J. Am. Chem. Soc.* **132**, 11864–11865 (2010).
- [50] Eigler, D. M., Lutz, C. P., and Rudge, W. E. *Nature* **352**, 600–603 (1991).
- [51] Bartels, L., Meyer, G., and Rieder, K.-H. *Appl. Phys. Lett.* **71**, 213–215 (1997).
- [52] Mohn, F., Schuler, B., Gross, L., and Meyer, G. *Appl. Phys. Lett.* **102**, 073109 (2013).
- [53] Gross, L. *Nat. Chem.* **3**, 273–278 (2011).
- [54] Nikolaj, M., Leo, G., Fabian, M., Alessandro, C., and Gerhard, M. *New J. Phys.* **12**, 125020 (2010).
- [55] Weymouth, A. J., Hofmann, T., and Giessibl, F. J. *Science* **343**, 1120–1122 (2014).
- [56] Neu, M., Moll, N., Gross, L., Meyer, G., Giessibl, F. J., and Repp, J. *Phys. Rev. B* **89**, 205407 (2014).

## Bibliography

---

- [57] Moll, N., Schuler, B., Kawai, S., Xu, F., Peng, L., Orita, A., Otera, J., Curioni, A., Neu, M., Repp, J., Meyer, G., and Gross, L. *Nano Lett.* **14**, 6127–6131 (2014).
- [58] Zhang, J., Chen, P., Yuan, B., Ji, W., Cheng, Z., and Qiu, X. *Science* **342**, 611–614 (2013).
- [59] Sweetman, A. M., Jarvis, S. P., Sang, H., Lekkas, I., Rahe, P., Wang, Y., Wang, J., Champness, N. R., Kantorovich, L., and Moriarty, P. *Nat Commun* **5**, 3931 (2014).
- [60] Endres, R. G., Fong, C. Y., Yang, L. H., Witte, G., and Wöll, C. *Comput. Mater. Sci.* **29**, 362–370 (2004).
- [61] Arunan, E., Desiraju Gautam, R., Klein Roger, A., Sadlej, J., Scheiner, S., Alkorta, I., Clary David, C., Crabtree Robert, H., Dannenberg Joseph, J., Hobza, P., Kjaergaard Henrik, G., Legon Anthony, C., Mennucci, B., and Nesbitt David, J. *Pure Appl. Chem.* **83**(8), 1637 (2011).
- [62] Wheland, G. W. *J. Am. Chem. Soc.* **64**, 900–908 (1942).
- [63] Yates, K. *Hückel Molecular Orbital Theory*. Academic Press, (1978).
- [64] Hoffmann, R. *J. Chem. Phys.* **39**, 1397–1412 (1963).
- [65] Pritchard, H. O. and Skinner, H. A. *Chem. Rev.* **55**, 745–786 (1955).
- [66] Wolfsberg, M. and Helmholz, L. *J. Chem. Phys.* **20**, 837–843 (1952).
- [67] Slater, J. C. *Phys. Rev.* **36**, 57–64 (1930).
- [68] Boys, S. F. *Proc. R. Soc. Lond. A* **200**, 542–554 (1950).
- [69] Hehre, W. J., Stewart, R. F., and Pople, J. A. *J. Chem. Phys.* **51**, 2657–2664 (1969).
- [70] Bardeen, J. *Phy. Rev. Lett.* **6**, 57–59 (1961).
- [71] Arfken, G. *Mathematical Methods for Physicists*. Academic Press, (1968).
- [72] Tersoff, J. and Hamann, D. R. *Phys. Rev. Lett.* **50**, 1998–2001 (1983).

## Bibliography

---

- [73] Tersoff, J. and Hamann, D. R. *Phys. Rev. B* **31**, 805–813 (1985).
- [74] Chen, C. J. *Phys. Rev. B* **42**, 8841–8857 (1990).
- [75] Jones, J. E. *Proc. R. Soc. Lond. A* **106**, 441–462 (1924).
- [76] Jones, J. E. *Proc. R. Soc. Lond. A* **106**, 463–477 (1924).
- [77] Nikolaj, M., Leo, G., Fabian, M., Alessandro, C., and Gerhard, M. *New J. Phys.* **14**, 083023 (2012).
- [78] Lakin, A. J. *Theoretical Interpretation of Scanning Probe Microscopy Images Involving Organic Molecules*. PhD thesis, The University of Nottingham, UK, (2014).
- [79] Gross, E. and Dreizler, R. *Density Functional Theory*. Springer US, (2013).
- [80] Martin, R. *Electronic Structure: Basic Theory and Practical Methods*. Cambridge University Press, (2004).
- [81] Parr, R. and Weitao, Y. *Density-Functional Theory of Atoms and Molecules*. Oxford University Press, (1994).
- [82] Payne, M. C., Teter, M. P., Allan, D. C., Arias, T. A., and Joannopoulos, J. D. *Rev. Mod. Phys.* **64**, 1045–1097 (1992).
- [83] Lundqvist, S. and March, N. H. *Theory of the Inhomogeneous Electron Gas*. Plenum Press, (1983).
- [84] Hohenberg, P. and Kohn, W. *Phys. Rev.* **136**, B864–B871 (1964).
- [85] Borštnik, U., VandeVondele, J., Weber, V., and Hutter, J. *Parallel Computing* **40**, 47–58 (2014).
- [86] Hutter, J., Iannuzzi, M., Schiffmann, F., and VandeVondele, J. *WIREs Comput. Mol. Sci.* **4**, 15–25 (2014).
- [87] VandeVondele, J., Krack, M., Mohamed, F., Parrinello, M., Chassaing, T., and Hutter, J. *Computer Physics Communications* **167**, 103–128 (2005).
- [88] Jarvis, S. P., Rashid, M. A., Sweetman, A., Leaf, J., Taylor, S., Moriarty, P., and Dunn, J. *Phys. Rev. B* **92**, 241405(R) (2015).

## Bibliography

---

- [89] Sweetman, A., Rashid, M. A., Jarvis, S. P., Dunn, J. L., Rahe, P., and Moriarty, P. *Nat. Commun.* **7**, 10621 (2016).
- [90] Kroto, H. W., Heath, J. R., O'Brien, S. C., Curl, R. F., and Smalley, R. E. *Nature* **318**, 162–163 (1985).
- [91] Park, H., Park, J., Lim, A. K. L., Anderson, E. H., Alivisatos, A. P., and McEuen, P. L. *Nature* **407**, 57–60 (2000).
- [92] Schull, G., Frederiksen, T., Arnau, A., Sanchez-Portal, D., and Berndt, R. *Nat. Nanotech.* **6**, 23–27 (2011).
- [93] Gunnar, S., Katharina, J. F., and Jose Ignacio, P. *New J. Phys.* **10**, 065005 (2008).
- [94] Mayne, A. J. and Dujardin, G. *New Diam. Front. C. Tec.* **15**, 265–274 (2005).
- [95] Kawai, S., Sadeghi, A., Xu, F., Peng, L., Orita, A., Otera, J., Goedecker, S., and Meyer, E. *ACS Nano* **9**, 2574–2583 (2015).
- [96] Girifalco, L. A. *J. Phys. Chem.* **95**, 5370–5371 (1991).
- [97] Chiutu, C., Sweetman, A. M., Lakin, A. J., Stannard, A., Jarvis, S., Kantorovich, L., Dunn, J. L., and Moriarty, P. *Phys. Rev. Lett.* **108**, 268302 (2012).
- [98] Lakin, A. J., Chiutu, C., Sweetman, A. M., Moriarty, P., and Dunn, J. L. *Phys. Rev. B* **88**, 035447 (2013).
- [99] Jin, C., Hettich, R. L., Compton, R. N., Tuinman, A., Derecskei-Kovacs, A., Marynick, D. S., and Dunlap, B. I. *Phys. Rev. Lett.* **73**, 2821–2824 (1994).
- [100] Zhou, F., Van Berkel, G. J., and Donovan, B. T. *J. Am. Chem. Soc.* **116**, 5485–5486 (1994).
- [101] Troyanov, S. I., Troshin, P. A., Boltalina, O. V., Ioffe, I. N., Sidorov, L. N., and Kemnitz, E. *Angew. Chem. Int. Ed.* **40**, 2285–2287 (2001).
- [102] Hedberg, L., Hedberg, K., Boltalina, O. V., Galeva, N. A., Zapolskii, A. S., and Bagryantsev, V. F. *J. Phys. Chem. A* **108**, 4731–4736 (2004).

## Bibliography

---

- [103] Sharp, P. *Passivated silicon and diamond surfaces: Mapping, modification, and molecular adsorption*. PhD thesis, The University of Nottingham, UK, (2013).
- [104] Sweetman, A., Jarvis, S. P., and Rashid, M. A. *Beilstein J. Nanotechnol.* **7**, 937–945 (2016).
- [105] Schlier, R. E. and Farnsworth, H. E. *J. Chem. Phys.* **30**, 917–926 (1959).
- [106] Takayanagi, K., Tanishiro, Y., Takahashi, S., and Takahashi, M. *Surf. Sci.* **164**, 367–392 (1985).
- [107] Brommer, K. D., Needels, M., Larson, B., and Joannopoulos, J. D. *Phys. Rev. Lett.* **68**, 1355–1358 (1992).
- [108] Sweetman, A., Rahe, P., and Moriarty, P. *Nano Lett.* **14**, 2265–2270 (2014).
- [109] Sadewasser, S., Jelinek, P., Fang, C.-K., Custance, O., Yamada, Y., Sugimoto, Y., Abe, M., and Morita, S. *Phys. Rev. Lett.* **103**, 266103 (2009).
- [110] Giessibl, F. J. *Appl. Phys. Lett.* **76**, 1470–1472 (2000).
- [111] Giessibl, F. J., Hembacher, S., Bielefeldt, H., and Mannhart, J. *Science* **289**, 422–425 (2000).
- [112] Weston, M. *Adsorption and Charge Transfer Dynamics of Photovoltaic and Photocatalytic Dye-Sensitizers*. PhD thesis, The University of Nottingham, UK, (2014).
- [113] Grätzel, M. *J. Photochem. Photobiol., A* **164**, 3–14 (2004).
- [114] Kohle, O., Ruile, S., and Grätzel, M. *Inorg. Chem.* **35**, 4779–4787 (1996).
- [115] Rensmo, H., Sdergren, S., Patthey, L., Westermark, K., Vayssieres, L., Kohle, O., Brühwiler, P. A., Hagfeldt, A., and Siegbahn, H. *Chem. Phys. Lett.* **274**, 51–57 (1997).
- [116] Grätzel, M. *Nature* **414**, 338–344 (2001).

## Bibliography

---

- [117] Grätzel, M. *Phil. Trans. R. Soc. A* **365**, 993–1005 (2007).
- [118] O’Shea, J. N., Taylor, J. B., Mayor, L. C., Swarbrick, J. C., and Schnadt, J. *Surf. Sci.* **602**, 1693–1698 (2008).
- [119] Ben Taylor, J., Mayor, L. C., Swarbrick, J. C., O’Shea, J. N., Isvoranu, C., and Schnadt, J. *J. Chem. Phys.* **127**, 134707 (2007).
- [120] Labat, F. and Adamo, C. *J. Phys. Chem. C* **111**, 15034–15042 (2007).
- [121] Thomas, A. G., Flavell, W. R., Chatwin, C., Rayner, S., Tsoutsou, D., Kumarasinghe, A. R., Brete, D., Johal, T. K., Patel, S., and Purton, J. *Surf. Sci.* **592**, 159–168 (2005).
- [122] Odelius, M., Persson, P., and Lunell, S. *Surf. Sci.* **529**, 47–58 (2003).
- [123] Persson, P. and Lunell, S. *Sol. Energy Mater. Sol. Cells* **63**, 139–148 (2000).
- [124] Lippert, G., Parrinello, J. H., and Michele. *Mol. Phys.* **92**, 477–488 (1997).
- [125] Goedecker, S., Teter, M., and Hutter, J. *Phys. Rev. B* **54**, 1703–1710 (1996).
- [126] Hartwigsen, C., Goedecker, S., and Hutter, J. *Phys. Rev. B* **58**, 3641–3662 (1998).
- [127] Krack, M. *Theor. Chem. Acc.* **114**, 145–152 (2005).
- [128] Perdew, J. P., Burke, K., and Ernzerhof, M. *Phys. Rev. Lett.* **77**, 3865–3868 (1996).
- [129] Grimme, S., Ehrlich, S., and Goerigk, L. *J. Comput. Chem.* **32**, 1456–1465 (2011).
- [130] Grimme, S., Antony, J., Ehrlich, S., and Krieg, H. *J. Chem. Phys.* **132**, 154104 (2010).
- [131] VandeVondele, J. and Hutter, J. *J. Chem. Phys.* **127**, 114105 (2007).
- [132] Pettersen, E. F., Goddard, T. D., Huang, C. C., Couch, G. S., Greenblatt, D. M., Meng, E. C., and Ferrin, T. E. *J. Comput. Chem.* **25**, 1605–1612 (2004).

## Bibliography

---

- [133] Van Slyke, S. A., Chen, C. H., and Tang, C. W. *Appl. Phys. Lett.* **69**, 2160–2162 (1996).
- [134] Bao, Z., Lovinger, A. J., and Dodabalapur, A. *Appl. Phys. Lett.* **69**, 3066–3068 (1996).
- [135] Wu, S. W., Nazin, G. V., Chen, X., Qiu, X. H., and Ho, W. *Phys. Rev. Lett.* **93**, 236802 (2004).
- [136] Placencia, D., Wang, W., Shallcross, R. C., Nebesny, K. W., Brumbach, M., and Armstrong, N. R. *Adv. Funct. Mater.* **19**, 1913–1921 (2009).
- [137] Tao, N. *Nat. Chem.* **1**, 108–109 (2009).
- [138] Sedona, F., Di Marino, M., Forrer, D., Vittadini, A., Casarin, M., Cossaro, A., Floreano, L., Verdini, A., and Sambi, M. *Nat. Mater.* **11**, 970–977 (2012).
- [139] Lindner, S., Treske, U., and Knupfer, M. *App. Surf. Sci.* **267**, 62–65 (2013).
- [140] Szczepaniak, B. and Bragiel, P. *Vacuum* **46**, 465–467 (1995).